Potential Energy Surface and Rotational Energy Transfers in CNNC and NCCP in Collision with He and *para*-H_2

Ph.D. Thesis

by

RITIKA

DEPARTMENT OF CHEMISTRY
INDIAN INSTITUTE OF TECHNOLOGY ROPAR
RUPNAGAR, PUNJAB 140001, INDIA
July 2024

Potential Energy Surface and Rotational Energy Transfers in CNNC and NCCP in Collision with He and *para*-H_2

A Thesis Submitted
in Fulfilment of the Requirements
for the Degree of

DOCTOR OF PHILOSOPHY

by

RITIKA
2019CYZ0007

to the

DEPARTMENT OF CHEMISTRY

INDIAN INSTITUTE OF TECHNOLOGY ROPAR
RUPNAGAR, PUNJAB 140001, INDIA
July 2024

Dedicated

to my family

DECLARATION BY THE CANDIDATE

I hereby declare that the work described in the thesis entitled "Potential Energy Surface and Rotational Energy Transfers in CNNC and NCCP in Collision with He and *para*-H_2" submitted for the degree of **Doctor of Philosophy** in Chemistry to the Indian Institute of Technology Ropar has been carried out under the supervision of **Dr. T. J. Dhilip Kumar**. The work is original and has not been submitted in part or full by me elsewhere for a degree.

Place: Rupnagar
Date: 25-07-2024

Ritika
Research Scholar

CERTIFICATE

It is certified that the work contained in this thesis entitled "Potential Energy Surface and Rotational Energy Transfers in CNNC and NCCP in Collision with He and *para*-H_2" by **Ms. Ritika**, a student in the Department of Chemistry, Indian Institute of Technology Ropar, for the award of degree of **Doctor of Philosophy** has been carried out under my supervision and that this work has not been submitted elsewhere for a degree.

Place: Rupnagar
Date: 25-07-2024

Dr. T. J. Dhilip Kumar
Research Supervisor

Acknowledgements

I take great pleasure in expressing my heartfelt gratitude to all those individuals who provided unwavering support during this successful journey. First and foremost, I express my sincere thanks to my supervisor, *Dr. T. J. Dhilip Kumar*, for providing me the opportunity to pursue my doctoral studies under his guidance. I am profoundly grateful for his constant support and mentorship throughout the course. He has been a constant source of inspiration, providing not only valuable academic expertise but also encouragement and patience. I am also thankful for the opportunities provided by him to engage in meaningful research, present at conferences, and interact with experts in the field. His belief in my abilities has been a driving force behind the successful completion of this thesis. I thank him for his trust, understanding, and the invaluable lessons I have learned under his guidance. This journey would not have been the same without his support.

I would also like to extend my warm thanks to *Dr. Rajendra Srivastava*, *Dr. Manoj Kumar Pandey*, *Dr. Sudipta Sinha*, and *Dr. Sandeep Gautam* for their contributions as members of my doctoral committee and for providing helpful feedback and suggestions. I am also thankful for the assistance and support from *Mrs. Poonam Kataria*, *Mrs. Samita Saini*, and other staff members of the Department of Chemistry throughout the research process.

I thank IIT Ropar for providing a platform for doing research with high-performance computing facilities. I also acknowledge the Ministry of Education for granting me the Prime Minister Research Fellowship. Financial support from IIT Ropar to attend national and international conferences is gratefully acknowledged. A travel grant from the Science and Engineering Research Board, India to attend the international conferences is highly appreciated.

I am thankful to my seniors *Dr. Sandeep Kumar*, *Dr. Rohit Sathe*, *Dr. Sanchit Kumar*, *Dr. Neha Yadav* and my lab-mates *Ms. Nidhi Duhan*, *Mr. Apoorv Kushwaha*, *Ms. Preeti*, *Ms. Pooja Chahal*, *Ms. Manpreet Kaur*, *Ms. Gurpreet Kaur*, *Mr. Habit Titan*, *Ms. Shalini Mishra* and *Mr. Triumphany Cotibal Sagolsem* for their constant support and maintaining a good environment in the lab. Special regards to *Mr. Apoorv Kushwaha* and *Mr. Shivam Gupta* for healthy discussions and their timely help in generating computer codes.

It is truly impossible to imagine my days in IIT without friends. I convey my heartfelt thanks to my batchmates and friends *Mr. Anoop Chahal*, *Mr. Saurav Chatterjee*, *Mr. Sandeep Patel*, *Mr. Vishal Kumar*, *Mr. Arijit Hazra*, and *Mr. Priyank Sharma* for sharing good memories. They made my research period memorable and enjoyable.

I owe a debt of gratitude to my parents, my brother *Mr. Jai* and my sister *Ms. Anjali* for their constant belief in me. I am truly blessed to have parents who have always stood by me and inspired me to pursue my dreams. I would like to express my heartfelt gratitude to my husband *Mr. Jagrit Grover* for being my constant source of strength. His unwavering support, insightful discussions, and constructive suggestions have played a pivotal role in the successful completion of this thesis.

This work would have never taken shape without the blessings of *Sai Baba*. I express my gratitude to all individuals who assisted me, both directly and indirectly, throughout my Ph.D. journey and guided me along the path.

Ritika

Abstract

Keywords: Interstellar Medium, Potential Energy Surface, *Ab Initio* Method, Coupled Cluster method, Multipolar Expansion, Collisional De-excitation, Quantum Dynamics, Scattering Theory, Bound States, Pressure Broadening, Ultracold Chemistry.

In the past century, our understanding of the interstellar medium (ISM) has greatly evolved. Initially thought of as empty space between stars, modern astrochemistry has revealed a complex web of physical and chemical processes in various interstellar environments. Around 300 molecules have been detected in interstellar space with the help of spectroscopy so far that are dominated by H_2 and He. Because of their importance, several communities are working on experimental and theoretical astrochemistry to determine the spectroscopic properties. In ISM, the density is typically low, and collisions occur rarely, making it challenging to maintain a local thermodynamic equilibrium. Consequently, it becomes important to calculate the collisional rate with key collisional partners like H_2 and He. For calculating collisional rate coefficients, the first step is to define the potential energy surface (PES) of the colliding system.

The work deals with the interaction of interstellar molecules CNNC and NCCP with He and *para*-H_2. New accurate *ab initio* PESs for CNNC-He, CNNC-H_2, NCCP-He and NCCP-H_2 are generated using electronic structure calculations involving coupled-cluster singles and doubles with perturbative triples with F12 approximation (CCSD(T)-F12) and augmented correlation consistent polarized valence triple zeta (aVTZ) basis sets. To perform the dynamical calculations, the ground state PESs are expanded in terms of Legendre polynomials. The time-independent approach of quantum dynamics is employed to study the collisional systems. Inelastic cross-sections for the rotational de-excitations of all the studied systems have been computed with a close-coupling method. The cross-sections are then thermally averaged to calculate the collisional rate coefficients at interstellar temperatures. Only

even Δj transitions are allowed in the case of CNNC collisions, whereas both even and odd Δj transitions are present for NCCP. NCCP-*para*-H_2 rates are determined to be 1.5-4.5 times of NCCP-He.

A tremendous increase in the research on ion-molecule interactions is attributed to their involvement in the synthesis of larger molecules in interstellar clouds. These reactions become important as compared to neutral species interactions due to the long-range electrostatic interactions occurring between ion and atom. In this context, the interaction of ionic molecule COH^+ in collision with He is studied considering its possibility to form bound states. COH^+-He has a global minimum of 836.55 cm^{-1} and He approaches from H-side of COH^+ in stable configuration. Inelastic and pressure broadening (PB) cross-sections are calculated and compared for COH^+-He, resulting in some extra peaks in PB cross-sections. The obtained rotational rate coefficients are consistent with the previously reported data for COH^+-He.

Cooling molecules to ultracold temperatures has produced a new research area of ultracold chemistry due to their applications in controlled chemical reactions and ultrahigh-resolution molecular spectroscopy. In the ultracold study, rotational quenching cross-sections and rate coefficients are computed for C_2 in collision with C_2-^{3,4}He. The quenching cross-sections are found to obey Wigner's threshold laws. The isotopic effect of He is analyzed by computing the scattering lengths and lifetime of quasi bound states. Quenching rate coefficients suggest that C_2 can be cooled with ^{4}He buffer gas.

List of Abbreviations

amu	Atomic mass unit
aVTZ	Augmented Correlation Consistent Polarized Valence Triple-Zeta
aVQZ	Augmented Correlation Consistent Polarized Valence Quadruple-Zeta
BF	Body Fixed
BO	Born-Oppenheimer
BS	Basis Set
CBS	Complete Basis Set
CC	Close Coupling
CCSD(T)	Coupled-Cluster with Single and Double and Perturbative Triple Excitation
DF	Density Fitting
GTO	Gaussian-Type Orbitals
HF	Hartree-Fock
HWHM	Half-Width-at-Half-Maximum
ISM	Interstellar Medium
LTE	Local Thermodynamic Equilibrium
PB	Pressure Broadening
PES	Potential Energy Surface
PEC	Potential Energy Curve
PS	Pressure Shift
SCF	Self-Consistent Field
SE	Schrödinger Equation
SF	Space Fixed
SL	Scattering Length
STO	Slater-Type Orbitals
TMC	Taurus Molecular Cloud

List of Symbols and Units Conversion

Table 1: Conversion factor.

Distance	a_0	0.529177 Å
Electric Charge	e	1.6022×10^{-19} C
Dipole Moment	ea_0	8.4784×10^{-30} C-m
Quadrupole Moment	ea_0^2	$4.486551331 \times 10^{-40}$ C-m^2

In this Table, a_0 is the Bohr radius (atomic units of length), e is the electrical charge, Å is the Angstrom, C is the Coulomb and m is the meter.

Table 2: Energy conversion.

	hartree	cm^{-1}	eV	J
hartree	1	219474.63	27.2114	4.3597×10^{-18}
cm^{-1}	4.5563×10^{-6}	1	1.2398×10^{-4}	1.9863×10^{-23}
eV	3.6749×10^{-2}	8065.73	1	1.6021×10^{-19}
J	2.2937×10^{17}	5.0344×10^{22}	6.2418×10^{18}	1

Contents

List of Figures

List of Tables

Chapter 1

Introduction

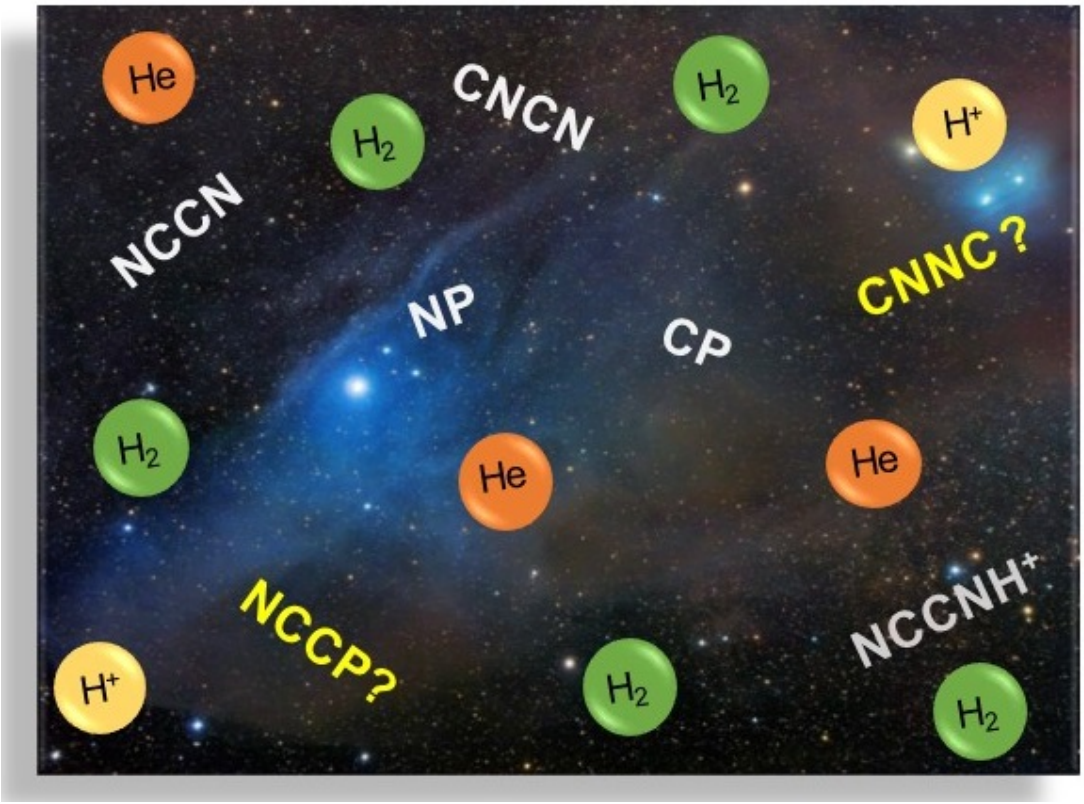

Introduction

1.1 Background

It all began in the early days of spectroscopy when Joseph von Fraunhofer, an optician and physicist, made a groundbreaking discovery about the solar system. He identified numerous fine dark absorption lines within the solar spectrum using telescopes and lenses. These distinctive dark lines emerged as a result of elements absorbing specific wavelengths emitted by the sun. This crucial discovery represented a notable milestone in spectroscopy, indicating that the composition of the sun and stars matches that of Earth's chemical constituents. It proved to be one of the most notable applications of spectroscopy to celestial bodies.[1] Thereafter, the collaboration between astrophysicists and spectroscopists started and aimed at attributing these lines in the solar spectrum with atomic transitions, marking the beginning of what is now acknowledged as modern astrophysics.[2] Identifying these lines firmly established spectroscopy as a potent analytical tool for investigating the chemical and physical conditions of astronomical bodies. Excited about the possibilities offered by spectroscopy, astrophysicists expressed that this technique would unveil a completely unexplored domain, extending far beyond Earth and our solar system.

The teamwork between spectroscopists and astrophysicists has been found to be consistently productive and captivating, resulting in the successful identification of more than 300 diverse molecular species[3] in both circumstellar envelopes and the interstellar medium (ISM). These molecules vary from simpler diatomic molecules like C_2, H_2, CH, N_2, NP, CO, OH, etc., to more complex species with eight atoms or more.[4,5] Each molecule discovered provides valuable insights into the physics and chemistry of the observed environment.[6] Molecules are not confined only to the ISM and circumstellar regions but are widespread in various celestial regions. This study primarily concentrates on circumstellar and interstellar molecules. The exploration of such species to understand the physical conditions in space has become a significant trend, sparking increased interest in astrochemistry, astronomy, and related fields.[7]

1.1.1 An Introduction to the Interstellar Medium

In the early 20th century, interstellar space was commonly considered an empty vacuum spotted with black holes, planets, stars, and other celestial structures. But

the discovery of various molecules, such as HNC, HCl, OH^+, CO^+, and COH^+, etc., has led to the realization that this space between the stars consists of the biggest storehouse of chemically bonded matter and concluded that this space is not empty.[8] ISM is simply home to a lot of stuff or matter that exists between stars, including dust, gases (in all their forms), and cosmic rays.[9] The composition of the interstellar medium is predominantly 99 percent gas and 1 percent dust. Concerning the gas in the interstellar medium, 90 percent consists of hydrogen atoms, 8 percent of helium atoms, and 2 percent comprises atoms of heavier elements than hydrogen and He, such as carbon, nitrogen, oxygen, sulphur, etc. Interstellar dust primarily comprises particles of heavier elements, mainly consisting of silicates, iron, carbon, and dirty ice.

The thermal and chemical states of the ISM are conventionally described in terms of a number of distinct phases characterizing the temperature, ionization fractions, and density.[10] These phases are hot ionized medium, warm ionized and neutral medium, and cold neutral medium. Due to the abundance of hydrogen, scientists have classified various types of ISM clouds based on the type of hydrogen they contain. The cold medium consists of hydrogen in the molecule form (H_2), and this region is called a molecular cloud. It is the densest region (10^3-10^6 cm^{-3}) of the ISM and is made up of H_2 molecules with the lowest temperature of 10-20 K. It makes up a small portion of the mass of ISM (25%). On the other hand, atomic hydrogen is present in a cold neutral medium with a density of 3050 cm^{-3} and a temperature of $\sim$ 70-100 K. Among the various phases of ISM, molecular clouds hold particular significance in the realm of interstellar chemistry.[11] These clouds serve as the birthplace of 70% of molecules, where their formation and detection occur. Among the molecular species identified in space, 17 different elements are present, including the five most crucial biogenic elements: N, C, P, H and O. 80% molecules are linear and organic in nature.[12]

1.1.2 Important tool for Interstellar Molecules: Molecular Spectroscopy

Spectroscopy has now become an indispensable tool that enables astronomers to explore the universe, unveiling details such as physical characteristics, radial velocities, and, chemical compositions of celestial objects.[13] It has proven invaluable in measuring the dark matter present in galaxies, determining the net mass of galaxy clusters & stars, and estimating the rate of the Universe expansion. Molecules are identified in interstellar medium by analyzing their unique spectroscopic signatures.[14] The

distinctiveness of each molecule's spectrum proves valuable in both terrestrial laboratories and the ISM for identifying the molecules. The primary method for detecting molecules in the ISM involves comparing spectroscopic frequencies observed through a radio telescope with spectral features derived either from laboratory experiments or precise theoretical predictions.[15,16] The gases in ISM emit detectable radiation, making it readily accessible for astrochemists to study. The unique conditions of ISM allow for the observation of forbidden lines, while in regular laboratory settings, less probable transitions are considered "forbidden" because high energy states readily undergo collisional de-excitation. In the ISM, the duration of collisions is typically far greater than the lifespans of these excited states, especially for forbidden transitions. This characteristic makes such transitions easily detectable and potentially dominant in the spectrum. Molecules within the ISM exhibit rotational energy due to bodily rotation around their centre of gravity, forming the basis of radio astronomy.

1.1.3 Why Rotational Spectroscopy?

Within the realm of high-resolution spectroscopic methods, rotational spectroscopy (RS) is a paramount technique in ISM for identifying molecules.[17] In contrast to widely used spectroscopic techniques in analytical chemistry, such as NMR, IR, and UV-spectroscopies, microwave spectroscopy has relatively few but distinctive applications. One notable application is its role in chemically examining the interstellar medium. RS entails measuring the transition energy in the gas phase between two rotational states of molecules.[18] These rotational level changes stem from the rotation of the molecule, causing a change in the permanent dipole moment. Transitions among rotational levels are generally less energetic than transitions between electronic and vibrational states. Consequently, rotationally excited states are more readily populated at the lower temperatures of ISM, and molecules exist in their vibrational and electronic ground states. As a result, in the radio frequency and microwave regions, the molecular cloud's spectra will have sharp lines corresponding to rotational transitions. Over 70% of all known interstellar molecular species, such as NP, CCP, HCCN, CNCN, COH^+, HCO^+, NCCP, etc., have been identified based on their rotational spectral characteristics using a spectrometer linked to a radio telescope, and helped to determine their abundance and the physical conditions of the environment.[6,7]

1.1.4 Role of Quantum Chemistry in Astrochemistry

Numerous molecules within the ISM have been detected through quantum chemistry due to advancements in the accuracy of electronic structure calculations and quantum chemical methods. After years of significant improvement in quantum theories and development in the power of computational facilities, quantum chemical calculations have reached a level where they can depict real systems with accuracy comparable to experiments. These methodologies have emerged as the most viable option when conducting experiments is impractical, expensive, hazardous, or simply unfeasible. Quantum chemistry provides insights into the energy levels of molecules and the transitions between these levels. Understanding these energy transitions is essential for interpreting the observed spectral lines to determine the presence of molecules and their accurate abundance in space.

The molecular clouds of our interest have the lowest temperature in the interstellar medium, and due to the relatively low density of this region, collisions between species are very rare that local thermodynamic equilibrium cannot be maintained[7]. Consequently, it becomes essential to consider the competition between collisional and radiative processes that determine the energy transfers leading to the distribution of molecular energy levels. The radiative processes involving absorption and emission are characterized by the values of Einstein coefficients that can be known easily experimentally, but the analysis of the collisional processes (excitation and deexcitation) requires information of the collisional rate coefficients. The data of collisional cross-sections and rate coefficients predominantly relies on theoretical calculations, given that laboratory experiments can only offer limited, specific data.[19]

Experimental cross-section studies are generally conducted at room temperature, employing collisional gases like Ne, Ar, and N_2, which are unsuitable for astrophysical scenarios.[20] Using heavier collisional partners in experiments simplifies the setup but limits the analysis of inelastic rate coefficients for collisions involving astrophysical species like H, H^+, H_2 and He. Therefore, theoretical cross-sections and rate coefficients are obtained assuming electronic and nuclear movements (Born-Oppenheimer approximation)[21] separately. In this approximation, cross-sections (and subsequently rate coefficients) are derived by solving the motion of the nuclei on the electronic potential energy surface. Studies that utilize advanced computational techniques to address both electronic and nuclear motion issues have shown that the theory can match the accuracy of experimental data. Many interstellar molecules have been

studied in collision with H, H^+, H_2 and He theoretically. In essence, we can say that quantum chemistry emerges as a valuable source of astrochemical data in situations where experimental approaches face challenges.

1.2 Review of Molecular Systems in ISM

Interstellar chemistry primarily involves organic species. The vast majority of molecules identified in interstellar and circumstellar environments contain at least one carbon atom. These molecules are believed to play a role in the origins of life. Because of their importance, they attract the attention of various scientific communities involved in experimental and theoretical astrochemistry. These communities seek to understand the collision rates of these molecules with the most abundant colliders, i.e., helium and molecular hydrogen (H_2). In our research, we focus on studying the dynamics and spectroscopy of several interstellar molecules, CNNC, NCCP, and COH^+. We will provide a brief overview of these systems.

1.2.1 The Diisocyanogen CNNC

Carbon fragments were discovered in dense intermolecular clouds for the very first time in 1970.[22–24] Among them, nitriles (R−C≡N) and isonitriles (R−N≡C), are of key importance in the field of astrochemistry because of their considerable existence in the circumstellar and interstellar media.[22,25–32] More than 30 cyano and 12 isocyano molecules have been detected in ISM to date. The arrangement of cyanopolyynes, $H-(C\equiv C)_n-C\equiv N$ merits unique consideration since it forms the biggest known interstellar molecules.[33] Cyanogen, NCCN being the simplest molecule of dicyanopolynne series, has been studied extensively both theoretically[34–36] and experimentally.[37–40] NCCN has three other possible isomeric forms CNCN (isocyanogen), CNNC (diisocyanogen) and CCNN (diaza-dicarbon), with relative stability order as NCCN > CNCN > CNNC > CCNN.[41]

Diisocyanogen, the energetically higher-lying isomer of cyanogen and smallest molecule of diisocyanopolyynes family has attracted considerable interest recently both theoretically[42–47] and experimentally.[48–50] The taurus molecular cloud-1 (TMC-1) and IRC+10216 are significant sources of abundance of various nitrile and isonitrile molecules.[25,32,51] In 1991, Kruger reported the first linear isocyano molecule (HCCNC) having a column density 2.9×10^{12} cm^{-2} in TMC-1.[28,29,52] NCCN and CNNC being

centrosymmetric species remains undetected in cold ISM to date and both lack permanent dipole moment whereas CNCN has some value of dipole moment and has been found with few interstellar molecules towards the dense clouds L483.[53,54] However, in 1981 NCCN was found in the atmosphere of Titan and Comets through infrared spectra.[55,56] The detection of CNCN[54], $NCCNH^+$[57] and various isocyano molecules like HNC[31], HCC-NC[28], HC_4NC[25] represent absolute clue of presence of CNNC in ISM. Thus, the presence of diisocyanogen in interstellar space can't be ruled out. To investigate the CNNC abundance in ISM and to understand the CNNC molecule, indirect observations, and theoretical studies are required.

1.2.2 The Cyanophosphaethyne NCCP

IRC+10216 hosts numerous molecules dominated by carbon chain species like cyanopolyyne and polyyne radicals[58,59], along with carbon chains including silicon or sulphur,[60–62] as well as exotic molecules consisting of phosphorus or metals.[26,63] The periodic table's third-row elements are also found there but with low cosmic standards. Phosphorus (also known as a biogenic element) is one of them, which is found to be less abundant. The chemistry of P differs significantly from that of the neighboring second-row element. Phosphorous is released by Type II supernovae into the interstellar medium[64,65] and exists as P^+ in the gas phase, showing little indications of depletion in grains.[29,66] PN was the first phosphorous molecule that was detected more than 35 years ago in ISM by Turner and Bally[67,68] and predicted to be most abundant phosphorus molecule.

Phosphorous is mostly trapped in HCP (C-rich envelopes) or PO and PS (O-rich envelopes), according to thermochemical equilibrium calculations.[69,70] In astrophysical media, the accurate determination of abundances is required for the discovery of new molecules. Without these data, one would have to rely on the physical conditions of local thermodynamic equilibrium (LTE), which are extremely rare in space. We have extended our research for P-bearing species in IRC+10216 to understand more about the chemistry of phosphorous in circumstellar envelopes. Among them, we are interested in NCCP, cyanophosphaethyne (chemical cousin of NCCN), which is expected to be the source of phosphorus in interstellar space. NCCP is found to be a linear molecule having singlet sigma ($^1\Sigma^+$) electronic ground state with a closed shell. NCCP, being the stable isomer among its other possible isomers has been studied extensively.[71–74] In the laboratory, the rotational spectrum of NCCP has been described over a wide spectral range of 26-820 GHz.[74] Agúndez et al. reported the 3

mm line survey that showed 7 NCCPs rotational lines ranging from J=15 to J=21 in the temperature domain of 30-60 K and considered the presence of NCCP in astronomical sources like IRC+10216.[75] The column densities of CCP and NCCP are 1.2-2.9 $\times$ 10^{12} cm^{-2}[63] and 7 $\times$ 10^{11} cm^{-2}[75], respectively, in IRC+10216 suggesting slightly very less abundance of NCCP than CCP. NCCP could be a viable candidate for its discovery in space due to its reasonably significant value of dipole moment i.e. 3.44 D[73] and could follow the following reaction path

$$HNC + CP \rightarrow NCCP + H$$

for its formation having reactants with enough abundance in ISM.[72] PN, CP, HCP, OP, CCP, PH_3 and OP^+ are seven other P-containing molecules that have been successfully discovered in ISM.[24,63,67,68,70,75–79] NCCP is the 8th phosphorus molecule that was identified tentatively and needs further supportive information to be confirmed. For instance, the collisional dynamical study of already discovered phosphorous molecules[80–83] have been discussed with most abundant colliders, but NCCP collisional data is not currently available.

1.2.3 The Isoformyl Cation COH^+

Recently, there has been a significant increase in the study of simple ion-molecule reactions. This is primarily driven by their crucial role in the synthesis of larger molecules within interstellar clouds.[8,84,85] These reactions become important as compared to neutral species interactions due to the long-range electrostatic interactions occurring between molecule and ion.[86,87] The interstellar medium has revealed the presence of over 50 ionic species, shedding light on the abundance of numerous other observed species.[84,85] Among the ionic molecules, COH^+ and HCO^+ are the only isomeric pairs of ions observed in ISM so far.[88] In the vast expanse of space, carbon monoxide plays a significant role as one of the most abundant molecules, existing in two protonated forms: the formyl cation (HCO^+) and the isoformyl cation (COH^+).[7,89] The initial discovery of HCO^+[90,91] in the interstellar medium led to extensive theoretical[92–100] investigations, but the literature on COH^+ is limited.

COH^+, a metastable isomer of HCO^+, was first observed in 1983.[101] Both these species are formed through the interaction of CO and H_3^+, but COH^+ is more susceptible to destruction by H_2 due to its higher activation barrier, resulting in its quick conversion to HCO^+.[102,103] The energy difference between the COH^+ and HCO^+ is

found to be ∼163 kJ mol^{-1}, which suggests the formation of the former cation in the laboratory is rare.[104,105] However, COH^+ has been observed in interstellar space where chemical reactions are collisionally controlled, although it is less abundant than the formyl cation. The formation and destruction mechanisms of the isoformyl cation and the abundance ratio of both cations have garnered significant interest.[23,106,107]

Observations of COH^+ have been conducted in different molecular clouds, providing valuable insights into its characteristics. Two astronomical studies for COH^+ have been performed, first by Woods *et al.* showing J=1→0[101] transitions as foremost spectroscopic detection and second by Ziurys *et al.* for J=2→1 and J=3→2[108] towards SgrB2. COH^+ has been found in both diffuse[109] and dense[110] molecular clouds. COH^+ is an interesting molecule because it serves as a substitute tracer for molecular H_2.[111] Many collisional dynamical studies have been devoted to HCO^+, the most stable isomer of protonated carbon monoxide, determining the rate of rotational transitions with the most abundant species, i.e., H_2 and He,[94–97,99,100] but the collisional data of reactive ion, COH^+ is limited.

1.3 Outcomes of Molecular Collisions

"In the dance of collisions, the Universe creates"

Nearly more than 300 molecules[3] have been identified to date involving 16 different elements that are colliding with each other. Understanding the outcomes of molecular collisions in the interstellar medium is paramount for unravelling the possible processes shaping our Universe. Within this vast expanse, where particles are sparse, yet interactions are profound, molecular collisions play a pivotal role in dictating the chemical composition, energy distribution, and evolutionary pathways of celestial bodies.[112] These collisions involve the exchange of energy, momentum, electrons, or atoms and are broadly categorized into elastic, inelastic, and reactive collisions.[113] Elastic collision only entails the exchange of momenta between the interacting partners; there is no change in the internal energy after the collision. They remain in the same energy state before and after the collision, whereas in an inelastic collision, either they can excite or de-excite from their original energy state and hence would change the energy level. The internal states of the colliding partners transform without changes in their chemical identity. This includes rotational and vibrational excitations or de-excitations. In contrast, reactive collisions involve chemical reactions, dissociation, ionization, or charge transfer. Reactive collisions involve the formation

of new molecules through bond breaking or formation, altering the chemical composition of the colliding species. The collisional cross-section, expressed in area units, is a crucial parameter determining the rate of collision. The rate of collision between the molecules determines the efficiency of energy transfer, which further affects the spectral lines. Therefore, the calculation of the collisional rate coefficient with the most abundant species is necessary for finding the accurate abundance of any molecule.

1.4 Objective of this Thesis

To explore the abundance of chemical species in the ISM, complexes are subjected to theoretical studies. Spectroscopy is the primary tool used to investigate interstellar molecules. Estimating molecular abundances requires rate coefficients involving collision partners such as molecular hydrogen and helium. Therefore, obtaining precise measurements of rate coefficients is a crucial step in determining the physical conditions present in molecular clouds. The main aim of this thesis is to compute state-to-state cross-sections and rate coefficients under interstellar conditions. A stepwise procedure will be followed to achieve this goal.

1. To compute the potential energy surface of CNNC, NCCP, COH^+ and C_2 with the most abundant species: He and H_2.

2. To expand the potential energy surface into the appropriate functional form necessary for performing scattering dynamics, achieved using Legendre polynomials.

3. To calculate the state-to-state cross-sections of complexes at low energies based on potential energy surfaces.

4. To compute the rotational de-excitation rate coefficients at interstellar and ultracold temperatures.

1.5 Outline of the Thesis

Ground state *ab initio* potential energy surfaces are computed for interstellar molecules in collision with the most abundant species, i.e., He and H_2. Inelastic collisions are investigated and cross-sections are calculated for CNNC-He, CNNC-*para*-H_2, NCCP-He, NCCP-*para*-H_2, C_2-He and COH^+-He systems. The close coupling approach is followed to study the quantum dynamics using time-independent quantum mechanics

for the collisional partners and rotational de-excitation rate coefficients are calculated at cold temperatures. Rotational quenching rate coefficients are calculated by averaging the cross-sections for C_2-He at ultracold temperatures. Bound state and pressure broadening calculations are performed for COH^+-He complex. The thesis is structured into six chapters, which are outlined as follows:
Chapter 1 provides the introductory overview of the thesis chapter and the theoretical background. This chapter briefly touches upon the interstellar medium and the application of rotational spectroscopy in Astrochemistry, followed by a short introduction to the outcomes of molecular collisions and the selection of molecular systems.

Chapter 2 of this thesis outlines the theoretical aspects underlying the methods employed for electronic structure and quantum scattering calculations. It covers a range of methodologies, starting from the Born-Oppenheimer approximation and extending to the determination of collisional rate coefficients using the close-coupling approach, which is applicable to study inelastic collisions.

Chapter 3 is divided into two subsections. In the first subsection, collisions of CNNC with He are discussed, starting with the computation of new *ab initio* potential energy surface, extending to its quantum dynamics. The second subsection of Chapter 3 talks about the interaction of CNNC with *para*-H_2. The results of collisional cross-sections and rate coefficients are discussed.

New potential energy surfaces of NCCP-He and NCCP-*para*-H_2 are computed using a coupled-cluster method discussed in Chapter 4 followed by their scattering dynamics using CC method. Collisional rate coefficients are calculated for both systems and propensity rules are discussed.

In Chapter 5, the interaction of ionic molecule COH^+ in collision with He is studied considering its possibility to form bound states. Inelastic and pressure-broadening cross-sections are calculated for COH^+-He.

In Chapter 6, inelastic cross-sections and quenching rate coefficients are computed for C_2 with ^{3}He and ^{4}He at cold and ultracold temperatures. We also studied the isotopic effects of ^{3,4}He at ultracold temperatures.

The study's conclusion and the potential for future work are discussed in the last chapter of the thesis.

Chapter 2

Methodology

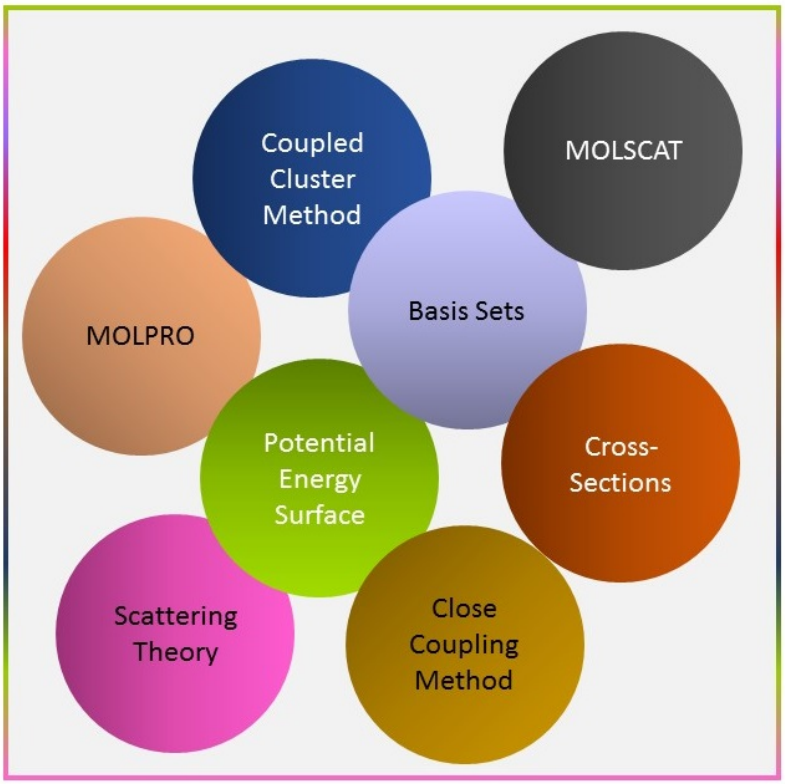

Methodology

2.1 Computational Insights into Molecular Detection in ISM

Scientific progress and advancements in computer technology have made it possible to accomplish many tasks in interstellar chemistry using computational methods that were traditionally carried out in laboratories. These methods offer remarkable accuracy. These computational methods not only aid in guiding experimental work, such as identifying new molecular species in ISM and comprehending their chemistry but also facilitate the successful detection of such species within ISM. Conditions in the ISM are characterized by low temperatures and pressures making computational studies particularly suitable that are challenging to achieve in experimental laboratories. Certain chemical species in the ISM, such as highly unstable radicals and ions, pose significant challenges for synthesis and study in laboratories but computational exploration can effectively address these challenges. Quantum chemical computations are essential in this endeavor, as they help determine spectroscopic parameters crucial for detecting these molecules. Electronic structure theory is a key field within computational chemistry focused on studying the interaction of interstellar molecules with colliders. Methods within electronic structure theory employ principles from quantum mechanics to predict molecular structures and characteristics.

2.2 Born-Oppenheimer Approximation

2.2.1 Description of Molecular Hamiltonian

In quantum mechanics, every system is described by a wave function, and Hamiltonian needs to be defined for this. The Hamiltonian operator involves the sum of electronic and nuclear energies:

$$\hat{H}(\boldsymbol{R}_A, \boldsymbol{r}_a) = \hat{T}_N(\boldsymbol{R}_A) + \hat{T}_e(\boldsymbol{r}_a) + \hat{V}_{eN}(\boldsymbol{R}_A, \boldsymbol{r}_a) + \hat{V}_{ee}(\boldsymbol{r}_a) + \hat{V}_{NN}(\boldsymbol{R}_A), \tag{2.1}$$

where $\boldsymbol{R}_A$ and $\boldsymbol{r}_a$ are the nuclear and electronic coordinates, respectively, and $\hat{T}_N(\boldsymbol{R}_A)$ is the kinetic energy operator for the nuclei:

$$\hat{T}_N(\boldsymbol{R}_A) = -\sum_{A=1}^{N} \frac{\hbar^2}{2M_A} \nabla_A^2. \tag{2.2}$$

$\hat{T}_e(\boldsymbol{r}_a)$ is the kinetic energy operator for the electrons:

$$\hat{T}_e(\boldsymbol{r}_a) = -\frac{\hbar^2}{2m_e}\sum_{a=1}^{n}\nabla_a^2. \tag{2.3}$$

$\hat{V}_{ee}(\boldsymbol{r}_a)$ is the potential energy operator for the electron-electron repulsion:

$$\hat{V}_{ee}(\boldsymbol{r}_a) = \sum_{a=1}^{n}\sum_{b<a}^{n}\frac{e^2}{4\pi\epsilon_0|\boldsymbol{r}_a - \boldsymbol{r}_b|}. \tag{2.4}$$

$\hat{V}_{eN}(\boldsymbol{R}_A,\boldsymbol{r}_a)$ is the attractive potential energy operator for the electrons and nuclei:

$$\hat{V}_{eN}(\boldsymbol{r}_a) = -\sum_{a=1}^{n}\sum_{A=1}^{N}\frac{Z_A e^2}{4\pi\epsilon_0|\boldsymbol{r}_a - \boldsymbol{R}_A|}. \tag{2.5}$$

$\hat{V}_{NN}(\boldsymbol{R}_A)$ is the potential energy operator for the nuclear-nuclear repulsion:

$$\hat{V}_{NN}(\boldsymbol{R}_A) = \sum_{A=1}^{N}\sum_{A<B}^{N}\frac{Z_A Z_B e^2}{4\pi\epsilon_0|\boldsymbol{R}_A - \boldsymbol{R}_B|}. \tag{2.6}$$

where N and n are the number of nuclei and electrons, respectively. The Hamiltonian of the system in combined form can be described as:

$$\hat{H}(R_A,\boldsymbol{r}_a) = -\sum_{A=1}^{N}\frac{\hbar^2}{2M_A}\nabla_A^2 - \frac{\hbar^2}{2m_e}\sum_{a=1}^{n}\nabla_a^2 + \sum_{a=1}^{n}\sum_{b<a}^{n}\frac{e^2}{4\pi\epsilon_0|\boldsymbol{r}_a - \boldsymbol{r}_b|} - \sum_{a=1}^{n}\sum_{A=1}^{N}\frac{Z_A e^2}{4\pi\epsilon_0|\boldsymbol{r}_a - \boldsymbol{R}_A|} + \sum_{A=1}^{N}\sum_{A<B}^{N}\frac{Z_A Z_B e^2}{4\pi\epsilon_0|\boldsymbol{R}_A - \boldsymbol{R}_B|}. \tag{2.7}$$

It's important to note that this Hamiltonian does not consider relativistic effects. For a specific system, the time-independent Schrödinger equation can be written as:

$$\hat{H}(\boldsymbol{R}_A,\boldsymbol{r}_a)\psi(\boldsymbol{R}_A,\boldsymbol{r}_a) = E\psi(\boldsymbol{R}_A,\boldsymbol{r}_a). \tag{2.8}$$

Here, E denotes the total energy of the system associated with the total wave function $\psi(\boldsymbol{R}_A,\boldsymbol{r}_a)$. Solving the equation 2.8 for systems with more than 2 particles is practically unfeasible due to the Hamiltonian depending on both nuclear and electronic coordinates, $\boldsymbol{R}_A$ and $\boldsymbol{r}_a$. Consequently, it becomes necessary to take approximations to solve the Schrödinger equation.

The Born-Oppenheimer (BO) approximation[21] is generally used to solve the Schrödinger equation and relies on the significant differences in mass between nuclei and electrons, resulting in a substantial difference in their velocities. The theory posits that nuclei are relatively stationary compared to electrons, allowing us to treat electrons as moving within a constant nuclear potential energy field determined by the positions of the nuclei. Consequently, the overall wave function can be expressed as the product of a nuclear wave function and an electronic wave function:

$$\psi(\boldsymbol{R}_A; \boldsymbol{r}_a) = \psi_N(\boldsymbol{R}_A)\psi_e(\boldsymbol{R}_A; \boldsymbol{r}_a). \tag{2.9}$$

Solution for the Schrödinger equation 2.9 can be derived by dividing into two parts:

(a) To solve the electronic Schrödinger equation:

$$\hat{H}_e(r_a)\psi(\boldsymbol{R}_A; \boldsymbol{r}_a) = E_e\psi(\boldsymbol{R}_A; \boldsymbol{r}_a), \tag{2.10}$$

where H_e represents the electronic Hamiltonian and E_e corresponds to the eigenvalue of the electronic wave function and the electronic energy of the system.

$$\hat{H}_e(\boldsymbol{r}_a) = \hat{V}_{eN}(\boldsymbol{R}_A, \boldsymbol{r}_a) + \hat{T}_e(\boldsymbol{r}_a) + \hat{V}_{ee}(\boldsymbol{r}_a). \tag{2.11}$$

The nuclear kinetic energy term ($\hat{T}_N$) in equation 2.1 disappears because of the assumption of fixed positions of nuclei, leaving only the nuclear potential energy term ($\hat{V}_{NN}$), which is determined solely by the nuclei's positions and remains constant. Consequently, the overall electronic energy is parametrically dependent on the nuclear coordinates ($\hat{V}_{NN}$) and is given as:

$$E_e^{\text{tot}}(\boldsymbol{R}_A) = E_e(\boldsymbol{R}_A) + \sum_{A=1}^{N}\sum_{A<B}^{N} \frac{Z_A Z_B e^2}{4\pi\epsilon_0|\boldsymbol{R}_A - \boldsymbol{R}_B|} \tag{2.12}$$

Hence, the idea of solving equation 2.10 for a fixed set of nuclear coordinates results in the generation of a potential energy surface which will be discussed in the following section.

(b) Once we get the PES, we can solve the nuclear Schrödinger equation (SE) by considering nuclear Hamiltonian:

$$\hat{H}_N = E_e^{\text{tot}}(\boldsymbol{R}_A) + \hat{T}_N(\boldsymbol{R}_A), \tag{2.13}$$

$$\hat{H_N}(\boldsymbol{R}_A)\psi(\boldsymbol{R}_A;\boldsymbol{r}_a) = E_N\psi(\boldsymbol{R}_A;\boldsymbol{r}_a). \tag{2.14}$$

The solution of the nuclear SE allows us to determine a large variety of molecular properties.

2.3 Calculation of Potential Energy Surface

Potential energy surfaces hold significance as they help us visualize and understand the graphical and mathematical relationship between potential energy and the unique molecular geometry of a system. Stationary points are the most important features of potential energy surfaces for understanding chemical reactions and reaction pathways. Qualitatively, these points correspond to flat surfaces, and mathematically, these are the points where the first derivative of the potential energy (PE) with respect to each geometric parameter equals zero. These points can be further distinguished on the basis of second derivatives of the PE according to the number of positive, negative, and zero eigenvalues (E_v) of the Hessian matrix.

For a minimum point, along the geometric parameter, x:

$$\frac{\partial^2 V}{\partial x^2} > 0. \tag{2.15}$$

For a transition state, one eigenvalue must be negative:

$$\frac{\partial^2 V}{\partial x^2} <> 0 \;\; and \;\; E_1 < 0, E_v > 0\,(v > 1). \tag{2.16}$$

The lowest point on the potential energy surface corresponds to a stable configuration and has the minimum energy.

2.3.1 *Ab Initio* Methods to Compute PES

PES is derived from fitting *ab initio* energies and aims to depict molecular energy across varying intermolecular distances. We calculate the *ab initio* energies by solving the electronic Schrödinger equation represented in equation 2.10 and often referred to as electronic structure calculation. Electronic structure methods have been used to solve the above equation within BO approximation, and Hartree Fock (HF) is the

most common and simplest method widely used. As the level of approximation is improved, the wave function's quality increases leading to more sophisticated solutions. There are a number of Softwares, like MOLPRO,[114] GAMESS, GAUSSIAN-16,[115] etc., available to carry out the high-level electronic structure calculation where these *ab initio* methods are available.

2.3.1.1 Hartree Fock Theory

HF method solves the electronic Schrödinger equation approximately and considers that the electron faces the average repulsion of remaining electrons instead of explicit repulsion. It presumes that only a single Slater determinant can approximate the complete many-electron wave function and considers the ground state configuration of the system:

$$\psi_{\text{total}} = \sum_{i=1}^{n} c_i \psi_i, \tag{2.17}$$

$$\psi_{\text{HF}} = c_0 \psi_0. \tag{2.18}$$

In the HF method, we compute the set of spin orbitals that minimize the energy, providing us with the best single determinant possible satisfied with the Pauli principle. A spin-orbital is the product of spin and spatial wave functions. HF method relies on the variational theorem, which suggests that calculated energies are always higher than the exact energy values. HF method recovers 99% of exact energy, the other 1% plays a vital role in defining the chemistry of molecules. Thus, the correlation energy (E_c) is defined as the remaining deviation from the exact energy:

$$E_c = E_{\text{exact}} - E_{\text{HF}}. \tag{2.19}$$

2.3.1.2 Coupled Cluster Method

The Coupled Cluster (CC) method is a post-Hartree-Fock method used to improve the electron correlation. Additionally, this method simplifies the treatment of Coulombic repulsion between electrons in an averaged manner, neglecting instantaneous electron interactions. CC is known to be the most accurate method for solving the SE and determining the *ab initio* energies. CC considers the basic HF method and constructs a multi-reference wavefunction using the exponential cluster operator ($\hat{T}$):

$$\Psi_{\text{CC}} = e^{\hat{T}} \Psi_{\text{HF}}, \tag{2.20}$$

where Ψ_{HF} denotes the reference HF wave function, while $e^{\hat{T}}$ represents an exponential operator expanded through Taylor series:

$$e^{T} = 1 + \hat{T} + \frac{\hat{T}^2}{2!} + \frac{\hat{T}^3}{3!} + ... = \sum_{k=0}^{\infty} \frac{\hat{T}^k}{k!}. \tag{2.21}$$

Let us define the excitation cluster operator:

$$\hat{T} = \hat{T}_1 + \hat{T}_2 + ... + \hat{T}_N. \tag{2.22}$$

Here, N denotes the number of electrons in the molecular system. $\hat{T}_1$ represents the single excitations operator, $\hat{T}_2$ denotes all double excitations operator, and so on. The $\hat{T}_i$ operator applied to Ψ_{HF} produces all possible Slater determinants corresponding to the i^{th} excited state.

$$\hat{T}_1 \Psi_{\text{HF}} = \sum_{i}^{occ} \sum_{a}^{vir} t_i^a \Psi_i^a, \tag{2.23}$$

$$\hat{T}_2 \Psi_{\text{HF}} = \sum_{i<j} \sum_{a<b} t_{ij}^{ab} \Psi_{ij}^{ab} \tag{2.24}$$

where t_i^a and t_{ij}^{ab} indicate the single-excitation and double-excitation cluster coefficients of the various determinants. Putting equation 2.22 into 2.21, $e^{\hat{T}}$ can be written as:

$$e^{\hat{T}} = 1 + \hat{T}_1 + \left(\hat{T}_2 + \frac{\hat{T}_1^2}{2}\right) + \left(\hat{T}_3 + \hat{T}_2\hat{T}_1 + \frac{\hat{T}_1^3}{6}\right) + \left(\hat{T}_4 + \hat{T}_3\hat{T}_1 + \frac{\hat{T}_2^2}{2} + \frac{\hat{T}_2\hat{T}_1^2}{2} + \frac{\hat{T}_1^4}{24}\right) + ... \tag{2.25}$$

It is noteworthy that different $\hat{T}_N$ operators commute with each other. Here in equation 2.22, products of cluster operators like $\hat{T}_2\hat{T}_1$ or $\hat{T}_1^2/2$ are known as disconnected operators and $\hat{T}_1$ or $\hat{T}_2$ or $\hat{T}_3$ are connected operators.

The most common and widely used extension of this method is coupled-cluster singles, doubles and triples (CCSDT) represented by,

$$\hat{T}_{\text{CCSDT}} = \hat{T}_1 + \hat{T}_2 + \hat{T}_3. \tag{2.26}$$

Schrödinger equation can be written as:

$$\hat{H}_e \, \Psi_{\text{CCSDT}} = E_{\text{CCSDT}} \, \Psi_{\text{CCSDT}}, \tag{2.27}$$

$$\hat{H}_e\, e^{(\hat{T}_1+\hat{T}_2+\hat{T}_3)}\, \phi_{\mathrm{HF}} = E_{\mathrm{CCSDT}}\, e^{(\hat{T}_1+\hat{T}_2+\hat{T}_3)}\, \phi_{\mathrm{HF}}, \tag{2.28}$$

which leads to the energy:

$$E_{\mathrm{CCSDT}} = \frac{\langle \phi_{\mathrm{HF}}|\, \hat{H}_e e^{(\hat{T}_1+\hat{T}_2+\hat{T}_3)}\, |\phi_{\mathrm{HF}}\rangle}{\langle \phi_{\mathrm{HF}}|\, e^{(\hat{T}_1+\hat{T}_2+\hat{T}_3)}\, |\phi_{\mathrm{HF}}\rangle}, \tag{2.29}$$

$$E_{\mathrm{CCSDT}} = E_{\mathrm{HF}} + \Delta E_{\mathrm{CCSDT}} \tag{2.30}$$

.

$\Delta E_{\mathrm{CCSDT}}$ is the correlation energy obtained from the coupled cluster calculation. The above equations are solved iteratively. The CCSDT method yields results with enough accuracy, yet it's typically applicable only to very small systems due to its high computational cost. Consequently, more convenient approaches have been incorporated to alleviate computational costs without compromising accuracy. One such method is CCSD(T),[116] where triple excitations are treated perturbatively rather than exactly as presented in the following equation:

$$E_{\mathrm{CCSD(T)}} = E_{\mathrm{HF}} + \Delta E_{\mathrm{CCSD}} + \Delta E_T. \tag{2.31}$$

Here, ΔE_T is a perturbative triples correction term which is given as:

$$\Delta E_{\mathrm{T}} = \sum_{i<j<k} \sum_{a<b<c} \frac{|\, \langle \Psi_{ijk}^{abc}|\, \hat{H}\, |\Psi_{\mathrm{CCSD}}\rangle\, |^2}{\epsilon_i + \epsilon_j + \epsilon_k - \epsilon_a - \epsilon_b - \epsilon_c}, \tag{2.32}$$

where $\langle \Psi_{ijk}^{abc}|$ represents the triple excitation determinant and $|\Psi_{\mathrm{CCSD}}\rangle$ is the coupled cluster wave function obtained from the CCSD calculation and ϵ_i, ϵ_j, ϵ_k, ϵ_a, ϵ_b, ϵ_c are the orbital energies from the reference Hartree-Fock calculation.

This method recovers about 95% of the correlation energy. CCSD(T) is widely employed in computational chemistry for its enhanced accuracy while offering reasonable computational efficiency compared to more computationally demanding methods. CCSD(T) is a size-consistent method and has a computational complexity of N^7 due to the inclusion of perturbative triples correction, which introduces higher-order terms, where N is the number of interacting particles.

Further, there is another class of method, i.e., explicitly correlated CCSD(T)-F12

method.[117,118] The term F12 is known as a correlation factor and has a form of Slater function which strongly improves the basis set convergence,

$$F12 = \frac{1}{\gamma} exp(-\gamma\, r_{12}). \tag{2.33}$$

Here, the parameter γ controls the width of the orbital and varies from molecule to molecule, and r_{12} is the radial term. There are two approximations, CCSD(T)-F12a and CCSD(T)-F12b, associated with CCSD(T)-F12 method which only differ in energy expression:[117,118]

$$E_{\mathrm{CCSD(T)-F12}} = E_{\mathrm{CCSD-F12}} + E_T. \tag{2.34}$$

CCSD-F12 methods introduce additional terms to the electronic wave function to account for electron correlation effects more accurately. In general, explicitly correlated methods stem from the observation that Slater determinants are inadequate in accurately describing wave functions at close interelectronic distances. To address this limitation, the wave function is explicitly represented in relation to these interelectronic distances. CCSD(T)-F12a yields accurate reaction and correlation energies with aVTZ basis set and the calculations are quite faster than standard CCSD(T)/aug-cc-pV5Z.[117]

2.4 Basis Sets

Choosing the right *ab initio* method isn't the sole factor influencing the accuracy of PES calculation. The selection of a basis set (BS) also holds considerable importance in these calculations. In simple terms, BS is a mathematical representation of the molecular orbitals in a specific molecule. It essentially defines the space within which each electron is confined. As the basis set gets larger, fewer restrictions are placed on the electrons, allowing for a more accurate approximation of the molecular orbitals. However, larger basis sets require more computational time. The basis set is an expansion of spatial/molecular orbitals as a linear combination of basis functions/atomic orbitals. Basis functions are further combinations of Gaussian functions. Let Φ_i represent the spatial orbitals and χ_k as basis functions:

$$\Phi_i = \sum_{k=1}^{n} c_{k_i} \chi_k, \tag{2.35}$$

where, c_{k_i} are molecular orbital coefficients. There are primarily two types of basis functions, also referred to as Atomic Orbitals (AO). These are the Slater-type orbitals (STOs) and the Gaussian-type orbitals (GTOs). STOs typically involve spherical harmonic functions, while GTOs are based on Gaussian functions. STOs are expressed in polar coordinates as follows:

$$\chi^{\mathrm{STO}}_{\alpha,n,l,m}(r,\theta,\phi) = Nr^{n-1}e^{-\alpha r}Y_{l,m}(\theta,\phi). \tag{2.36}$$

$Y_{l,m}$ and N represent the spherical harmonic functions and normalization constant, respectively. The GTO's functional forms in terms of Cartesian and polar coordinates are as follows:

$$\chi^{\mathrm{GTO}}_{l_x,l_y,l_z}(x,y,z) = Nx^{l_x}y^{l_y}z^{l,z}e^{-\alpha r^2}, \tag{2.37}$$

$$\chi^{\mathrm{GTO}}_{\alpha,n,l,m}(r,\theta,\phi) = Nr^{2n-2-l}e^{-\alpha r^2}Y_{l,m}(\theta,\phi). \tag{2.38}$$

$l_x + l_y + l_z{=}l$ is a non-negative integer specifying the type of orbital. The key difference between GTOs and STOs with respect to their radial dependence lies in the functional forms used to describe how the wave function changes with distance from the nucleus. GTOs have a r^2 ($e^{-\alpha r^2}$) and STOs have r ($e^{-\alpha r}$) dependence, respectively, and GTOs decay more rapidly than STOs as r increases. The dependence on r^2 in the exponential function makes GTOs less effective than STOs in two aspects. Firstly, at the nucleus, a GTO exhibits zero slope, whereas an STO shows a "cusp" (discontinuous derivative), causing GTOs to struggle to represent behavior near the nucleus accurately. Secondly, GTOs decay too rapidly when far from the nucleus compared to STOs, resulting in poor representation of the wave function. While both STOs and GTOs can form a complete basis, these considerations suggest that more GTOs are required to achieve a certain level of accuracy compared to STOs. In practical quantum chemistry calculations, both Gaussian and Slater basis functions are employed, with Gaussian basis sets being more common due to their computational efficiency.

2.4.1 Classification of Basis Sets

2.4.1.1 Minimal Basis Set

The basis sets are differentiated based on the number of basis functions used to express the atomic valence shells. The smallest basis sets utilize only one basis function for each atomic orbital and are referred to as minimal basis sets. STO-nG, where

n=2−6 represents minimal basis sets. The periodic table's first row elements require two s-functions (1s; 2s) and one set of p-functions. For e.g., carbon uses 5 basis functions. Minimal basis sets are mostly employed for very large molecules because of their low computational cost.

2.4.1.2 Correlation-Consistent Basis Set

For more accurate calculations, large basis sets are necessary. In double zeta (DZ) basis sets, atomic orbitals are defined by two basis functions, whereas in triple zeta (TZ) sets, there are three functions and so forth. A widely-used basis set developed by Dunning and his group,[119,120] known as aug-cc-pVnZ, is employed in our work. "aug" indicates that diffuse functions are included in the basis set, while "cc" implies correlation-consistent, meaning the functions are optimized for better performance in correlated calculations. The "p" signifies polarization functions added to all atoms. "V" denotes valence, indicating that valence orbitals are described by "n" functions, with one function dedicated to describing core orbitals. aug-cc-pVTZ and aug-cc-pVQZ basis set have 5s 4p 3d 2f and 6s 5p 4d 3f 2g orbitals, respectively, for carbon or nitrogen atoms and 46 and 80 in total basis functions, respectively.

2.4.1.3 Complete Basis Set

Generally, in computational chemistry, electronic structure calculations are performed using a finite set of basis functions. When the finite basis is expanded towards an (infinite) complete set of functions, calculations using such a basis set are said to approach the complete basis set (CBS) limit. CBS is not a basis set. Instead, it is an extrapolated estimate of results obtained using any infinitely large basis set.

2.5 Basis Set Superposition Error

In the realm of quantum chemistry, a notable challenge arises in finite basis set calculations, giving rise to a significant phenomenon known as the basis-set superposition error (BSSE). This error becomes apparent when considering the interaction energy of a complex 12, which is defined as the difference:

$$\Delta E_{\text{int}}(12) = E(12)^*_{12} - E(1)^*_1 + E(2)^*_2, \tag{2.39}$$

where $E(1)_1^*$ and $E(2)_2^*$ represent the monomer 1 and monomer 2 at infinite separation, respectively. $\Delta E_{int}(12)$ represents the interaction energy of the system. $E(12)_{12}^*$ denotes the energy of the bimolecular complex. The interaction energy described in equation 2.39 requires a correction for the BSSE. Boys and Bernardi introduced the counterpoise correction method to address this issue.[121] This correction involves compensating for the artificial stabilization by allowing individual atoms to improve their basis sets through the inclusion of functions from an empty basis set. To create this empty basis set, a "ghost" atom is introduced, possessing the basis set of the corresponding atom but lacking electrons to occupy it. By applying this procedure to both atoms involved, the BSSE can be effectively corrected. Thus, the interaction energy with the counterpoise correction applied as follows:

$$\Delta E_{\text{int}}^{\text{CP}}(12) = E(12)_{12}^* - E(1)_{12}^* - E(2)_{12}^*, \tag{2.40}$$

where $E(1)_{12}^*$ and $E(2)_{12}^*$ are the energy of monomers 1 and 2 in the presence of ghost orbital of monomers 2 and 1, respectively. Alternatively, BSSE error can be rectified by scaling or extrapolating the *ab initio* energies to reach the complete basis set limit.

2.6 Scattering Theory in Quantum Mechanics

In this section, we explain how the motion of the nuclei is addressed by solving the nuclear component of the Schrödinger equation. Here, we focus on a simple case involving a closed-shell diatomic molecule colliding with a structureless atom. The discussion centers on pure rotational transitions, as interstellar temperatures typically lead to the maximum population in the ground vibrational level in molecules. These principles can be extended to diatom-diatom collisions by considering the interaction between the angular momenta of the two molecules. Arthurs and Dalgarno were the pioneers who initially introduced the quantum treatment of collisions in 1960.[122]

The colliding systems can be studied by either the Body Fixed (BF) frame or the Space Fixed (SF) frame. Arthurs and Dalgarno[122] used the SF framework, while Curtiss and Adler[123] employed the BF framework in their scattering theory. Even though the BF coordinate system precedes the SF coordinate systems and both formulations are comparable, most of the scattering calculations have used the SF formulation. BF coordinate system represents a more convenient way to express the interaction potential energy surface for collisional systems characterized by the strong anisotropic nature of interaction potential. Additionally, in this representation, the intermolec-

ular potential is block diagonal, simplifying the evaluation of matrix elements. On the other hand, the SF frame is preferable in calculations as it eliminates the need for coordinate transformations. However, the choice between coordinate systems ultimately yields equivalent results in scattering with identical values of cross-sections.

Let us begin scattering theory by considering the inelastic collision between a rigid rotor XY and a collider Z within the space-fixed coordinate system, as depicted in Figure 2.1. R represents the distance from the center of mass of XY molecule to the

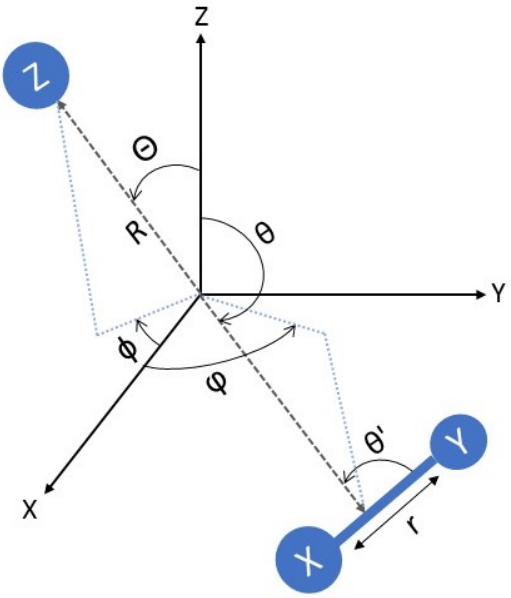

Figure 2.1: Space-fixed coordinate system

collider Z and r is the internuclear distance of XY molecule. θ, ϕ and Θ, φ are polar angles of the rotor and collider, respectively. $V(R, \theta')$ is denoted as the potential energy of the system and explains the potential within rigid rotor approximation, keeping r fixed at its optimized value in the Jacobi coordinate system θ' and R.

The kinetic energy operator ($\hat{T}_N$ in atomic units) can be written in terms of polar coordinates:

$$\hat{T}_N(R, \theta, \phi, \Theta, \varphi) = \hat{H}_{XY}(\theta, \varphi) - \frac{1}{2\mu}\nabla_R{}^2, \tag{2.41}$$

where $\mu = \mathrm{m_{XY}m_Z/(m_{XY}+m_Z)}$ represents the reduced mass.

$$\hat{H}_{XY}(\theta, \varphi) = \frac{\hat{j}^2}{2I}. \tag{2.42}$$

$\hat{H}_{XY}$ is the Hamiltonian operator of molecule XY and I is moment of inertia of XY molecule with ($\hat{j}$) its angular momentum. The kinetic energy term for the relative motion of both partners XY and Z can be divided into two parts: radial with only dependence on R and angular part and can be represented as:[122]

$$-\frac{{\nabla_R}^2}{2\mu} = -\frac{1}{2\mu R}\frac{\partial^2}{\partial R^2}R + \frac{\hat{l}^2}{2\mu R^2} \tag{2.43}$$

Here, $\hat{l}$ denotes the angular momentum of atom Z.

The time-independent Schrödinger equation is:

$$H\Psi(R,\theta,\phi,\Theta,\varphi) = E\Psi(R,\theta,\phi,\Theta,\varphi). \tag{2.44}$$

After substituting 2.41, 2.42 and 2.43 into 2.44, we get:

$$\left[-\frac{1}{2\mu R}\frac{\partial^2}{\partial R^2}R + \frac{\hat{l}^2}{2\mu R^2} + \frac{\hat{j}^2}{2I} + V(R,\theta') - E\right]\Psi(R,\theta,\phi,\Theta,\varphi) = 0. \tag{2.45}$$

During the collision, the sum of j+l=J represents the overall angular momentum and M=m_l+m_j indicates its projection along the z-axis, and ρ denotes the total parity, which remains constant. Consequently, the combined wave function can be written as a linear combination of wave functions as a function of J, ρ and M:

$$\Psi(R,\theta,\phi,\Theta,\varphi) = \sum_{J,M,\rho} C_{J\rho}\Psi^{JM\rho}(R,\theta,\phi,\Theta,\varphi). \tag{2.46}$$

J, ρ and M ensure the right boundary conditions for the complete wave function and this wave function can also be written into two parts (angular and radial) in the form of J^2, $\hat{j}^2$, J_z, j_z and ρ:

$$\Psi^{JM\rho}(R,\theta,\phi,\Theta,\varphi) = \sum_{j,l}\frac{1}{R}G_{jl}^{JM}(R)\chi_{jl}^{JM}(\theta,\phi,\Theta,\varphi), \tag{2.47}$$

where $\chi_{jl}^{JM}(\theta,\phi,\Theta,\varphi)$ is the angular part described by spherical harmonics, which is further given as follows:[122]

$$\chi_{jl}^{JM}(\theta,\phi,\Theta,\varphi) = \sum_{m_l=-l}^{+l}\sum_{m_j=-j}^{+j}\langle jlm_jm_l|JM\rangle Y_{lm_l}(\theta,\varphi)Y_{jm_j}(\phi,\Theta), \tag{2.48}$$

where $\langle jlm_j m_l | JM \rangle$ is the Clebsch-Gordan Coefficient expressing the coupling between j and l and $G_{jl}^{JM}(R)$ describes the radial part of the wavefunction which only depends on R. After substituting the equation 2.47 into equation 2.45, we get the nuclear SE as:

$$\sum_{j,l} \left[-\frac{1}{2\mu R} \frac{\partial^2}{\partial R^2} R + \frac{\hat{l}^2}{2\mu R} + \frac{\hat{j}^2}{2I} + V(R,\theta') - E \right] \frac{1}{R} G_{jl}^{JM}(R) \chi_{jl}^{JM}(\theta,\phi,\Theta,\varphi) = 0. \tag{2.49}$$

The values of $\hat{l}^2$ and $\hat{j}^2$ operator acting on angular part is given as:

$$\hat{j}^2 \left| jlJM \right\rangle = j(j+1) \left| jlJM \right\rangle, \tag{2.50}$$

$$\hat{l}^2 \left| jlJM \right\rangle = l(l+1) \left| jlJM \right\rangle. \tag{2.51}$$

Equation 2.49 can be represented as:

$$\sum_{j,l} \chi_{jl}^{JM}(\theta,\phi,\Theta,\varphi) \left[\tfrac{1}{R} \tfrac{\partial^2}{\partial R^2} R - \tfrac{l(l+1)}{R^2} + 2\mu E - \tfrac{2\mu}{2I} j(j+1) \right]$$
$$= 2\mu \sum_{j,l} \frac{1}{R} G_{jl}^{JM}(R) V(R,\theta') \chi_{jl}^{JM}(\theta,\phi,\Theta,\varphi). \tag{2.52}$$

Expressing k_j as the channel wave number such that,

$$k_j = \left[2\mu (E - E_j) \right]^{\frac{1}{2}}, \tag{2.53}$$

where E-E_j=E_k denotes the kinetic energy of the incident particle and $E_j = \frac{\hbar^2}{2I} j(j+1)$ is the free rotational energy.

The final SE becomes:

$$\left[\frac{\partial^2}{\partial R^2} - \frac{l(l+1)}{R^2} + k_j^2 \right] = 2\mu \sum_{j',l'} \left\langle j'l'JM \right| V(R,\theta) \left| jlJM \right\rangle G_{j'l'}^{JM}(R). \tag{2.54}$$

$\left\langle j'l'JM \right| V(R,\theta) \left| jlJM \right\rangle$ expresses the matrix elements of potential energy surface. The boundary conditions for the equation 2.54 are as follows:

$$\lim_{R \to 0} G_{jl}^{JM}(R) = 0, \tag{2.55}$$

and

$$\lim_{R\to\infty} G_{jl}^{JM}(R) = \delta_{jj'}\delta_{ll'} exp\left[-i\left(k_j R - \frac{1}{2}l\pi\right)\right] - \left(\frac{k_j}{k_{j'}}\right)^{\frac{1}{2}} S^J(jl;j'l') exp\left[i(k_{j'j}R - \frac{1}{2}l'\pi)\right]. \tag{2.56}$$

$S^J(jl;j'l')$ is the scattering matrix containing all the information related to the collision.

$T^J(jl;j'l')$ represents the transitions matrix element associated with $S^J_{jj'll'}$ as:[122]

$$T^J(jl;j'l') = \delta_{jj'}\delta_{ll'} - S^J_{jj'll'}. \tag{2.57}$$

Once the S-matrix elements are known, the differential and integral cross-sections can be calculated by averaging over m_j and summing over $m_{j'}$:

$$d\sigma(j;j'|\theta) = \frac{1}{k_j^2(2j+1)} \sum_{J_1=0}^{\infty} \sum_{l_1=|J_1-j|}^{J_1+j} \sum_{l_1'=|J_1-j'|}^{J_1+j'} \sum_{J_2=0}^{\infty} \sum_{l_2=|J_2-j|}^{J_2+j} \sum_{l_2'=|J_2-j'|}^{J_2+j'} (i)^{-l_1+l_1'+l_2-l_2'} \times T^{J_1}(j'l_1';jl_1) * T^{J_2}(j'l_2';jl_2) K(J_1l_1'l_1;J_2l_2'l_2;j'j|\theta) d\phi, d\Theta, \tag{2.58}$$

where

$$K(J_1l_1'l_1;J_2l_2'l_2;j'j\,|\theta\rangle) = (2l_1+1)^{\frac{1}{2}}(2l_2+1)^{\frac{1}{2}}\pi \times \sum_{m_j=-j}^{+j} \sum_{m_{j'}=-j'}^{+j'} \sum_{M_1=-J_1}^{+J_1} \sum_{M_2=-J_2}^{+J_2} \sum_{M_{l'1}=-l_1'}^{+l_1} \sum_{M_{l'2}=-l_2'}^{+l_2'} (jl_1m_j0|jl_1J_1M_1)(jl_2m_j0|jl_2J_2M_2) \times (j'l_1'm_{j'}m_{l_1'}|j'l_1'J_1M_1)(j'l_2'm_{j'}m_{l_2'}|j'l_2'J_2M_2) Y_{l_1'm_1'}(\rho) Y_{l_2'ml_2'}(\phi,\Theta). \tag{2.59}$$

The integral scattering cross-section for the transition $j \to j'$ may be written in the simplest form as

$$\sigma(j;j') = \frac{\pi}{(2j+1)k_j^2} \sum_{J=0}^{\infty} \sum_{l=|J-j|}^{J+j} \sum_{l'=|J-j'|}^{J+j'} |\delta_{jj'}\delta_{ll'} - S^J_{jj'll'}(E_k)|^2(2J+1), \tag{2.60}$$

where j and j' are the molecule's initial and final rotational quantum states. We have used the close-coupling approach for calculating the integral cross-sections, and in this, the only approximation made is the truncation of rotational energy levels of molecule XY. A maximum value limits rotational states with j as j_{max}.

2.7 Collisional Rate Coefficients

The rate coefficients employed for modeling molecular spectra can be calculated by averaging the integral cross-sections using Boltzmann's Distribution principle. The collisional rate coefficient is defined as the product of the integral cross-section $\sigma(j; j')$ and relative velocity (v) of incoming atom (Z) to molecule XY:

$$k(j; j') = \sigma(j; j') \times v. \tag{2.61}$$

With the experimental constraint of obtaining rate coefficients at constant temperature, the state-to-state rate coefficients $k(j; j')$ are thermally averaged. This averaging is achieved by utilizing the Maxwellian speed distribution function $f(v)dv$ with respect to velocity (v) and the averaged rate coefficients are deduced as:

$$k(j; j')(T) \quad = \quad \sqrt{\frac{8k_BT}{\pi\mu}} \left(k_BT\right)^{-2} \int_0^\infty \sigma(j; j')(E_k)E_k \exp\left(\frac{-E_k}{k_BT}\right) dE_k, \tag{2.62}$$

where k_B presents the Boltzmann constant and kinetic energy E_k corresponds to kinetic energy, μ is the reduced mass of the van der Waals complex, and T stands for temperature.

Chapter 3

Rotational De-excitation of CNNC in Collisions with He and *para*-H_2

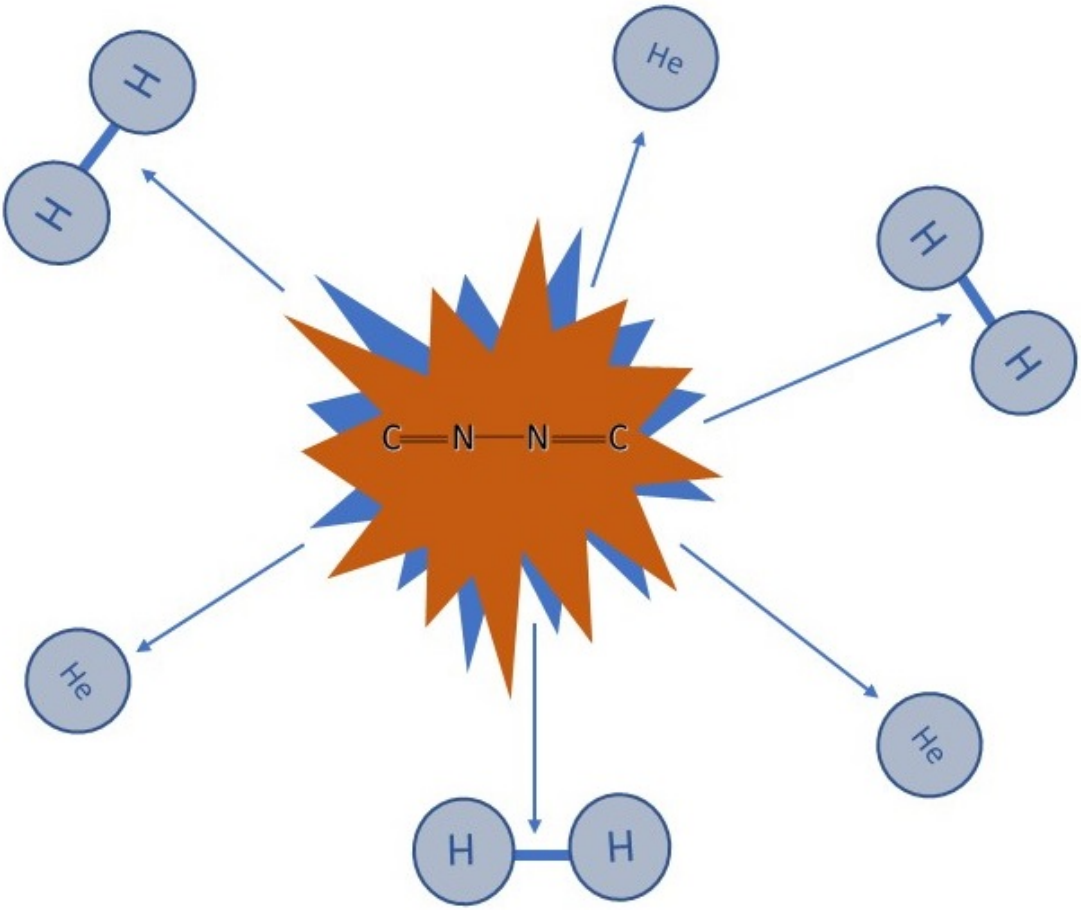

3.1 Potential Energy Surface of CNNC Collision with He

3.1.1 Adiabatic Potential Energy Curves

The calculations have been carried out by an efficient coupled cluster method involving perturbative triple excitations, i.e., the CCSD(T)-F12a method[117,118] and aug-cc-pVTZ is used as basis set[119,120] in the MOLPRO[114] package. Initially, CNNC has been optimized, and the ground state geometry of CNNC is found to be linear in a structure having the optimized C-N distance r_{CN} and N-N distance r_{NN}, which is labeled in Figure 3.1 with an $X^1\Sigma^+$ electronic ground state configuration.

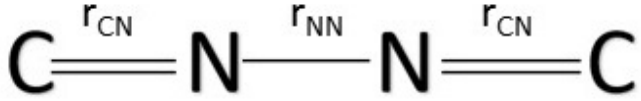

Figure 3.1: Optimized structure of CNNC.

The optimized bond *para*meters have been obtained for CNNC, CNCN and NCCN using CCSD(T)/aVTZ and CCSD(T)-F12a/aVTZ level and the available experimental parameters are reported in Table 3.1.

Table 3.1: Optimized bond *para*meters of CNNC, CNCN and NCCN molecules. Bond lengths are in Å.

	CNNC		CNCN		NCCN		
	r_{CN}	r_{NN}	r_{CN}	r_{NC}	r_{CN}	r_{NC}	r_{CC}
CCSD(T)/aVTZ	1.186	1.285	1.188	1.318	1.166	1.169	1.375
CCSD(T)-F12a/aVTZ	1.182	1.282	1.183	1.314	1.160	1.160	1.388
Experimental[124]	-	-	1.180	1.311	1.158	1.1578	1.383

The potential energy surface computed for this work models the interactions between a linear entity, CNNC, and atomic helium, and the rigid rotor approximation[122] is used. Here, calculations are performed by fixing the molecule's internuclear distances. For studying rotational transitions of CNNC by atomic He, we have deduced a two-dimensional potential energy surface (2D-PES) using the CCSD(T)-F12a method

with an aug-cc-pVTZ basis set. This computational approach is effective and accurate in constructing the potential energy surface of weakly bound complexes. This CNNC-He complex has been presented using the fixed Jacobi coordinate system r_{ij} (r_{CN}, r_{NN}), R and θ (Figure 3.2), where r_{ij} are internuclear distance in the CNNC molecule. R goes for the internuclear distance between the neutral He atom and the

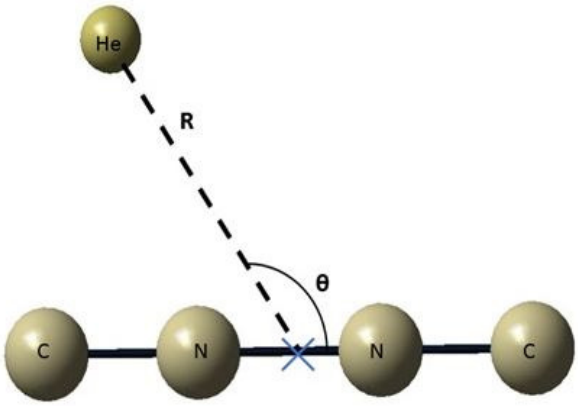

Figure 3.2: Jacobi coordinates of CNNC-He system

center of mass of the CNNC molecule and θ denotes the angle between the molecule bond vector and R. θ equals to 0° corresponds to collinearity of the CNNC-He system. Afterward, the size inconsistency of the CCSD(T)-F12a method is resolved by adjusting the global potential to the value of the potential at R equal to 100 Å and thus, the potential is allowed to decay to zero asymptotically. In addition, the counterpoise procedure of Boys & Bernardi[121] was used to correct the errors generated by the basis set superposition (see equation 3.1):

$$V(R,\theta) = E_{\mathrm{CNNC-He}}(r_{ij}, R, \theta) - E_{\mathrm{CNNC}}(r_{ij}, \infty) - E_{\mathrm{He}}(\infty). \tag{3.1}$$

Here, in these calculations, the internuclear distances were frozen at the optimized values $r_{CN} = 1.182$ Å and $r_{NN} = 1.282$ Å. 41 values are assigned to the radial scattering coordinate (R) ranging from 2.5 to 100 Å using irregular grid. For $2.5 \leq R \leq 4.5$, the grid is set to 0.1 Å, for $4.7 \leq R \leq 6.5$ to 0.2 Å, for $7.0 \leq R \leq 10.0$ to 0.5 Å. In addition, R= 20.0, 50.0, 100.0 are also calculated and the angular scattering coordinate θ is varied from 0° to 90° with 10° interval. The curves of potential energy for θ having values of 0°, 30°, 60° and 90° are shown in Figure 3.3. Due to symmetry and uniformity in CNNC [D_{∞_h}] molecule, the collisional studies are conducted from θ=0° to 90°, which would be a mirror reflection for the remaining surface (θ=90° to

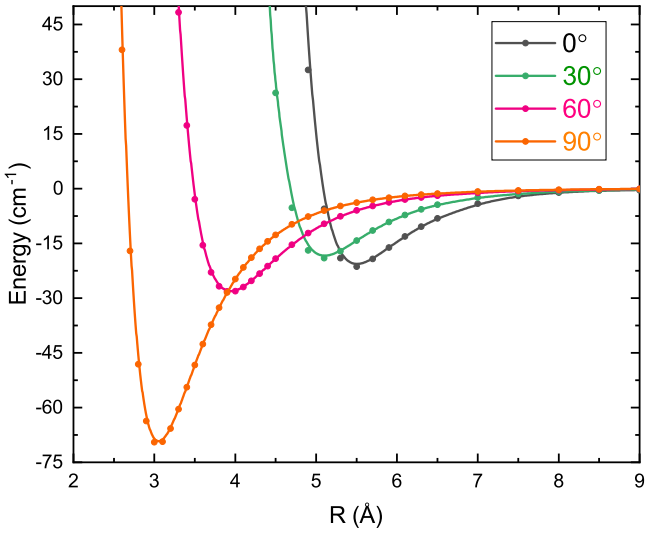

Figure 3.3: Potential energy curves of CNNC-He system for θ=0°, 30°, 60°, 90°. Bond lengths are in Å.

180°). This potential energy surface has a potential well-depth of -69.46 cm^{-1} at θ= 90° having a value of $R = 3.0$ Å as shown in Figures 3.4 (Surface) and 3.5 (Contour).[125] Like other systems associated with the cyano-He van der Waals system, i.e., NCCN-

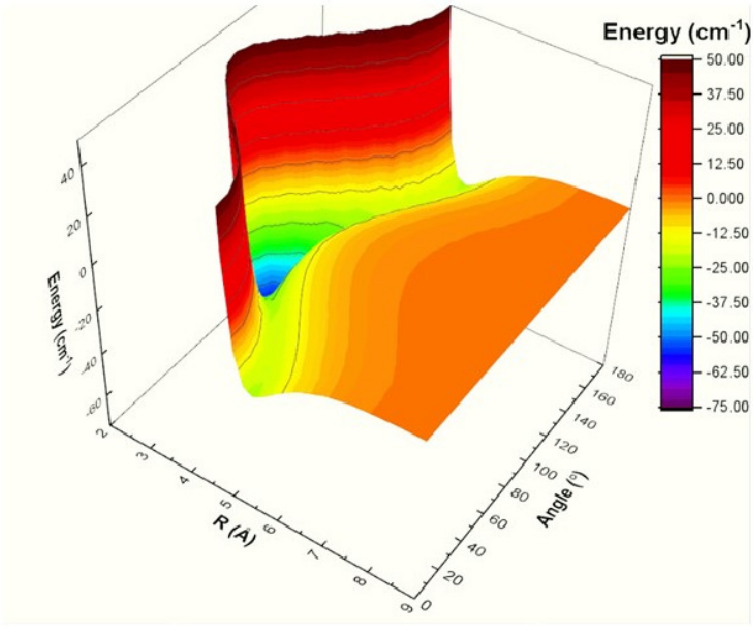

Figure 3.4: Potential energy surface of CNNC-He.

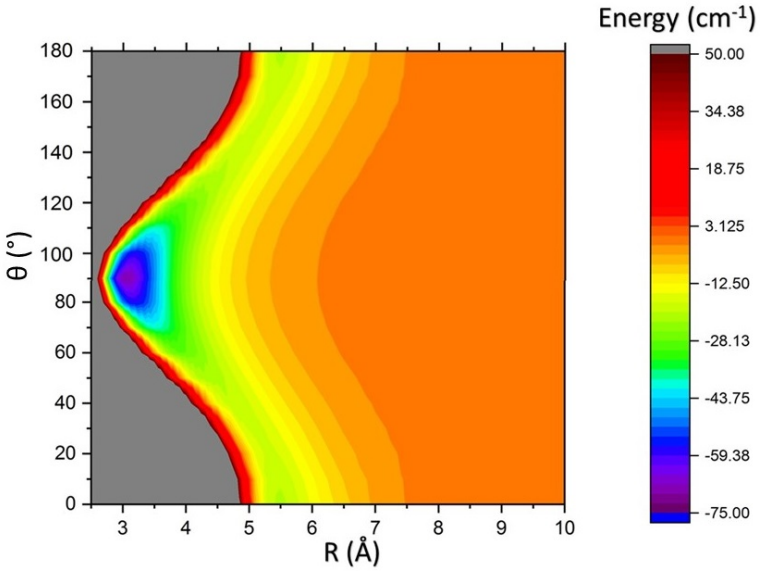

Figure 3.5: Contour plot of CNNC-He 2D-PES system. Energy values are in cm^{-1}.

He,[126] CNCN-He,[127] CCN-He,[128] CNNC system also has T-shaped geometry. Using the method of cubic spline, the potential energy surface is fitted. After comparing CNNC surface with the surfaces of other isomers, we get to know that NCCN[129] collisions with He have well-depth value of -50 cm^{-1} at R = 3.2 Å and CNCN[127] collision with He has well-depth value of -56.42 cm^{-1} at R equals to 3.1 Å at $\theta = 90°$.

3.1.2 Analytical Fit

For scattering calculations, the 2D-PES is expanded in terms of Legendre polynomial in an attempt to conduct the dynamical calculations for atom-linear rigid collisional partners as:

$$V(\theta, R) = \sum_{\lambda} V_{\lambda}(R) P_{\lambda}(cos\theta), \tag{3.2}$$

where P_λ corresponds to Legendre polynomial functions of order λ and V_λ(R) are radial functions. λ_{max} equals to 18. In *ab-initio* grid of angles, P_λ represents the number of θ. Due to the symmetric nature of CNNC, this molecule does not have a fixed dipole. Therefore, only even V_λ's exist for this collisional van der Waals complex, which has also been noticed for other few symmetric systems like NCCN,[126] C_3,[130–132] CO_2[133] etc. V_λ plot is reported in Figure 3.6.

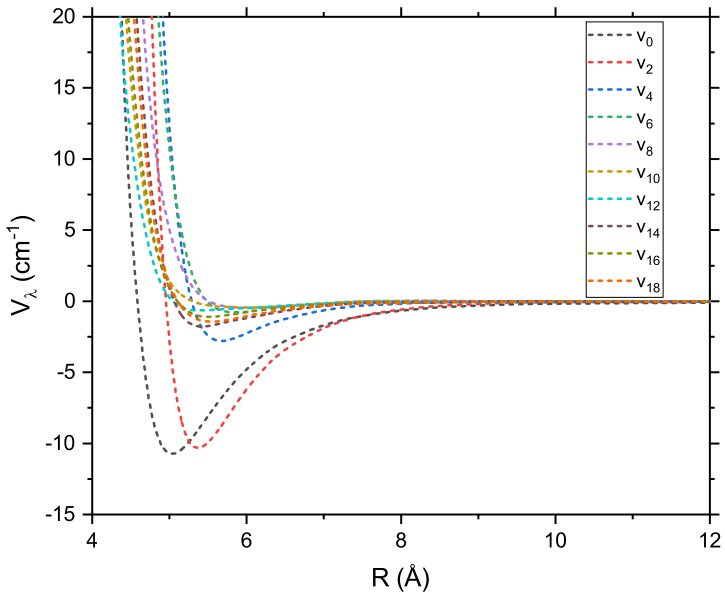

Figure 3.6: Plot of radial coefficients (λ=0-18) versus R associated with CNNC-He 2D-PES.

Here, the radial coefficients corresponding to $\lambda = 0$ and 2 strongly outweigh the others, and their potential wells exist in the attractive region of the plot, which further reduce at higher $V_\lambda^{'}s$. Further, the accuracy of analytical fit is checked, and the mean difference between the *ab initio* calculations and analytical fit calculations is less than 0.4% over the entire grid. The impact of the predominance of two radial coefficients is further shown on plots of the cross-sections and rate coefficients.

3.1.3 Rotational De-excitation of CNNC Collision with He

3.1.3.1 State-to-State Cross-Sections

In an attempt to find the integral-state-to-state inelastic cross-section, the analytical expansion of CNNC-He potential energy surface is further subsumed into quantum dynamical computations. The CC method developed by Arthurs and Dalgarno[122] is incorporated for calculating the cross-sections using the MOLSCAT[134] quantum package. It is worth mentioning that coupled equation calculations are performed using modified diabatic log derivative/AIRY propagator of Manolopoulos and Alexander.[135] In this CC approach, the rotational Hamiltonian is used as:

$H_{rot} = B_0\boldsymbol{J}^2 - D_0\boldsymbol{J}^4$

where B_0, D_0 and J correspond to rotational constant, distortion constant and rotational angular momentum operator, respectively. CNNC is linear with electronic state ($X^1\Sigma^+$) has spectroscopic constant values $B_0 = 0.1857$ cm^{-1} and $D_0 = 2.77\times10^{-8}$ cm^{-1}. B_0 has a relatively small value, resulting in dense rotational levels of CNNC. The cross-sections are computed using the scattering matrix $S^J_{jj'll'}$:

$$\sigma_{j\to j'}(E_k) = \frac{\pi}{k_j^2(2j+1)} \sum_{J=0} \sum_{l=|J-j|}^{J+j} \sum_{l'=|J-j'|}^{J+j'} \times|\delta_{jj'}\delta_{ll'} - S^J_{jj'll'}(E_k)|^2 \times (2J+1), \quad (3.3)$$

where J=j+l involves the rotational angular momentum of CNNC molecule and orbital angular momentum of the van der Waals complex, and l and l' denote the initial and final orbital angular momentum, respectively. The kinetic energy E_k is equal to E-E_j where $E_j = B_0j(j+1) - D_0j^2(j+1)^2$ is the energy of rotation and $k_j = \sqrt{2\mu E_k}/\hbar$ denotes the wave vector for the channel. In rotational de-excitation, scattering computations are performed for total energy between 0.5 and 1000 cm^{-1} using varying step size to ensure all the resonances at low values of total energy and the contributions correctly include when the corresponding rates are evaluated. The integration *para*meters are set to $R_{min} = 2.5$ Å and $R_{max} = 20$ Å. The STEPS (step size for short-range propagator) *para*meter is set large enough to create a low-energy fine integration grid. Typically, STEPS=20 corresponds to energy ≤ 120 cm^{-1} and 10 for the rest of total energy inputs up to 1000 cm^{-1}. For instance, j_{max} sets to 20 for E-value ≤ 60 cm^{-1} and progressively stepped up till j_{max}=50 for energy values upto 1000 cm^{-1} to yield converged cross-sections. Inelastic opacities have been computed as a function of l, i.e., total angular momentum is reported in Figure 3.7.[125] The convergence is guaranteed at $l = 181$ when the energy value is 500 cm^{-1}. Due to symmetry in the structure of the molecule, CNNC shows transitions corresponding to only even Δj values. Diisocyanogen has the same nuclear spin statistics as in N_2 because of the bosonic characteristics of ^{12}C(I=0) and ^{14}N(I=1) and comprises both odd and even j rotational levels in the diisocyanogen molecule.

Here, only even to even and odd to odd rotational transitions are allowed as presented in Figures 3.8(a) and 3.8(b), respectively. Odd to even and even to odd rotational transitions are forbidden. Close examination of rotational de-excitation cross-sections of CNNC-He depicts numerous resonances (Feshbach resonance and shape)[136] with prominent peaks below the energy value of 30 cm^{-1}. Feshbach resonances are the con-

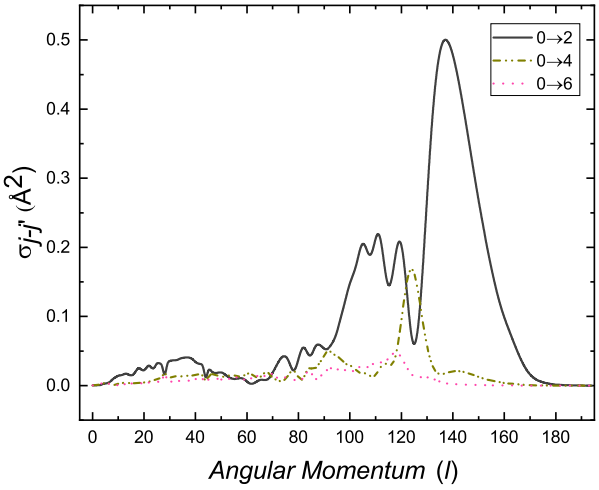

Figure 3.7: Computed opacities varying with angular momentum for cross-sections with $E = 500$ cm^{-1}.

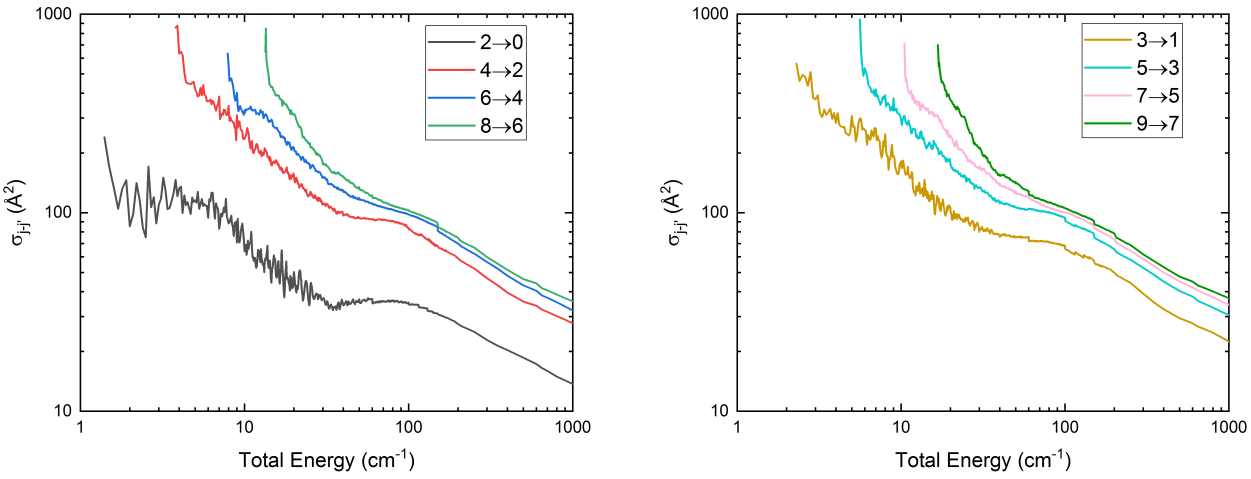

(a) (b)

Figure 3.8: Plot of rotational de-excitation inelastic cross-sections of CNNC-He with E_t for Δj=-2 where (a) even j and (b) odd j.

sequence of quasi-bound states of a closed channel when the helium gets trapped into the interaction well, whereas the shape resonances can be described as quasi-bound states that result from tunneling occurred by the centrifugal barrier of energy of an open channel. In the van der Waals potential well, the temporarily trapped CNNC-He system induces narrow spikes or dips in the value of cross-sections.[136,137] Concerning the propensity rules, we observe that transitions corresponding to even Δj values are

preferred for cross-sections, as shown in Figures 3.8(a) and 3.8(b). Figures 3.9(a) and 3.9(b) present the variation of rotational excitation and de-excitation cross-sections for j=0→j' and j'→j=0 transition, respectively. Similar excitation plots for even and

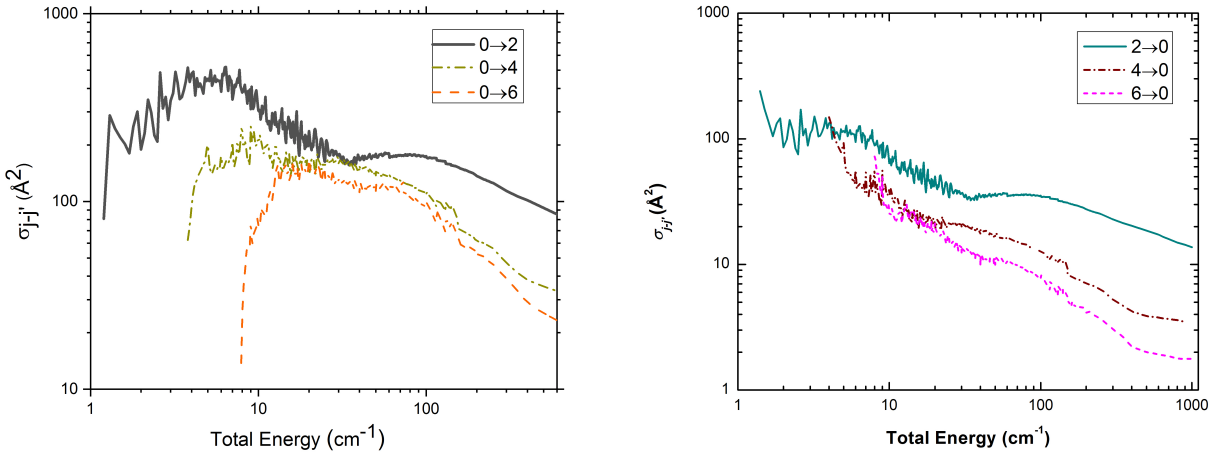

(a) (b)

Figure 3.9: Excitation and de-excitation cross-sections of CNNC-He complex for transitions (a) j=0→j' and (b) j→j'=0, respectively.

odd values of j are shown in Figures 3.10(a) and 3.10(b). The value of cross-sections

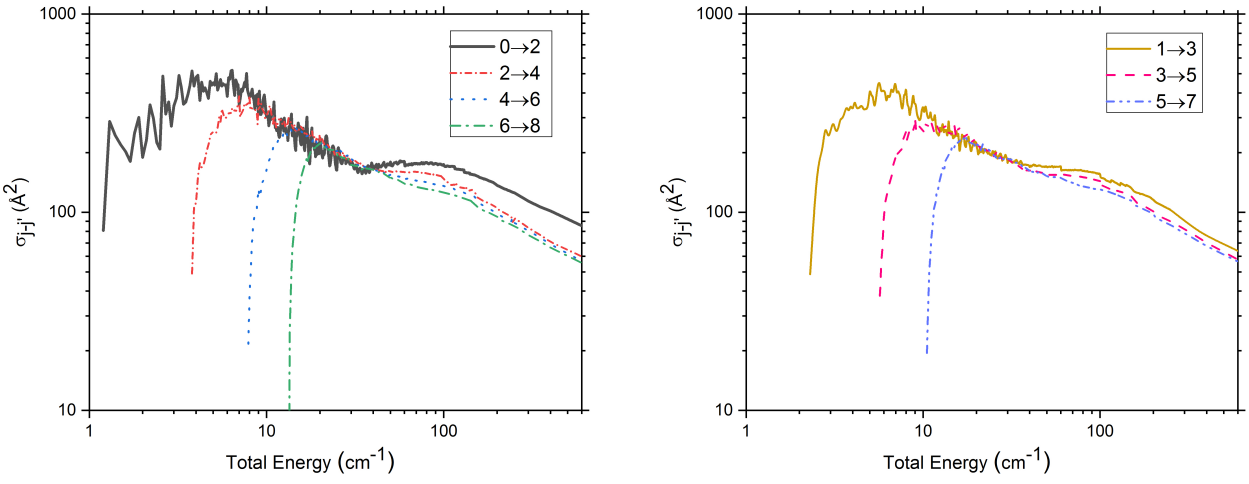

(a) (b)

Figure 3.10: Rotational excitation cross-sections of CNNC-He complex for (a) even j and (b) odd j transitions.

fluctuates at lower total energies attaining a maximum. Further, the magnitude of cross-sections decreases with the rise in energy and the plateau is achieved. For transitions corresponding to Δj=-2, the maxima in cross-sectional value for rotational

de-excitation is higher compared to those for Δj=-4, -6 as shown in Figure 3.9(b) illustrating the total energy dependence of the collisional de-excitation cross-sections. The cross-sections as a variation of initial state j are presented in Figure 3.11 at various energies. In addition, with increasing j, the cross-section trend shows an overall increase, which is a normal pattern for rotational de-excitation.

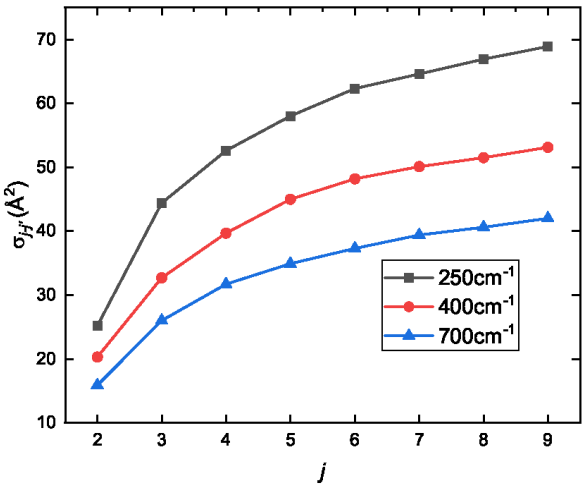

Figure 3.11: Plot of the CNNC cross-sections with initial j and Δj=-2 for E=250, 400 and 700 cm^{-1}.

3.1.3.2 Rotational Rate Coefficients of CNNC-He

These rotationally inelastic cross-sectional values obtained from the present CC calculations are thermally averaged aiming to compute the rate coefficients of CNNC due to He impact. The temperature range is kept at 1-200 K for further measurement of rate coefficients. The equation for the rate coefficient from one state j to another state j' is associated with the inelastic cross-section by the Boltzmann average as:

$$k_{j\to j'}(T) = \sqrt{\frac{8k_BT}{\pi\mu}}(k_BT)^{-2}\int_0^\infty \sigma_{j\to j'}(E_k)E_k\exp\left(\frac{-E_k}{k_BT}\right)dE_k, \quad (3.4)$$

where k_B presents the Boltzmann constant and kinetic energy E_k=E-E_j, where E_j corresponds to rotational energy, μ is the reduced mass of the van der Waals complex and T stands for temperature. The trend of rate coefficients for even and odd values of j can be analyzed correctly from Figures 3.12(a) and 3.12(b), respectively.

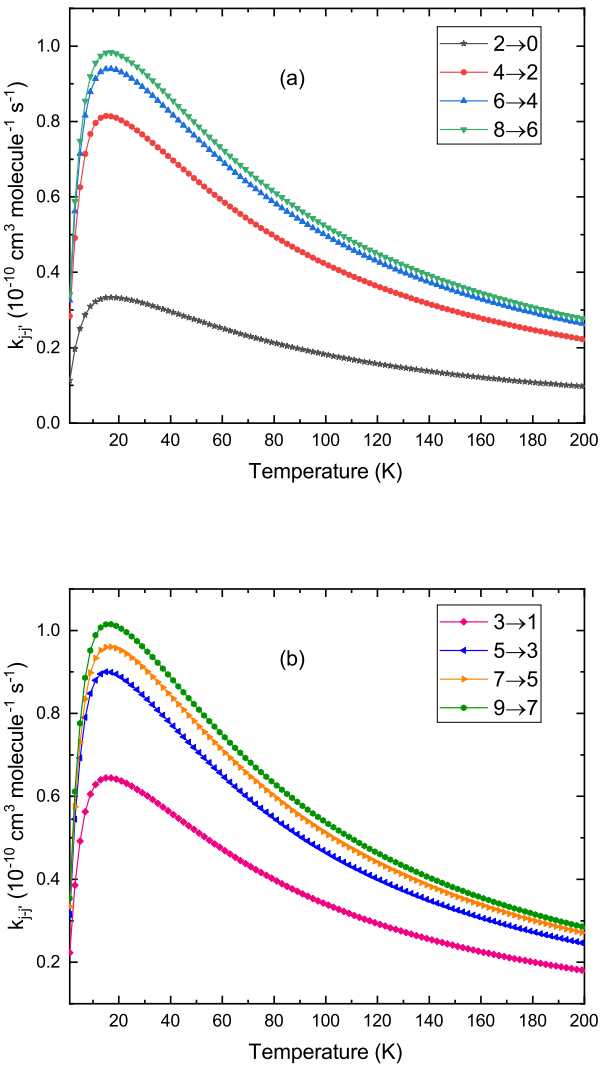

Figure 3.12: Rate coefficients for de-excitation rotational transitions of CNNC collision with atomic He from 1-200 K for (a) even value of j and (b) odd value of j for Δj=-2.

As expected from the trends of cross-section data, rate coefficient values are higher for transitions relating to Δj=-2 compared to the other higher order (Δj=-4,-6) transitions, as presented in Figure 3.13. In Figure 3.14, we depict the rate coefficients with respect to the initial rotational level j. As expected from the rotational de-excitation trend, it is mentioned that the value of coefficients of rate falls off with the decrease in j value.

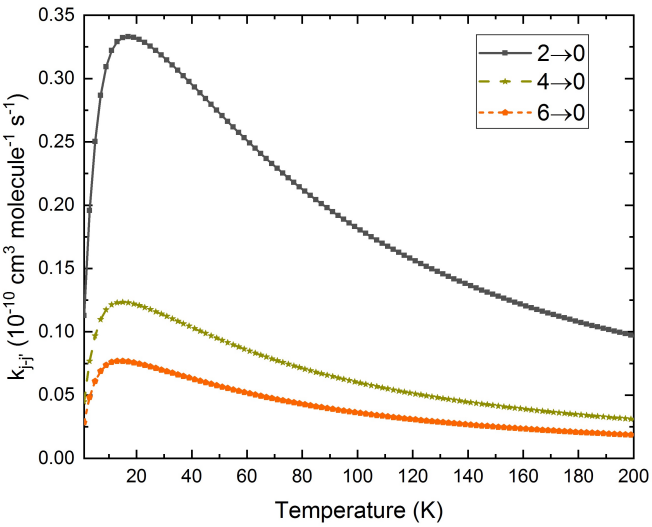

Figure 3.13: Rate coefficients of CNNC-He complex for $j \rightarrow j'=0$ for upto 200 K.

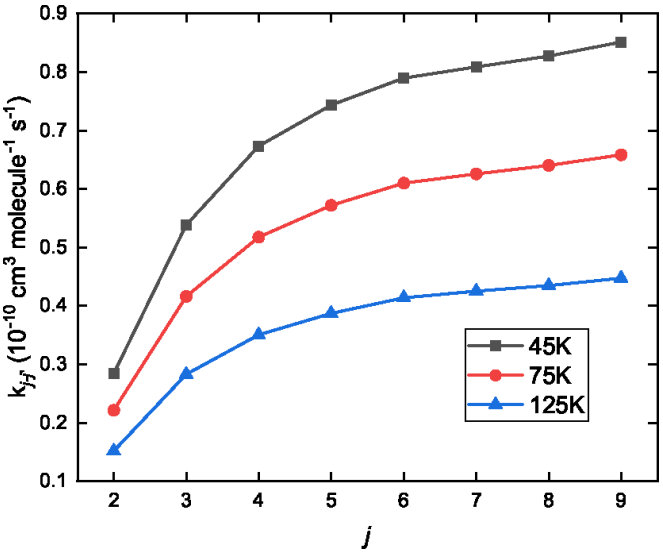

Figure 3.14: Plot of the CNNC rate coefficients with initial j and Δj=-2 for T=45K, 75K and 125K.

Collisional de-excitation studies of this system have been compared with the rate coefficients of dipole non-active C_2-He collision adapted from Najar's *et al.* work.[138] Both systems have comparable order and similar behavior, which could be explained based on the dipole property of weakly bound species. The information provided in this paper will be very useful for future astrophysical research.

3.2 Potential energy surface of CNNC collision *para*-H_2

3.2.1 Adiabatic Potential Energy Surface

The potential energy surface is based on the interaction between two linear molecules, specifically CNNC and H_2 in their ground electronic state ($X^1\Sigma^+$). The PES calculations treat both molecules as rigid or inflexible rotors. In a recent study, Faure *et al.* demonstrated that state-averaged geometries for the CO-H_2 system produced scattering results that are very similar to those of full-dimensional calculations.[139] Thus, the length of the H_2 bond is kept constant, i.e., $\langle r_{HH} \rangle$ =0.766 Å at its experimentally averaged vibrational distance. The geometry of CNNC-H_2 is represented using the Jacobi coordinate system depicted in Figure 3.15.

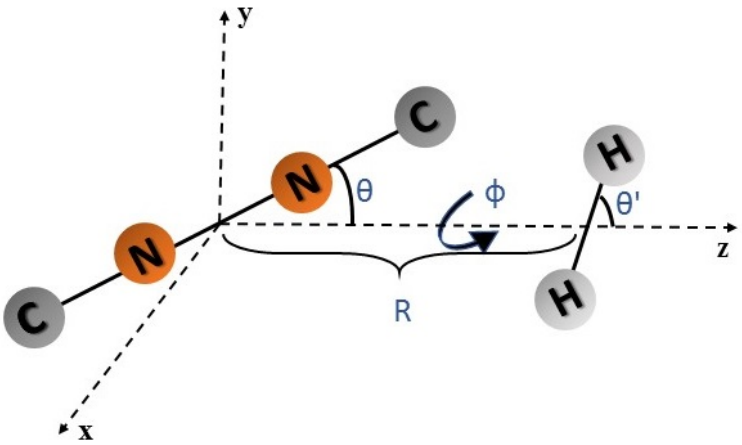

Figure 3.15: Jacobi coordinates of CNNC-H_2 system

The configuration of H_2 and CNNC is defined concerning a body-fixed system and characterized by the intermolecular distance R and three angles (θ, θ' and ϕ). The R-value defines the separation between the center of mass for CNNC and H_2, whereas θ & θ' represent the rotations of CNNC and H_2, respectively. Additionally, the symbol ϕ represents the dihedral angle that describes the relative orientation between CNNC and H_2. The monomer CNNC is kept fixed at optimized bond distances: r_{CN}=1.181 Å and r_{NN}=1.282 Å. Various CCSD(T)-F12[117,118] approximations and basis sets are tested for choosing the appropriate level of theory and the respective errors with respect to CCSD(T)/CBS in Table 3.2. Among these, the combination of CCSD(T)-F12a and aug-cc-pVTZ[119,120] yields the closest results to CCSD(T)/CBS.

Table 3.2: Values of well-depths at global minimum for θ=90°, θ'=90°, ϕ=0° and R = 3.1 Å using various levels of theory.

Level of Theory	Well-Depth (cm^{-1})	Relative Error (%)
CCSD(T)/aVQZ	215.19	2.60
CCSD(T)/aV5Z	218.59	1.09
CCSD(T)/CBS	**221.02**	-
CCSD(T)-F12a/aVTZ (CP)	221.38	0.16
CCSD(T)-F12a/aVQZ (CP)	220.38	0.28
CCSD(T)-F12b/aVTZ (CP)	217.91	1.4
CCSD(T)-F12b/aVQZ (CP)	219.34	0.76

Therefore, we have chosen to continue the PES calculations using this particular combination. All calculations are conducted using MOLPRO[114] package. To simplify the close-coupling calculations for a complete 4D surface, which is difficult due to low rotational constant of CNNC(B_0 = 0.1857 cm^{-1}), the surface is simplified by condensing it to 2D data by averaging 3 orientations (θ', ϕ) of H_2 molecule to consider the collision with *para*-H_2(j_p=0). It is occasionally possible to obtain a fair estimate of the collisional rate coefficients with *para*-H_2 from scattering calculations that do not include coupling with $j_p > 0$ levels of H_2. In fact, for collisions at low to moderate temperatures, the probability of rotational excitation of H_2 is low (the energy spacing between the $j = 0$ and $j = 2$ levels in *para*-H_2 is 510 K). Consequently, it becomes possible to confine H_2 to its lowest rotational level. In such instances, the interaction PES is derived by averaging over the angular motions of the H_2 molecule.

The values for the intermolecular distance R vary between 2.5 and 20 Å, and there are 10 values of θ in the grid, varying from 0° to 90° in steps of 10°. We have accounted three different H_2 orientations corresponding to each combination of R and θ which are given as:- (θ'=0°, ϕ=0°), (θ'=90°, ϕ=0°), (θ'=90°, ϕ=90°). Three different 2DPES, each of which is constructed similar to the CNNC-He over a grid in R and θ coordinates. The collinear arrangement of CNNC···H-H corresponds to the geometry when θ is equal to 0° and θ' is also equal to 0°. We applied the common Boys & Bernardi procedure to correct the basis set superposition error in all surface computations:[121]

$$V(R,\theta,\theta',\phi) = E_{\mathrm{CNNC-H_2}}(R,\theta,\theta',\phi) - E_{\mathrm{CNNC}}\left(r_{\mathrm{CNNC}},\infty\right) - E_{\mathrm{H_2}}\left(r_{\mathrm{H_2}},\infty\right). \quad (3.5)$$

Figure 3.16 displays the computed PESs. Panel (a) illustrates the interaction when H_2 is parallel to the z-axis, and panel (b) shows the PES where H_2 in the y-z plane

and perpendicular to the z-axis. In Panel (c), the PES is presented with H_2 lying in both the x-z plane and perpendicular to the z-axis and y-z plane, and panel (d) shows the spherically averaged 2D surface. These four plots discuss the variations in anisotropies and potential wells among different configurations of counterpoise-corrected PESs. The most pronounced of these is the global minimum of 221.38 cm^{-1} found at θ=90° & R = 3.1 Å for V(R, θ, θ'=90°, ϕ=0°). In comparison, all

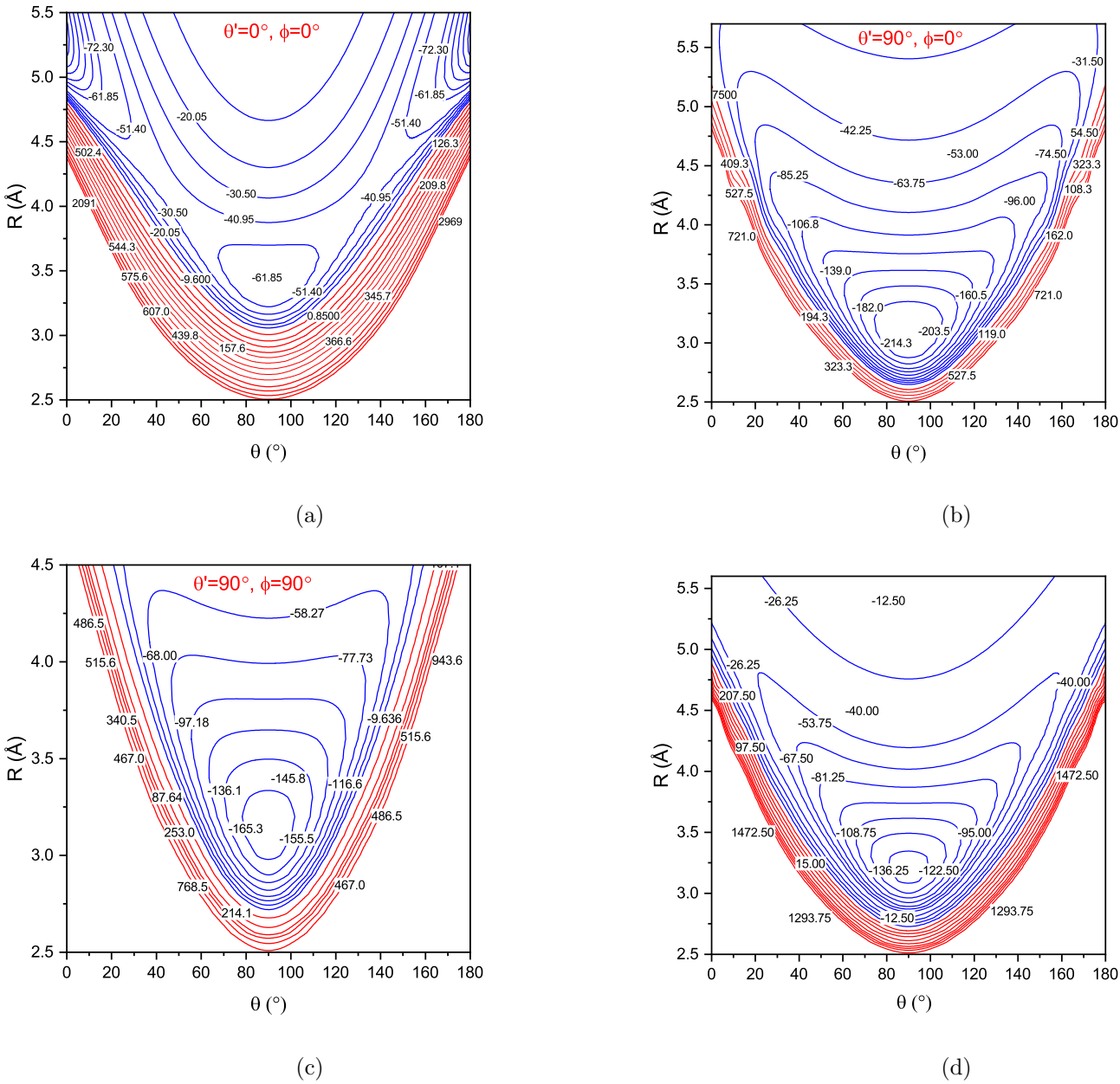

Figure 3.16: Contour plots for 3 configurations (ϕ,θ'): plot **(a)** depicts (0°,0°) configuration, plot **(b)** corresponds to (0°,90°), plot (c) shows for (90°,90°) and plot (d) for spherically averaged 2DPES with θ ranging from 0° to 180°.

other orientations exhibit lower well-depth. Specifically, a well with a depth of 168.95 cm^{-1} is located at R = 3.1 Å and θ=90° for V(R, θ, θ'=90°, ϕ=90°). Another configuration, V(R, θ=0°, θ'=0°, ϕ=0°) has a minimum at 130.45 cm^{-1} when R = 5.31 Å.[140] Consequently, the spherically averaged 2DPES takes the shape of V(R, θ, θ'=90°, ϕ=0°). However, it's important to note that the location of the potential well is at [R, θ] = [3.2 Å, 90°] and the well-depth is determined to be 143.38 cm^{-1}. It is interesting to compare the similarities and differences between our computed reduced PES for CNNC-H_2 and the PES for CNNC-He obtained using a similar theoretical approach.[141] Both PESs exhibit similar overall behavior, with global minima at an angle of 90°, but the depth of the well for CNNC-He was 69.46 cm^{-1} at R = 3.0 Å, which differs from reduced CNNC-H_2. This well-depth value of CNNC-*para*-H_2 also aligns with the reduced well-depth value of NCCN-*para*-H_2, which is 113 cm^{-1}.[142]

3.2.2 Analytical Fit

To obtain the fundamental data required for quantum dynamic calculations, cubic spline interpolation is employed on a specific mathematical function known as the Legendre polynomial function. The average value of the interaction potential ($V_{av}(\theta,R)$) is calculated by taking the mean of the overall potential energy surface based on the angular motion (θ', ϕ) of the hydrogen molecule:

$$V_{av}(\theta, R) = \sum_{\lambda} V_{\lambda}(R) P_{\lambda}(cos\theta). \tag{3.6}$$

This allows us to include up to 18 different radial (V_λ) coefficients in the expansion of the reduced 2D-PES and P_λ are Legendre polynomial functions.[140] We estimate the reduced potential energy surface by taking an average of the three potential energy surfaces using equipoise averaging:

$$V_{av}(\theta, R) = \frac{1}{3}(V_1 + V_2 + V_3), \tag{3.7}$$

where V_1=V(R, θ, θ':0°, ϕ:0°), V_2=V(R, θ, θ':90°, ϕ:0°), V_3=V(R, θ, θ':90°, ϕ:90°). Due to the symmetric nature of CNNC, only even V_λ values persist. The plot of multipole expansion coefficients as a function of radial coordinates is presented in Figure 3.17. The accuracy of the resulting fit has been checked by regenerating the potential and comparing directly with the *ab initio* computed energies. The Legendre polynomials reproduced the *ab initio* values with 0.3% . These calculations provide valuable insights into the rates of rotational de-excitation during CNNC-H_2 collisions.

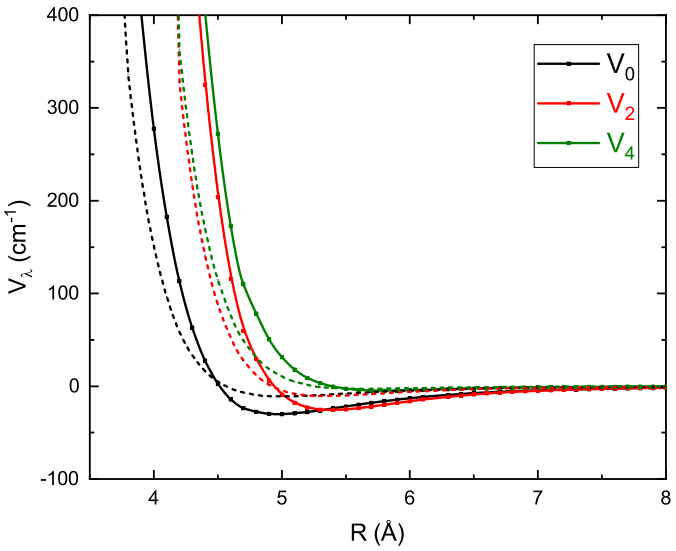

Figure 3.17: Multipolar expansion coefficients (λ=0-4) versus radial coordinate, R. Solid curves: CNNC-H_2 2DPES and dashed curves: CNNC-He.

3.2.3 Collision Dynamics of CNNC Collision with *para*-H_2

3.2.3.1 State-to-State Cross-Sections

The CC method[122] is used to calculate the integral-state-to-state inelastic cross-section for a CNNC-H_2 system using the MOLSCAT quantum package.[134] The calculations utilize the AIRY propagator, which was developed by Manolopoulos and Alexander.[135] The collisional problem is reduced to a rigid rotor by ignoring the H_2 molecule's rotational motion and the CNNC molecule's vibrational motion. The total energy range for the dynamical calculations of the collisional system is set to be between 0.5-1000 cm^{-1}. The parameters used in the propagator are R_{min}= 2.5 Å and R_{max}= 20 Å. The rotational de-excitation scattering computations are done with a step size of ΔE_t=0.1 cm^{-1} for total energies up to 50 cm^{-1}, ΔE_t=0.2 cm^{-1} for 50-100 cm^{-1}, ΔE_t=0.5 cm^{-1} for 100-150 cm^{-1}, ΔE_t=1 cm^{-1} for 150-200 cm^{-1}, ΔE_t=5 cm^{-1} for 200-250 cm^{-1}, ΔE_t=50cm^{-1} for 250-600 cm^{-1} and ΔE_t=100 cm^{-1} for 600-1000 cm^{-1}. A value of STEPS=20 is used for total energy levels below 100 cm^{-1} and STEPS=10 for E_t levels above 100 cm^{-1}. The rotational basis, symbolized by j_{max}, is set at a high enough level to include all coupling coefficients in dynamical measurements. For example, to ensure that the cross-section is converged, the value of j_{max} is set to 20 when dealing with energy values up to 60 cm^{-1} and is gradually raised to 90 for energy values up to 1000 cm^{-1}. In this optimization, the tolerance

for inelastic and elastic transitions is fixed to OTOL=0.001 Å^2 and DTOL=0.01 Å^2, respectively. CNNC has rotational energy levels that include both odd and even j values. Figures 3.18(a) and (b) illustrate how the rotational de-excitation cross-sections of CNNC change when it collides with the perturber, H_2 with respect to the total energy (E_t).[140] The analysis reveals that rotational transitions are limited to only

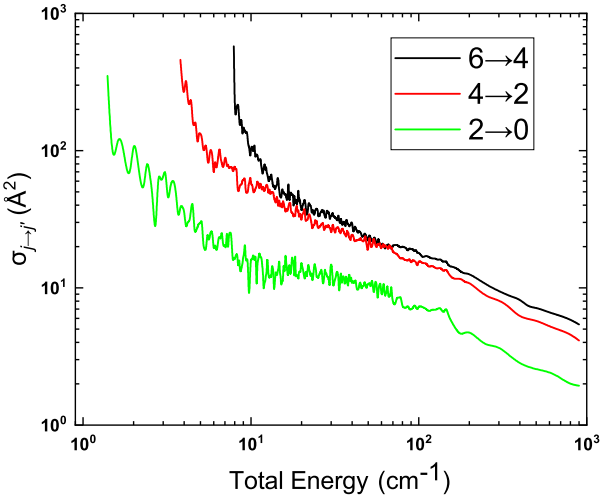

(a)

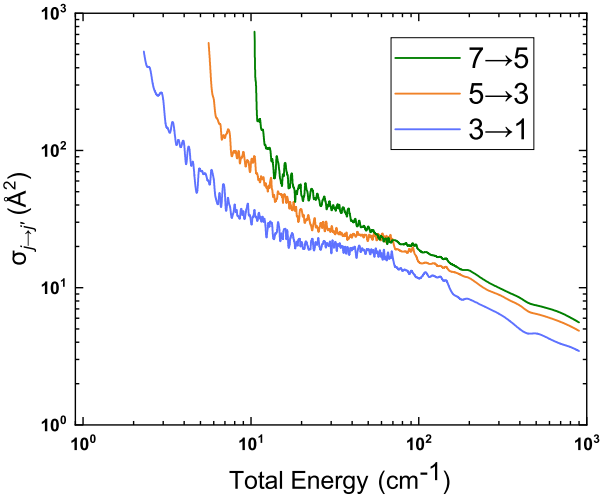

(b)

Figure 3.18: Plot of rotational de-excitation inelastic cross-sections of CNNC-H_2 with E_t for Δj=-2 where (a) even j and (b) odd j.

even-to-even and odd-to-odd transitions. Both panels show the presence of Feshbach and shape resonances[136] at energies up to E_t=200 cm^{-1}. The Feshbach resonances have large amplitudes at low energies (E_t)≤80 cm^{-1} but decrease as the total energy increases, eventually disappearing above 200 cm^{-1}. It should be emphasized that the

shapes of the cross-sections shown in this study resemble CNNC-He.[141] Furthermore, as the value of j increases, the trend for the cross-sections is a general rise, which is typical behavior for rotational de-excitation. Figures 3.18(a) and (b) illustrate the dependence of rotational de-excitation cross-sections on the energy of CNNC for both even-even and odd-odd transitions among the six rotational levels with Δj=-2. The trend remains consistent for both even and odd transitions, regardless of whether j is odd or even. In both cases, the cross-sections exhibit an increase as the transition order (j) increases (for example, from j = 2 to 6 and 3 to 7), as depicted in Figures 3.18(a) and (b), respectively. The information of variation of different Δj de-excitations and j to j'=0 transitions are provided in Figure 3.19. Here, the 2→0 transition is the most prominent among the other two (4→0 and 6→0) throughout the entire energy range. This preference will also be evident in the rotational rate coefficients.

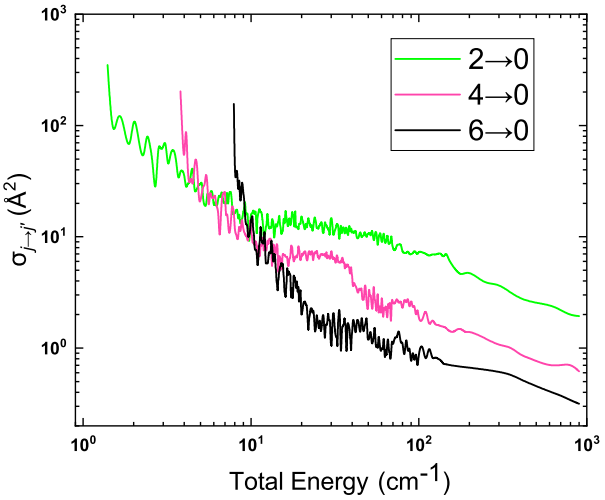

Figure 3.19: Inelastic cross-sections of CNNC-H_2 complex for $j\to j'$=0

3.2.3.2 Rate Coefficients of CNNC-*para*-H_2

The rate coefficients of CNNC resulting from *para*-H_2 impact are obtained at different temperatures from CC calculations. The rate coefficients are calculated from 1 to 100 K. The rate coefficients calculated from the cross-sections are shown in Figure 3.20 as a temperature-dependent function for the transitions. The observed trends confirm the expected presence of even Δj transitions.

During de-excitation, the highest rate occurs when transitioning from j=6 to j'=4 in Figure 3.20(a) and j=7 to j'=5 in Figure 3.20(b) and the rate decreases consistently

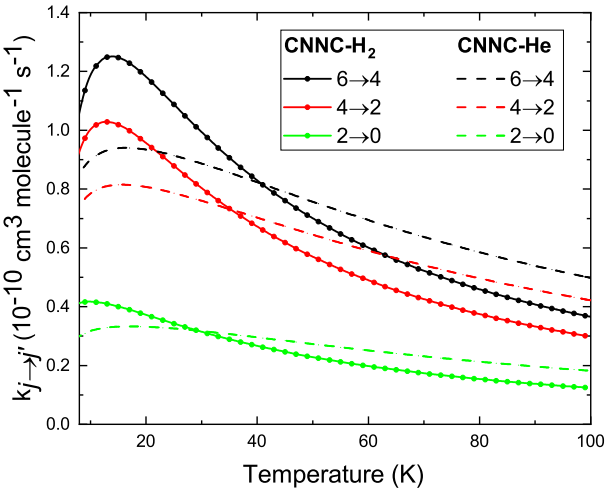

(a)

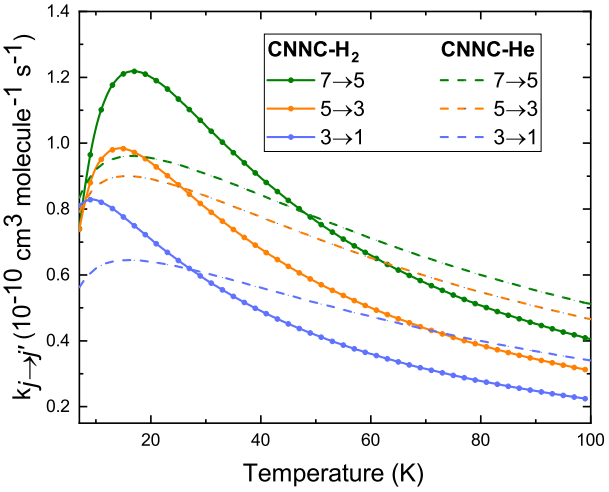

(b)

Figure 3.20: Rate coefficients of rotational de-excitation of CNNC-*para*-H_2 for Δj=-2 in the temperature range of 1-100 K for (a) even j values and (b) odd j values.

as the value of j decreases as expected. Both transitions, j=6 to j'=4 and j=7 to j'=5 exhibit similar rate coefficients. Figure 3.21 displays de-excitations (j to 0), where 2 to 0 rotational transition stands out in comparison to 4 to 0 and 6 to 0, reinforcing the previously observed trend in the cross-sections.[140] Furthermore, the obtained rate coefficients of CNNC by *para*-H_2 (j_p=0) are compared with previous rate coefficients for de-excitation of CNNC by helium. It is commonly assumed that the rate coefficients for *para*-H_2 (j_p=0) can be deduced from the He coefficients by using a scaling factor (SF) that accounts for the difference in reduced masses between H_2 and helium. The scaling factor for CNNC is found to be 1.38, which can be calculated using the

equation:

$$\mathrm{SF} = \frac{k_{\mathrm{H_2}}}{k_{\mathrm{He}}} = \sqrt{\frac{\mu_{\mathrm{CNNC-He}}}{\mu_{\mathrm{CNNC-H_2}}}} = \sqrt{\frac{3.7142}{1.9408}} = 1.38. \tag{3.8}$$

A similar methodology to the one employed in this study is used to compute a PES for CNNC-He. Figures 3.20 and 3.21 provide a comparison of rate coefficient data, contrasting the obtained results for CNNC-He with the corresponding values for CNNC-H_2. At lower temperatures, the rate coefficients for de-excitation of CNNC by He are lower compared to those with H_2. However, at higher temperatures, the rate coefficients with He surpass those for *para*-H_2. The dominant factor causing this occurrence is the anisotropy of the potential, which is more pronounced in the CNNC-He interaction compared to the CNNC-H_2 interaction. This anisotropy is significant within the well-depth region but relatively small in the long-range region, applying to both systems. This anisotropy arises from the distinct positions and well-depths of different orientations, leading to a variation in the 2DPES and a discrepancy between CNNC-He and CNNC-H_2 potentials, as shown in Figure 3.17. Since inelastic transitions primarily depend on the short-range region of potentials for higher temperatures, we expect that the calculated rate coefficients will be greater for CNNC-He compared to CNNC-H_2.

A similar pattern is observed in another symmetric molecule, specifically C_2-H_2[143,144] where k_{He} dominates over $k_{\mathrm{H_2}}$ at higher temperatures. In order to gain a deeper un-

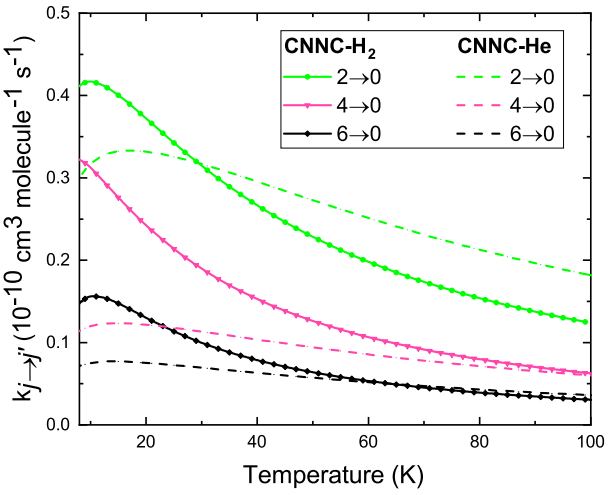

Figure 3.21: Rate coefficients of CNNC-*para*-H_2 complex for $j \rightarrow j'$=0 upto 100 K.

derstanding of the differences discussed above, a comparison is compiled in Table 3.3. The ratios of the rate coefficients ($k_{j\to j'}$), i.e., (CNNC-*para*-H_2(j_p=0)/CNNC-He), are

Table 3.3: Ratio (k_{H_2}/k_{He}) of the rate coefficients (in 10^{-10} cm^3 $molecule^{-1}$ s^{-1}) for CNNC colliding with *para*-H_2 versus He at T=10, 35 and 50 K.

j*→*j'	T=10 K	T=35 K	T=50 K
6→4	1.29	1.05	0.91
4→2	1.26	1.00	0.88
2→0	1.36	0.94	0.85
4→0	2.81	1.56	1.32
6→0	2.14	1.33	1.10
7→5	1.07	1.10	0.98
5→3	1.03	0.91	0.87
3→1	1.36	0.94	0.89

mentioned in this table. Table 3.3 reveals that this ratio is not constant and fluctuates between 0.85 and 2.81 at T=10 K, 35 K, and 50 K.[140] At lower temperatures, this ratio is approximately 1.38 for lower-order transitions, but as the temperature increases, the deviation from this expected ratio between the two sets of coefficients becomes more pronounced. This deviation highlights the importance of considering the radial terms in the potential expansion for accurate prediction of reaction rates. Based on the effect of collisional reduced mass, the data indicating *para*-H_2 with the rotational quantum number j_p=0 should show higher rate coefficients compared to He, which is consistent with our findings at low temperatures. These newly determined rate coefficients in astrophysics could potentially lead to a reassessment of the estimated abundance of CNNC in molecular clouds.

3.3 Summary

1. Modeling CNNC abundance in interstellar medium requires collisional rate coefficients with the most abundant colliders, i.e., helium and hydrogen. Quantum dynamical data is highly sensitive to interaction potentials of colliding species, which is developed for the collision between CNNC and H_2 & CNNC and He. These data are obtained by first generating the potential energy surface using accurate quantum methods. *Ab initio* PESs for collision between CNNC and He & CNNC and H_2 are computed using CCSD(T)-F12a/aug-cc-pVTZ.

2. The 4DPES of CNNC-H_2 is averaged to 2DPES using three different angular orientations for the angles ϕ and θ' at (0°,0°), (0°,90°), and (90°,90°), respec-

tively. The averaged CNNC-H_2 PES has a global minimum of 143.38 cm^{-1}, which is deeper than the minimum energy of 69.46 cm^{-1} for the CNNC-He collision, and the well-depth is found at 90° for both systems. When expanded for multipole fitting, both systems show similar trends and shapes. The deeper minimum energy of the CNNC-H_2 collision leads to a larger isotropic term v_0 by $\sim$ 20 cm^{-1}.

3. Further, rotational de-excitation cross-sections have been calculated for both systems using the CC method. The range of resonances in the CNNC-*para*-H_2 collision is broader, extending up to approximately 150 cm^{-1}, whereas the CNNC-He collision only covers a range up to 40 cm^{-1}. The effect of these differences is also clearly observed in rate coefficient plots. In both cases, only even Δj transitions are allowed. The values of the rotational de-excitation cross-section for the transition 2→0 dominate over 4→0 and 6→0. Similar trends have been observed in the case of rate coefficients.

4. The scaling factor for both systems is calculated to be 1.38, but deviations from this value are observed at higher temperatures. Overall, CNNC-H_2 rate coefficients are found to be 0.90-2.95 times those of CNNC-He rate coefficients. It is important to note that the scaling factor is not a reliable approximation for modeling *para*-H_2 collisions and can only be used for low-temperature conditions. A comparison between the present rate coefficients of CNNC-*para*-H_2 and scaled CNNC-He rate coefficients reveals discrepancies and suggests avoiding the fact of using He as a template for *para*-H_2. Despite this, similar trends and shapes of results are observed in both cases. The collision rates and other dynamical attributes computed at cold temperatures will facilitate the modeling of CNNC abundance in ISM.

Chapter 4

Collisional Properties of NCCP ($^1\Sigma^+$) in Collisions with He (^{1}S) and *para*-H_2

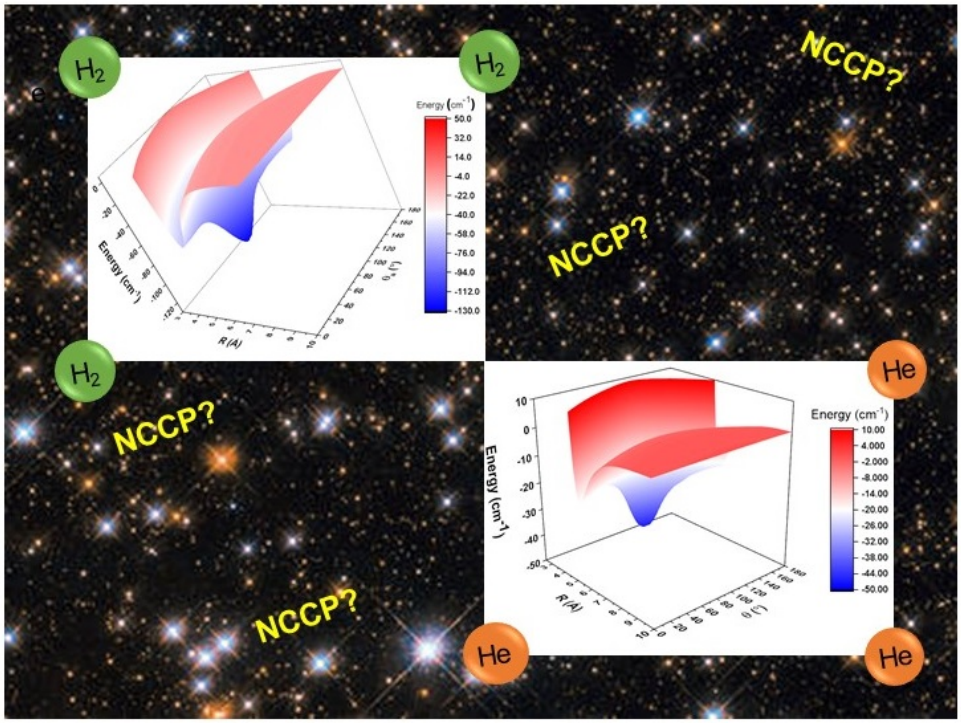

4.1 Potential Energy Surface of NCCP Collision with He

4.1.1 *Ab Initio* Calculations and PES

NCCP, a phosphorous species, is tentatively discovered in astronomical IRC+10216.[75] NCCP, being the most stable isomer among its other possible isomers, has been studied extensively both theoretically[71,72] and experimentally.[73,74] Geometry optimization is performed for NCCP using CCSD(T)-F12a/aug-cc-pVTZ in MOLPRO[114] software. The optimized NCCP molecule is found to be linear in structure with N-C distance r_{NC}, C-C distance r_{CC} and C-P distance r_{CP}. Various calculations are performed for the optimization of NCCP molecule using different levels of theory by other groups, and our bond distances match the reported and experimental results quite well, as shown in Table 4.1.

Table 4.1: Optimized bond distances of NCCP molecule

	r_{NC}(Å)	r_{CC}(Å)	r_{CP}(Å)
B3LYP/6-311G(2d)[71]	1.159	1.368	1.544
CCSD(T)/6-311++G(d,p)[72]	1.175	1.389	1.561
CCSD(T)-F12a/aug-cc-pVTZ	1.160	1.380	1.550
Experimental[72]	1.159	1.378	1.554

This NCCP-He complex has been presented using the fixed Jacobi coordinate system R and θ in Figure 4.1. R denotes the vector between the two partners, i.e.,

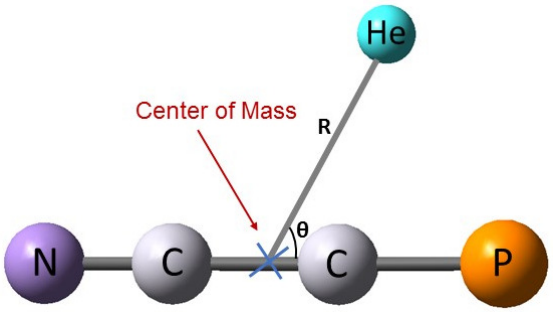

Figure 4.1: Jacobi parameters for the NCCP-He complex.

the center of mass of NCCP molecule and helium, (r_{NC},r_{CC},r_{CP}) are the internuclear distances of NCCP and θ represents the angle between the R vector and NCCP axis. The He atom approaching the P-end is represented by $\theta = 0°$. The linear NCCP molecule is considered here as rigid rotor and is kept rigid with its bond distances r_{NC} = 1.160 Å, r_{CC} = 1.380 Å, r_{CP} = 1.550 Å. R is varied from 2.5−26 Å using uniform grid with the stepsize of 0.1 Å. Uniform angular grid of 10° is choosen for θ from 0° to 180°. To remove the size inconsistency of the method, CCSD(T)-F12a at every geometry, the basis set superposition error is corrected with the help of counterpoise procedure[121] (see equation 4.1):

$$V(R,\theta) = E_{\mathrm{NCCP-He}}(R,\theta) - E_{\mathrm{NCCP}}(r,\infty) - E_{\mathrm{He}}(\infty). \tag{4.1}$$

The PES cuts for θ= 0°, 90°, 110° and 180° are depicted in Figure 4.2.

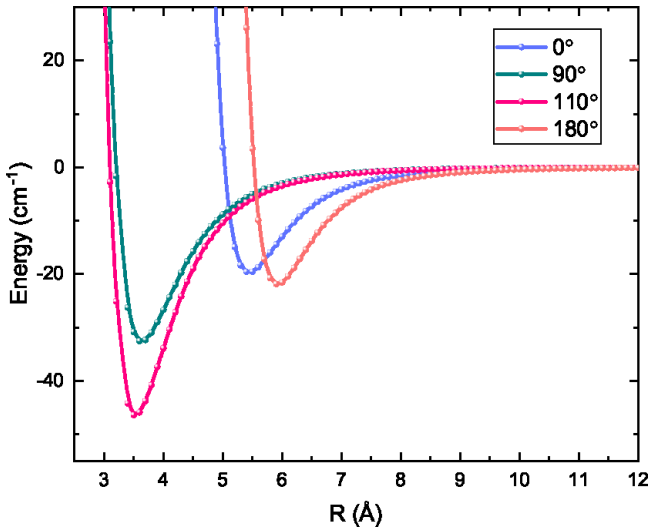

Figure 4.2: PES cuts for the NCCP-He complex for selected geometries.

With the change in orientation of He with respect to NCCP, the value of well-depth changes steadily, which can be observed in Figure 4.3. The PES cuts at $\theta = 90°$ and 180° have well-depth of -32.52 cm^{-1} and -21.87 cm^{-1}, respectively.[145] The resulting PES and contour plot are presented in Figures 4.4(a) and 4.4(b), respectively. From these figures, it is clear that this surface possesses a deeper well-depth of -46.40 cm^{-1} at R = 3.5 Å, $\theta = 110°$. We have compared our surface with P-associated surfaces such as PN[80] and HPO[146] collisions with He. The well-depth of the PN-He system is -67.26 cm^{-1} at linearity towards the P-end and well-depth of the HPO-He system is -53.22 cm^{-1} at $\theta = 70°$.

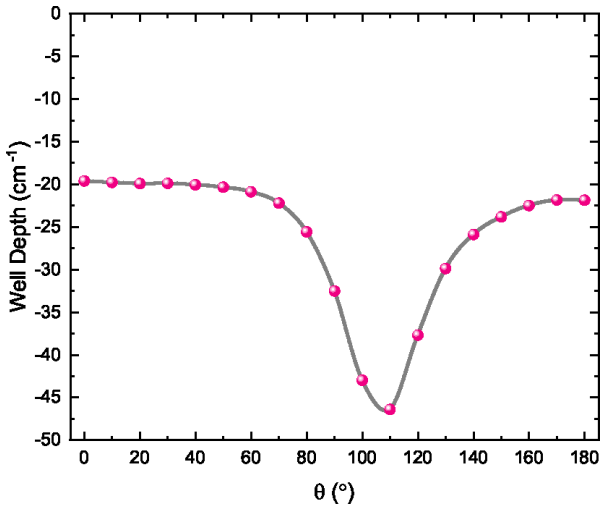

Figure 4.3: The variation of well-depth with the change in orientation θ.

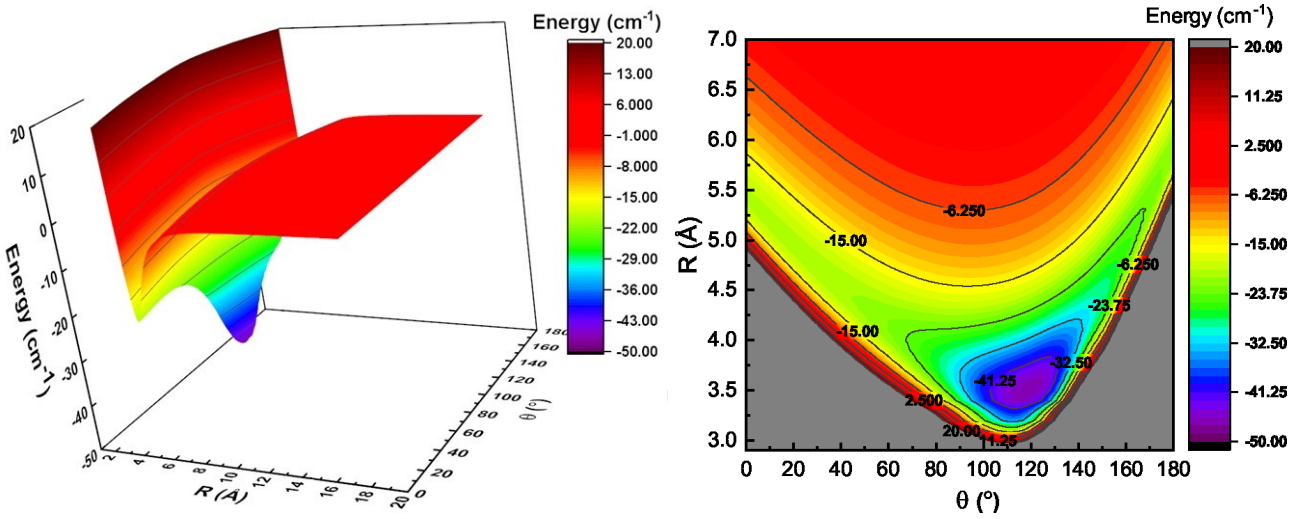

(a) (b)

Figure 4.4: Potential energy surface and contour plot as a function of θ and R.

4.1.2 Analytical Fit

For the calculations of quantum dynamics, the surface is expanded in the form of multipolar coefficients as:

$$V(\theta, R) = \sum_{\lambda} V_{\lambda}(R) P_{\lambda}(cos\theta), \tag{4.2}$$

where P_λ's are the Legendre functions of order λ. Radial coefficients are calculated for $\lambda = 0-18$. The average difference between the analytical fit and *ab initio* calculations is less than 0.4 % over the entire grid. λ varies between 0 and 3, and V_λ varies as a function of R as shown in Figure 4.5. The concavity of the curves is pointed downward

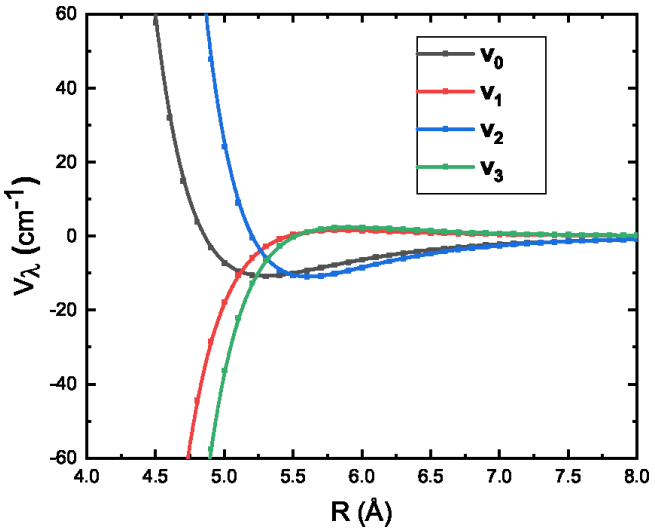

Figure 4.5: Radial coefficients as a function of R.

for $\lambda = 1$ and 3, whereas it is pointed upward for $\lambda = 0$ and 2. Similar findings are found in the works of Bop and his group[81] and Nkem's group.[147] The resulting V_λ's are utilized for the determination of collisional properties.

4.1.3 Rotational De-excitation of NCCP Collision with He

4.1.3.1 State-to-State Cross-Sections

The rotational inelastic de-excitation cross-sections are computed using the fitted NCCP−He PES. Transitions from an initial rotational state (j) to a final rotational state (j') have rotational cross-sections that can be described in the form of the scattering matrix $S_{jj'll'}$ using the equation 3.3. The molecular scattering code MOLSCAT is used to perform the quantum dynamics for this study.[134] The CC equations are integrated by adopting the modified Airy propagator of Alexander and Manolopoulos.[135] The rotational levels of NCCP are computed using the rigid rotor assumption rectified by including the centrifugal distortion (D_0). Rotational energy, E_j, is defined as $E_j = B_0 j(j+1) - D_0 j^2(j+1)^2$. The value of rotational and distortion constants[74] used in the calculations are given in Table 4.2.

Table 4.2: MOLSCAT parameters for the scattering calculations

$B_0 = 0.0902$ cm^{-1}	$D_0 = 6.708 \times 10^{-9}$ cm^{-1}
j_{max} = 20,30,35,45,50,60	$\mu = 3.7831$ a.m.u.
$R_{min} = 2.5$ Å	$R_{max} = 26$ Å
OTOL = 0.001 Å^2	DTOL = 0.01 Å^2

The non-reactive scattering calculations between NCCP and He are considered for total energies from 0.5 to 550 cm^{-1}. The energy grid between consecutive calculations increases as the energy increases: 0.1 for 0.5−120 cm^{-1}, 1 cm^{-1} for 120−160 cm^{-1}, 2 cm^{-1} for 160−200 cm^{-1}, 10 cm^{-1} for 200−500 cm^{-1}, 50 cm^{-1} for 500−550 cm^{-1}. The rotational basis j_{max} is fixed to 20 for E up to 50 cm^{-1} and successively increased to $j_{max} = 60$ for 550 cm^{-1} energy. Moreover, for inelastic (elastic) rotational transitions, the off-diagonal (diagonal) tolerance is set to OTOL = 0.001 Å^2 (DTOL = 0.01 Å^2). This complex comprises of both even and odd j rotational transitions. Figures 4.6 and 4.7 present the rotational cross-sections of NCCP-He collisions showing their dependence on total energy (E) for Δj = -1 and 5→j' transitions, respectively.

Usually, cross-sections decrease for de-excitations when the total energy increases.

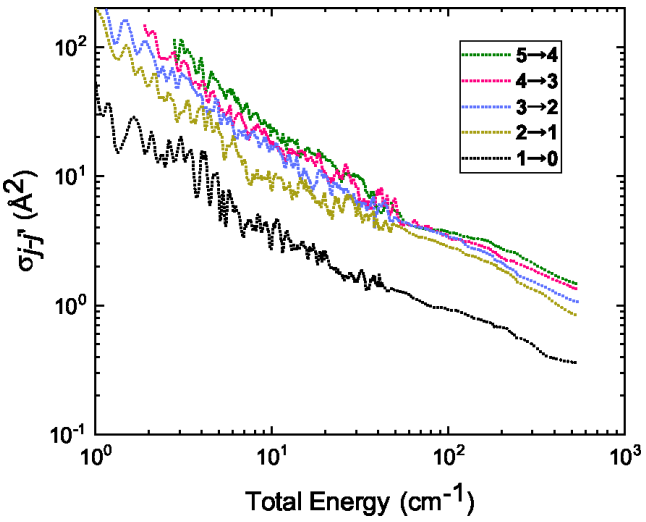

Figure 4.6: Dependence of cross-sections ($\sigma_{j\rightarrow j'}$) on the total energy (E) for Δj=-1 transitions.

Several shape resonances can be noticed for total energies less than 80 cm^{-1}. This trend relates to the decay of quasi-bound states that result from tunneling via a centrifugal energy barrier. These resonances vanish at higher energies. A similar behavior is also noticed in recent works[80–82] and NCCP-He system.[125] Furthermore,

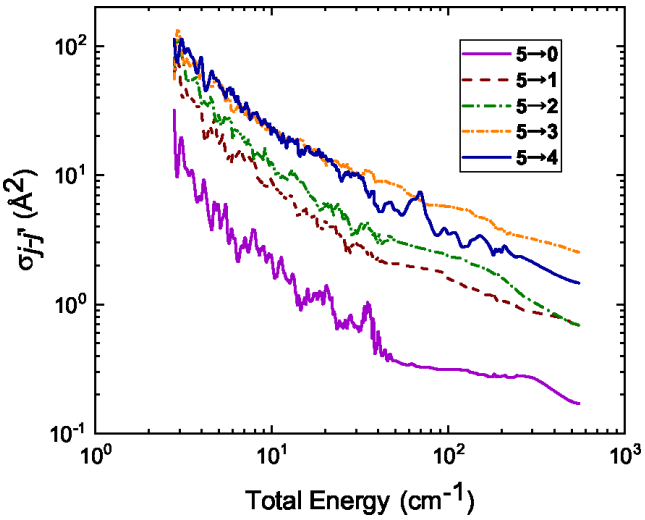

Figure 4.7: Dependence of cross-sections ($\sigma_{j\rightarrow j'}$) on the total energy (E) for j=5→j' transitions.

the cross-sections for Δj=-1 and Δj=-2 transitions rise as the value of j increases, as shown in figure 4.6. It is obvious from figure 4.7 that the cross-sections ($\sigma_{j\rightarrow j'}$) for j=5→j' transitions diminish as Δj increases. Cross-sections for 5→3 transitions predominate over 5→2, 5→1 and 5→0. The value of cross-sections decreases when the energy increases and it decreases upon decreasing the j value.

4.1.3.2 Rotational Rate Coefficients of NCCP-He

The collisional rate coefficients are computed by integrating the kinetic energy (E_k) dependence of the cross-sections ($\sigma_{j\rightarrow j'}$) at temperature T using the equation 3.4. Figures 4.8 and 4.9 display the rotational rate coefficients over a range of 3−200 K temperatures. The rate coefficients ($k_{j\rightarrow j'}$) are higher for Δj=-1 rotational transitions as compared to other rotational transitions (Δj=-2, -3, -4 and -5). For Δj=-1, the 1 → 0 transition has a minimum rate as shown in Figure 4.8, and it increases with increasing rotational level j. The comparison of present results with that of PN and HPO collisions with He[80,146] shows that PN has higher rate ($\sim 10^{-11}$ cm^3 molecule^{-1} s^{-1}) than that of NCCP and HPO ($\sim 10^{-12}$ cm^3 molecule^{-1} s^{-1}).

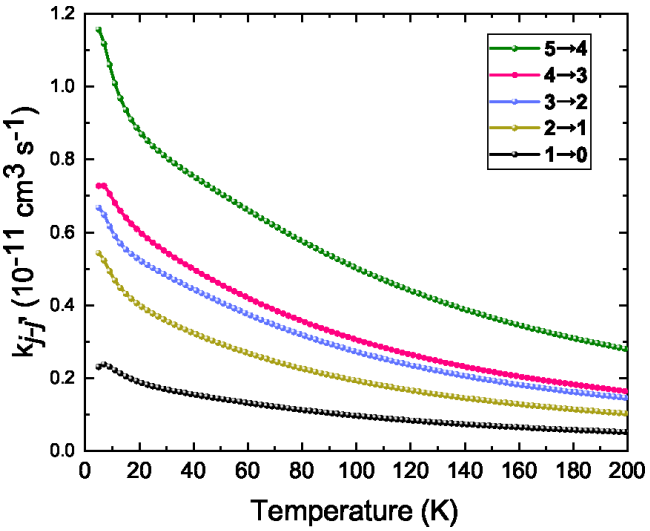

Figure 4.8: Rate coefficients with respect to change in temperature for Δj = -1 transitions.

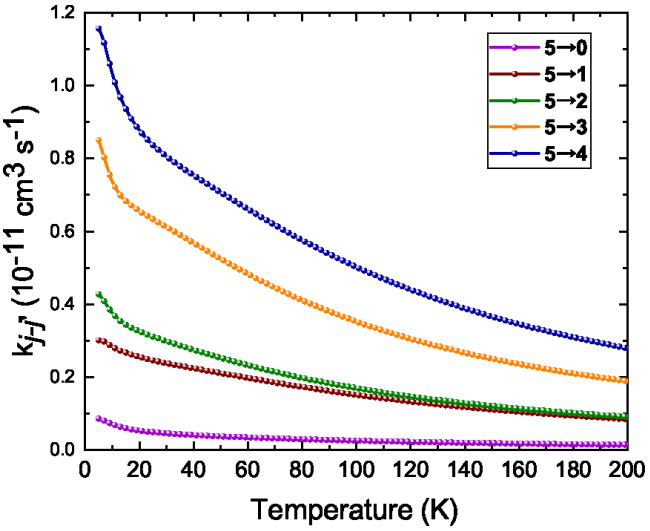

Figure 4.9: Plot of rate coefficients with respect to change in temperature for j=5→j' transitions.

4.2 Potential Energy Surface of NCCP collision *para*-H_2

4.2.1 Adiabatic Potential Energy Curves and Analytical Fit

In this study, we focus on rotational collisions between NCCP and *para*-H_2 at interstellar temperatures. Both molecules, NCCP and H_2 are treated as rigid rotors during

the PES calculations. According to a recent investigation by Faure *et al.*,[139] using state-averaged geometries yield scattering data for the CO-H_2 system that is similar to data obtained through full-dimensional calculations. Therefore, we fix the H_2 bond length at the ground vibrational level's average distance, $\langle r_{HH} \rangle$ =0.766 Å. For NCCP, we use the experimental equilibrium distance[72] with its bond distances r_{NC}=1.160 Å, r_{CC}=1.380 Å, r_{CP}=1.550 Å. The geometric parameters of the NCCP-H_2 system are described using certain angles (θ_a, θ_b, and δ) and a distance parameter (R), which represents the separation between the center of mass of both NCCP and H_2 as shown in Figure 4.10.

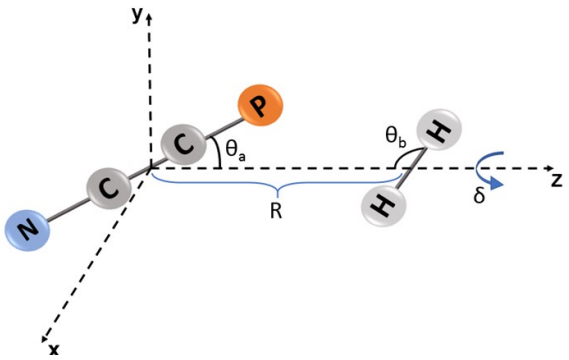

Figure 4.10: Jacobi coordinates for the NCCP-H_2.

The θ_a and θ_b denote the rotations of NCCP and H_2, respectively, relative to the z-axis and the symbol δ indicates the dihedral angle that describes the relative orientation between NCCP and H_2. The adiabatic 4DPES, which relies on the parameters θ_a, θ_b, δ and R is computed using CCSD(T)-F12a method described by Adler, Knizia and Werner[117,118] employing an aVTZ basis set.[119,120] In the F12 calculations, F12 integrals are computed using density fitting (DF) approximations. We have used the ri_basis= aVTZ/MP2FIT in PES calculations. We present a comparison in Table 4.3 where we have examined different CCSD(T)-F12 approximations and basis sets. The errors with respect to CCSD(T)/CBS are evaluated and presented in a table. It is observed that CCSD(T)-F12a/aVTZ proved to be sufficiently accurate in describing van der Waals intermolecular interactions.[7,148]

All calculations are conducted using MOLPRO[114] package. The values of R ranges from 3.0 to 26 Å and there are 19 discrete values of θ_a in the grid, ranging from 0° to 180° in increments of 10°. For each combination of R and θ_a, we consider three distinct orientations of H_2 molecules, which are given as:- (θ_b=0°, δ=0°), (θ_b=90°,

Table 4.3: Well-depth values attained for θ_a=180°, θ_b=0°, δ=0° and R = 5.7 Å at different levels of theory (LoT).

LoT	Well-Depth (cm^{-1})	Error (%)
CCSD(T)/aVQZ	188.805	1.57
CCSD(T)/aV5Z	190.244	0.82
CCSD(T)/CBS	**191.820**	-
CCSD(T)-F12a/aVTZ (CP)	191.281	**0.28**
CCSD(T)-F12a/aVQZ (CP)	190.915	0.47
CCSD(T)-F12b/aVTZ (CP)	189.465	1.22
CCSD(T)-F12b/aVQZ (CP)	191.089	0.38

δ=0°), (θ_b=90°, δ=90°). Consequently, 2964 geometries are computed for the NCCP-H_2 system in the C_s symmetry group, represented by (R, θ_a, θ_b, and δ). In all surface computations, we apply the standard Boys & Bernardi approach to rectify the basis set superposition error:[121]

$$V(R,\theta_a,\theta_b,\delta) = E_{\mathrm{NCCP-H_2}}(R,\theta_a,\theta_b,\delta) - E_{\mathrm{NCCP}}\left(r_{\mathrm{NCCP}},\infty\right) - E_{\mathrm{H_2}}\left(r_{\mathrm{H_2}},\infty\right). \quad (4.3)$$

The collinear configuration of NCCP···H-H occurs when θ_a is equal to 0° and θ_b is also equal to 0° and H-H···NCCP corresponds to the configuration when θ_a=180° and θ_b=0°. Figures 4.11 display the one-dimensional potential energy curves of NCCP-H_2 concerning the variable R. It illustrates these curves for three different orientations of H_2 at θ_a = 0°, 90°, and 180°. As evident from this figure, the potential exhibits strong anisotropy due to the orientation of H_2. The most favourable interaction arises from a collinear (H and N head-to-head) configuration of H-H NCCP (θ_a = 180° and θ_b = 0°), which is influenced by the H_2 quadrupole and NCCP dipole orientations. In the linear arrangement with angles θ_a = 0° and θ_b = 0°, the interaction is weaker due to a repulsive long-range electrostatic force between the unfavourable NCCP dipole and H_2 quadrupole orientations. When θ_a = 90°, the interaction potential shows minor dependency on the rotation of the H_2. Since our objective involves solving the CC equations to analyze scattering phenomena, expanding the PES function, V, at a given R value using angular functions is necessary. In the context of scattering between two linear rigid rotors, the potential can be represented as follows:[149,150]

$$V\left(R,\theta_a,\theta_b,\delta\right) = \sum_{l_1 l_2 \mu} v_{l_1 l_2 \mu}(R) \times P_{l_1 l_2 \mu}\left(\theta_a,\theta_b,\delta\right), \quad (4.4)$$

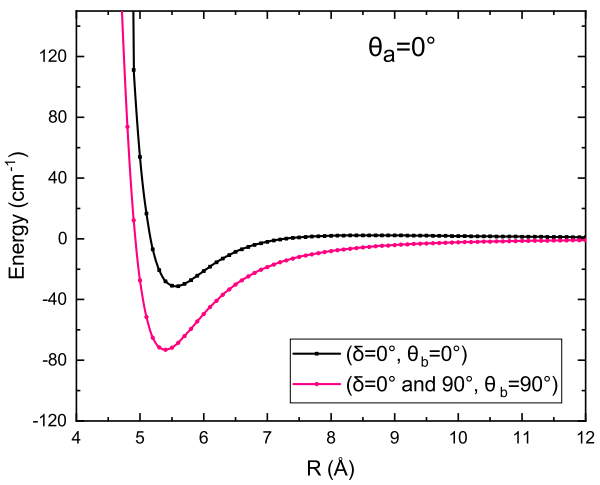

(a)

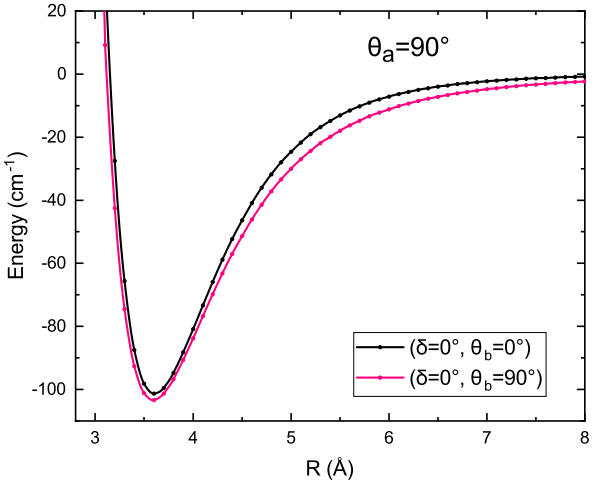

(b)

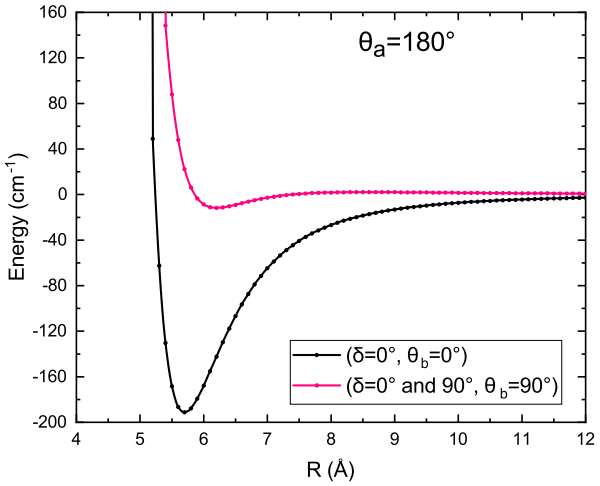

(c)

Figure 4.11: Plots depict the potential energy of NCCP-H_2 w.r.t. R are presented for various orientations, namely $(\delta,\, \theta_b) = (0°,\, 0°)$, $(0°,\, 90°)$, and $(90°,\, 90°)$. Plot (a) illustrates the case when θ_a=0°, plot (b) for θ_a at 90°, and plot (c) when θ_a is 180°.

where

$$P_{l_1 l_2 \mu}\left(\theta_a, \theta_b, \delta\right) = 4\pi \left[2\left(\delta_{\mu 0}+1\right)\right]^{-1/2} \left[Y_{l_1 \mu}(\theta_a, 0) Y_{l_2 -\mu}\left(\theta_b, \delta\right) + Y_{l_1 -\mu}(\theta_a, 0) Y_{l_2 \mu}\left(\theta_b, \delta\right)\right], \tag{4.5}$$

with $\mu \leq \min\left(l_1, l_2\right)$. Here, indexes l_1 and l_2 are connected, respectively, with the

rotational motion of NCCP and H_2. Specifically, index l_2 is even, reflecting the homonuclear geometry of the molecule H_2. In specific scenario of collisions involving *para*-H_2 molecules (where $j_p = 0$), with $l_2 = 0$, and reduced mass $\mu = 0$, the corresponding wave function simplifies to $Y_{00}(\theta_b, \delta) = 4 \times \pi^{-1/2}$. The expectation value of the potential is then deduced by averaging the total potential energy surface over the angular motion (θ_b, δ) of the H_2 entity:

$$V_{\text{av}}(R, \theta_a) = \langle Y_{00}|V|Y_{00}\rangle = \sum_l v_{l_1}(R) P_{l_1}(\cos\theta_a), \tag{4.6}$$

where P_{l_1} denotes the Legendre polynomials. Equation 4.6 has the appropriate form to expand the interaction potential between the fixed rotor and spherical projectile. As mentioned earlier, in the context of low-energy rotational excitation, the impact of the $j_p \geq 2$ channels of H_2 are ignored. Additionally, the energy difference between j_p=0 and j_p'=2 levels (510 K) is significantly larger than the thermal kinetic energy (T$\leq$150 K), suggesting that the influence of closed channels (j_p=0) on cross-sections is expected to be minor. Therefore, we have chosen to work with the minimal rotational basis of j_p=0 for *para* hydrogen. The PES for NCCP-H_2 (j_p=0) is simplified into a 2DPES, V_{av}, computed by averaging the total PES over angles θ_b and δ,

$$V_{av}(\theta_a, R) = \frac{1}{3}(V_a + V_b + V_c), \tag{4.7}$$

where

V_a=V(R, θ_a, θ_b:0°, δ:0°), V_b=V(R, θ_a, θ_b:90°, δ:0°), V_c=V(R, θ_a, θ_b:90°, δ:90°).

The spherically averaged 2DPES has a global minimum of -125.40 cm^{-1} at θ_a = 110° and R = 3.6 Å.[151] It is interesting to contrast the differences and similarities between the PES for NCCP-He and our computed reduced PES for NCCP-H_2.[145] The overall behavior of both PESs is similar, with global minima at 110°, but reduced NCCP-H_2 has a deeper well measuring -46.40 cm^{-1} at R=3.5 Å. Figure 4.12 presents the spherically averaged 2D contour plot for NCCP-H_2. For fitting the averaged surface, we have included 29 different radial (v_{l_1}) coefficients. The multipole expansion coefficients are presented in Figure 4.13 as a function of radial coordinates. Due to the asymmetric nature of NCCP, both even and odd v_{l_1} values persist. These calculations offer insightful information regarding the rotational de-excitation rates in NCCP-H_2 collisions.

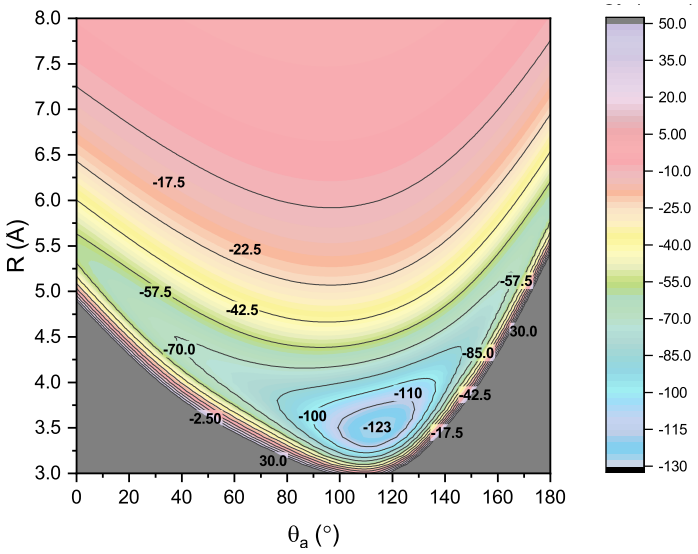

Figure 4.12: Spherically averaged 2D contour plot for NCCP-H_2 as function of θ_a and R.

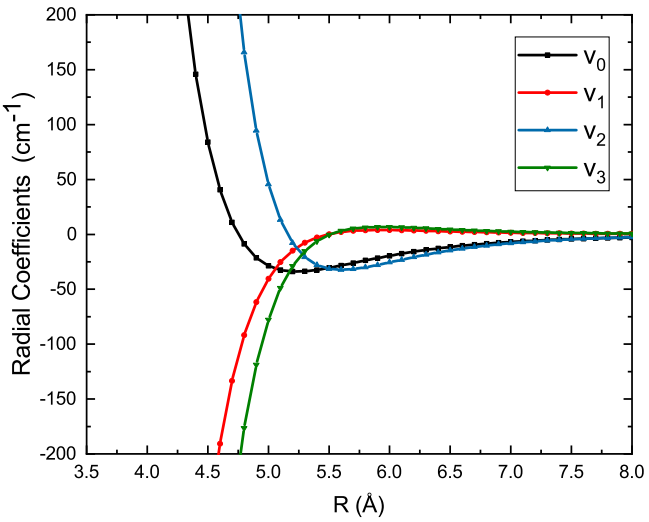

Figure 4.13: Multipolar expansion coefficients versus R for NCCP-H_2 at λ=0-3.

4.2.2 Collision Dynamics of NCCP Collision with *para*-H_2

4.2.2.1 Computational Details and De-excitation Cross-Sections

The CC method formulated by Arthurs, Dalgarno & Bates[122] is employed for the determination of the integral inelastic cross-section between different quantum states for NCCP-*para*-H_2 system using the MOLSCAT quantum package.[134] The calculations

are done using the AIRY propagator.[135] The NCCP possesses spectroscopic attributes denoted as B_0 (0.0902 cm^{-1}) and D_0 (6.708×10^{-9} cm^{-1}), and it has a linear configuration in its electronic state ($X^1\Sigma^+$). The collisional problem is limited to a rigid rotor by disregarding the H_2 rotational motion and the NCCP vibrational motion. The range of total energy considered for the dynamic computations spans from 0.5 to 600 cm^{-1}, encompassing all resonances. The parameters of the propagator are adjusted to strike a balance between accuracy and computational efficiency. Notably, R_{min} is set at 3.0 Å while R_{max} is set at 26 Å. Typically, STEPS=10 is set for E_t levels greater than 100 cm^{-1}, and STEPS=20 is used for E_t levels less than 100 cm^{-1}. The parameter j_{max} is initially configured at 20 for energy levels ranging up to 60 cm^{-1}, with a gradual increment to 60 for energy levels extending up to 600 cm^{-1}. Figures 4.14(a) and 4.14(b) indicate the de-excitation cross-section variation with respect to the total energy when it interacts with the perturber, H_2. The analysis discloses that rotational shifts are feasible for transitions of even-to-even, odd-to-odd, odd-to-even, and even-to-odd nature. The molecular asymmetry of NCCP results in transitions that produce both even and odd Δj values, and its energy levels allow both odd and even j values. Both illustrations reveal the presence of shape and Feshbach resonances (FR) within energy limits up to E_t=300 cm^{-1}.[136] The FR are pronounced at $E_t\leq$130 cm^{-1} but wane as E_t rises, disappearing past 300 cm^{-1}. Quasi-bound states are detected as a consequence of the H_2 projectile being confined within a potential well. This confinement gives rise to FR, which persists until the H_2 possesses sufficient energy to escape the trap.

In contrast, shape resonances emerge as a result of tunneling effects that enable the H_2 projectile to pass through the centrifugal barrier. Moreover, as the j value increases, the cross-section trend generally ascends, consistent with typical rotational de-excitation behaviour. Figures 4.14(a) and 4.14(b) depict the rotational de-excitation cross-sections for both Δj=-1 and Δj=-2 transitions among the eight rotational levels. As j rises (from j=1 to 4 for Δj=-1 and 3 to 5 for Δj=-2), the cross-sections in both cases show an increase.[151] The information on the variation of the final state (j') concerning cross-sections is provided in Figure 4.15. These results demonstrate a notable inclination towards favoring even values of Δj compared to odd ones. The same propensity is observed in other phosphorus-containing systems such as PN-H_2[83] and HPO-He,[146] where Δj=-2 favours.

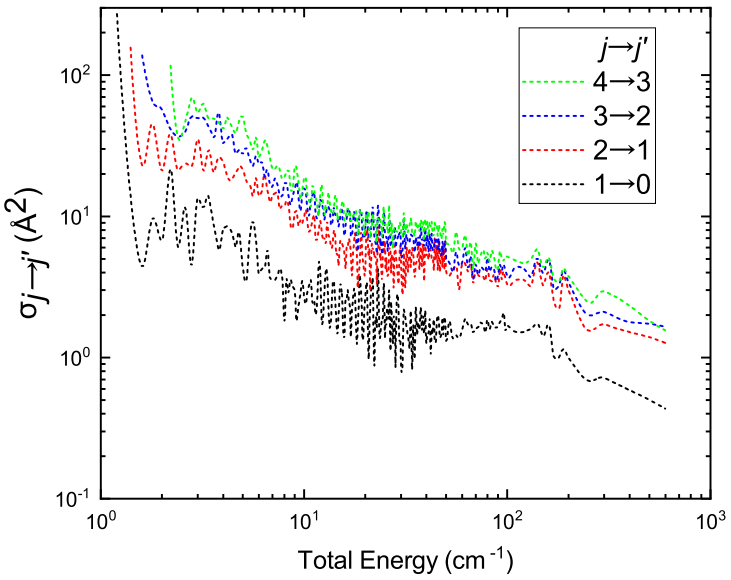

(a)

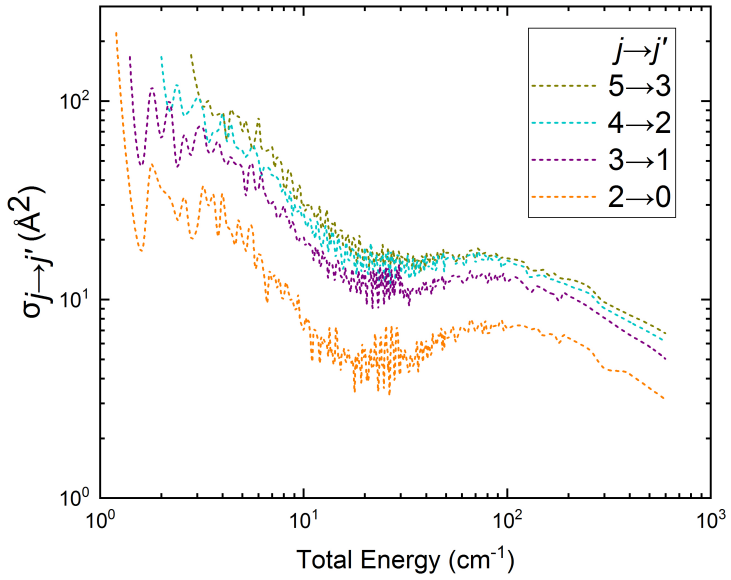

(b)

Figure 4.14: Plot of inelastic cross-sections of NCCP-H_2 with E_t where (a) Δj=-1 and (b) Δj=-2.

4.2.2.2 Rate Coefficients of NCCP-*para*-H_2 and Comparison with NCCP-He

The NCCP-*para*-H_2 interaction rate coefficients are calculated using equation 3.4 by thermally averaging the cross-sections obtained from CC calculations at various tem-

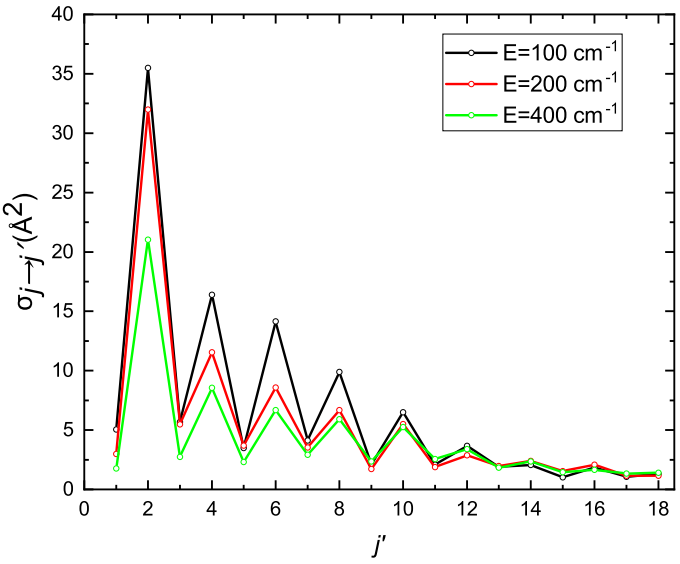

Figure 4.15: Propensities for the excitation of NCCP for E_t=100, 200 and 400 cm^{-1} from j=0 to j'.

peratures. The temperature range used for the measurements is 5-200 K. Figure 4.16 illustrates the rate coefficients of interest as a function of temperature. The ob-

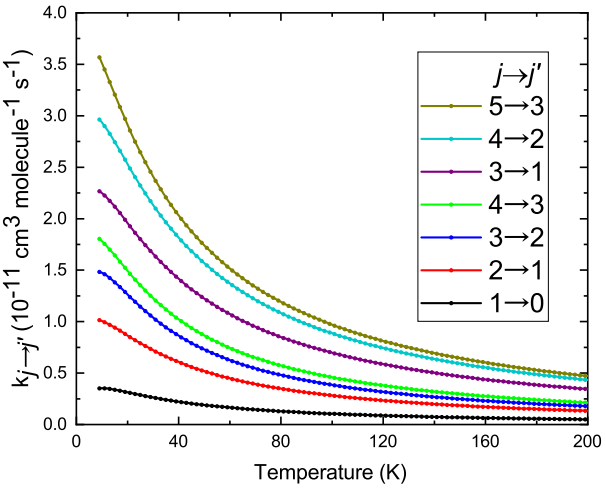

Figure 4.16: Rate coefficients of rotational de-excitation of NCCP-*para*-H_2 for selected transitions at 5-200 K.

served trends confirm the same propensity that favours even Δj=-2 transitions over Δj=-1 transitions. The obtained values of $k_{j\to j'}(T)$ for NCCP-*para*-H_2 are compared with previously determined rate coefficients of NCCP-He. The scaling factor (SF) for

NCCP can be determined using the following equation:

$$\mathrm{SF} = \frac{k_{H_2}}{k_{He}} = \sqrt{\frac{\mu_{\mathrm{NCCP-He}}}{\mu_{\mathrm{NCCP-H_2}}}} = \sqrt{\frac{3.7831}{1.9587}} = 1.38. \tag{4.8}$$

The above approximation suggests that the cross-sections involving *para*-H_2 (j_p=0) and He are the same and this scaling factor of 1.38 is only attributed to the reduced mass factor incorporated in equation 3.4, which determines the associated rate coefficients. Since a limited number of systems have been examined with both He and H_2, it's necessary to verify the accuracy of this approximation. Figure 4.17 provides a comparison of $k_{j\to j'}(T)$ data, comparing the results for NCCP-He with NCCP-H_2. This indicates that accurate collisional rate coefficients using helium collision can-

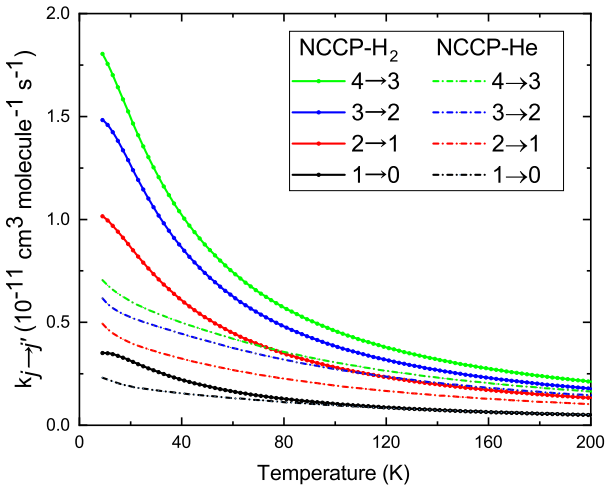

Figure 4.17: Rate coefficients of NCCP-*para*-H_2 and NCCP-He for Δj=-1 transitions.

not be achieved for *para*-H_2 interactions. The observed differences in the results are expected due to the difference in the well-depth of both NCCP-He and NCCP–H_2. NCCP-H_2 has three times deeper well than NCCP-He, resulting in a different range of resonances presented in Figure 4.14. The ratios of the $k_{j\to j'}(T)$, i.e., (NCCP-*para*-H_2(j_p=0)/NCCP-He), are tabulated in Table 4.4. Table 4.4 shows that the ratio is inconsistent and exhibits fluctuations at T=10 K and T=50 K.

At low-temperature values, the differences between the two sets of systems are more pronounced, and as the temperature rises further, the correspondence between the two sets of coefficients would likely become quite favorable. The outcomes align with the earlier research by Lique *et al.*[152] concerning collisions involving SO and H_2. In an attempt to examine these differences, we have also graphed the rate coefficients for various transitions at T=10 K and T=50 K as illustrated in Figure 4.18.

Table 4.4: Calculated values of $k_{j\to j'}(T)$ (in 10^{-11} cm^3 s^{-1} molecule^{-1}) for NCCP-*para*-H_2 and NCCP-He and their ratio.

j*→*j'	**T=10 K**			**T=50 K**		
	k_{H_2}	k_{He}	k_{H_2}/k_{He}	k_{H_2}	k_{He}	k_{H_2}/k_{He}
5→3	3.41	0.75	4.54	1.71	0.52	3.28
4→2	2.90	1.04	2.78	1.55	0.68	2.27
3→1	2.23	0.84	2.65	1.21	0.59	2.05
2→0	0.91	0.41	2.21	0.54	0.30	1.80
4→3	1.76	0.68	2.58	0.85	0.45	1.88
3→2	1.46	0.58	2.51	0.73	0.40	1.82
2→1	0.99	0.46	2.15	0.52	0.29	1.79
1→0	0.35	0.22	1.59	0.19	0.13	1.46

The estimated abundance of NCCP in molecular clouds could have been revised in light of these recently calculated rate coefficients. The bending frequency (ν_2)[71] for NCCP is found to be 206 cm^{-1}, but the infrared intensities of the vibrational transitions of linear NCCP are all very small, almost negligible due to very less polarity in the NCCP bonds. Strictly speaking, our dynamical calculations for rigid model NCCP are valid for energies lower than the lowest frequency (bending) of NCCP molecule, i.e., <206 cm^{-1}. Nonetheless, several benchmarks on molecules colliding with H_2 or He demonstrated that a complete consideration of vibrational degrees of freedom is not needed to account for the effect of vibration.[153–155] With the exception of a few cases, such as quasi floppy molecule which is linear (e.g., C_3),[154,156] where minor differences between rigid and nonrigid models were found, almost identical results were obtained without and with considering the vibrations. This should be the case for the NCCP molecule.

4.3 Summary

1. NCCP has been tentatively detected in the interstellar medium. Modeling of NCCP molecular emission from interstellar clouds requires the data of collisional rates. These useful data are obtained by generating PES and rotational cross-sections using highly accurate quantum methods. *Ab initio* PESs for collision between NCCP & He and NCCP & H_2 are computed using CCSD(T)-F12a/aug-cc-pVTZ.

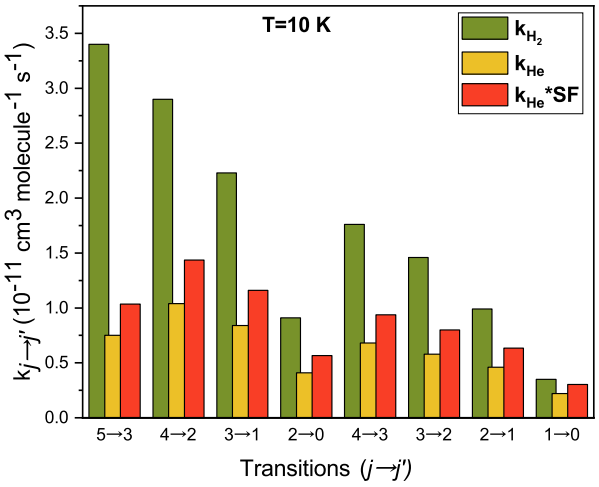

(a)

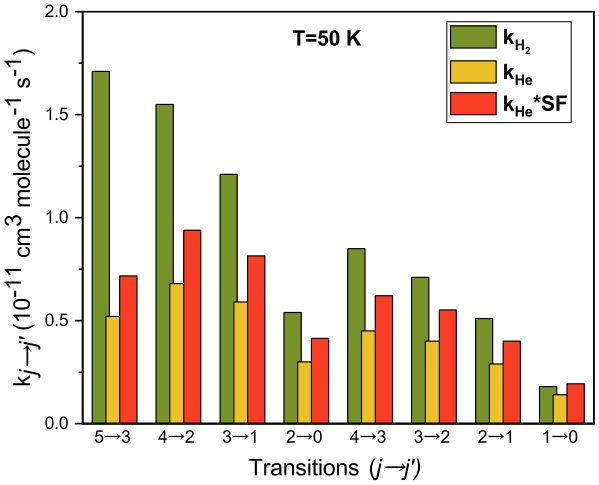

(b)

Figure 4.18: Comparison of rate coefficients of NCCP with *para*-H_2 and He along with the scaling factor (1.38) at T= 10 K and 50 K.

2. The 4DPES of NCCP-H_2 is averaged to 2DPES using three different angular orientations for the angles δ and θ_b at (0°,0°), (0°,90°), and (90°,90°), respectively. θ_a is varied from 0° to 180°. The averaged NCCP-H_2 PES has a global minimum of -125.40 cm^{-1}, which is deeper than the minimum energy of -46.40 cm^{-1} for the NCCP-He collision, and the well-depth is found at 110° for both systems. When expanded for multipole fitting, both systems show similar trends and shapes.

3. Rotational de-excitation cross-sections have been calculated for both systems

using the CC method. Furthermore, the spectrum of resonances in the NCCP-*para*-H_2 collision spans a wide range, extending to around 200 cm^{-1}. In contrast, the NCCP-He collision's range only encompassed approximately 50 cm^{-1}. In both cases, both even and odd Δj transitions are allowed. The effect of these differences is also clearly observed in rate coefficient plots.

4. Comparing the newly calculated $k_{j\to j'}(T)$ for NCCP-*para*-H_2 collisions with the existing NCCP-He rate coefficients reveals notable distinctions, particularly at lower temperatures. The rate coefficients for collisions with He appear to provide a plausible model for interactions with *para*-H_2 at moderately higher temperatures. It's crucial to highlight that the scaling factor cannot be deemed a dependable approach for replicating *para*-H_2 collisions. Analyzing the data, it becomes evident that the rate coefficients for NCCP-H_2 collisions are 1.5 to 4.5 times greater than those for NCCP-He collisions.

Chapter 5

Rotational Transitions of COH^+ and He: PES, Bound States and Pressure Broadening Cross-sections

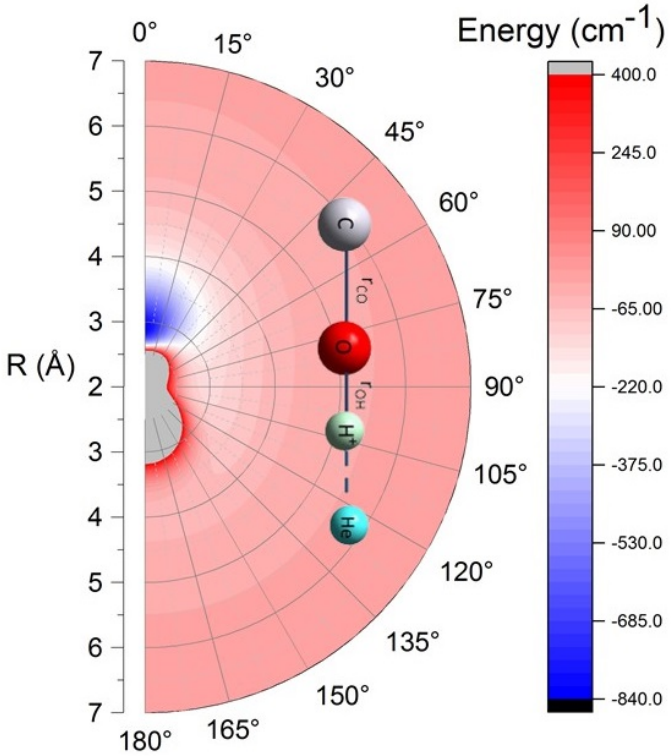

5.1 Potential Energy Surface of COH^+ in Collision with He

5.1.1 Computational Details and PES

The studied charged complex in this chapter consists of a linear COH^+ and a neutral spherical He atom. The linear COH^+ molecule is considered here as a rigid rotor in its ground vibrational state and is kept rigid with its bond distances r_{CO} = 1.158 Å and r_{OH} = 0.990 Å. Two Jacobi coordinates are described to characterize the COH^+-He system as shown in Figure 5.1.

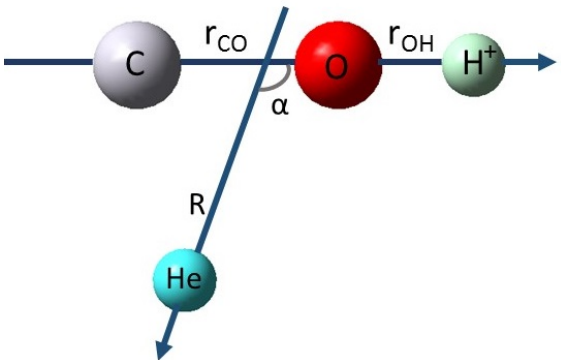

Figure 5.1: Jacobi parameters for the COH^+-He complex.

R stands for the distance between the two partners, i.e., the center of mass of COH^+ molecule and helium, r (r_{CO}, r_{OH}) for the intermolecular distance of COH^+, and α for the angle between the R vector and COH^+ axis. The ground state structure of the COH^+ molecule is linear concerning C-O and O-H distances according to the optimization of the COH^+ molecule. COH^+ is found to be in a $^1\Sigma^+$ electronic ground state with a closed shell. Other groups performed several calculations for the optimization of the COH^+ molecule using various levels of theory and Table 5.1 shows that the optimized bond distances calculated in this work match the reported results quite well. Our research starts with a thorough examination of the PES of the COH^+ and He complex. *Ab initio* calculations are performed using the MOLPRO package[114] with the method of coupled cluster involving single, double and perturbative triple excitations (CCSD(T))[160] and a basis set of augmented correlation consistent polarised valence quadruple zeta (aug-cc-pVQZ)[120] which has been observed to be the most

Table 5.1: Optimized bond distances of COH^+ molecule

	r_{CO} (Å)	r_{OH} (Å)
CCSD(T)/aug-cc-pVQZ[157]	1.158	0.990
CCSD(T)/cc-pVQZ[98]	1.157	0.990
CCSD(T)-F12a/aug-cc-pVTZ[158]	1.158	0.991
CCSD(T)-F12a/aug-cc-pVQZ[158]	1.158	0.990
Experimental values[159]	1.154	0.990
CCSD(T)/aug-cc-pVQZ (This work)	1.158	0.990

accurate to CCSD(T)/CBS (complete basis set) method as shown in Table 5.2.

Table 5.2: Well-depth values attained at different levels of theory (LoT).

LoT	α= 0°, R = 2.9 Å	α= 90°, R = 3.0 Å
CCSD(T)/aVTZ	811.34	120.76
CCSD(T)/aVQZ	836.55	131.39
CCSD(T)/CBS	**840.45**	**133.74**
CCSD(T)-F12a/aVTZ	848.97	139.70
CCSD(T)-F12b/aVQZ	849.18	140.96

R is varied from 1.5−30 Å using uniform grid with the stepsize of 0.1 Å. Additionally, R= 50.0 and 100.0 Å are calculated to check on the asymptotic behaviour. Uniform angular grid of 10° is chosen for α from 0° to 180°. The He atom approaching the H-end ($COH^+\cdots$He) is represented by $\alpha = 0°$ and He$\cdots COH^+$ shows an approach for $\alpha = 180°$. The three cuts of the PES for α= 0°, 90° and 180° are depicted in Figure 5.2. The variation of well-depth with respect to angle (α) is shown in Figure 5.3. The resulting COH^+-He contour and surface plots are presented in Figures 5.4 and 5.5, respectively, as a function of R and α.[161] From these figures, it is clear that this surface possesses a well-depth of -836.55 cm^{-1} at $R = 2.9$ Å, $\alpha = 0°$. The PES cuts at $\alpha = 90°$ and 180° have well-depth of -131.39 cm^{-1} and -50.29 cm^{-1}, respectively. Reported global minimum of COH^+-He[162] has a value of -853.49 cm^{-1}. This variation in well-depth is probably due to the difference in bond lengths of COH^+ and different methods used for calculations. Santander *et al.* used CCSD(T)-F12b/aug-cc-pVQZ level of theory. We have also compared our surface with its stable isomer HCO^+-He surface of Buffa and his coworkers[95] and recent work of Lique's group[100] on HCO^+-He complex. The well-depth of the former complex is -277.4 cm^{-1} at linearity towards

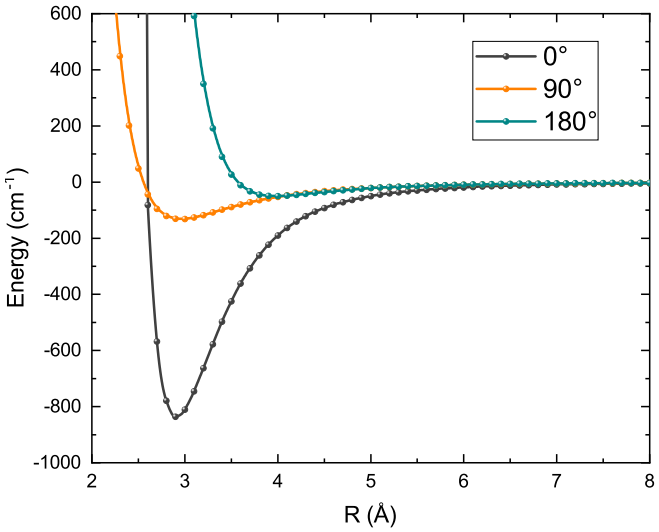

Figure 5.2: PES cuts for COH^+-He complex for selected geometries.

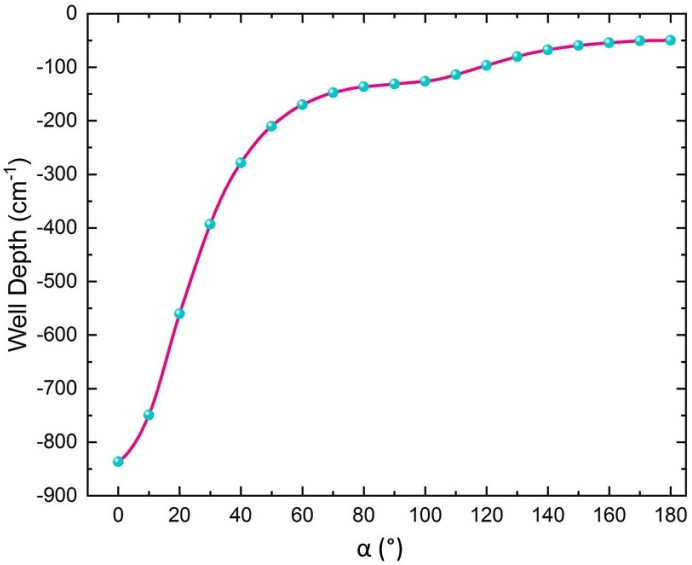

Figure 5.3: Variation of well-depth with orientation α for COH^+-He.

the H-end and that of the latter complex is -279.7 cm^{-1} at α=0° and R=3.6 Å. Since COH^+-He has three times larger well-depth than HCO^+-He, the scattering attributes will be expected to differ from the latter complex. In order to carry out the scattering study, the surface is expanded in the form of multipolar coefficients using equation 5.1:

$$V(R,\alpha) = \sum_{\lambda} V_{\lambda}(R) P_{\lambda}(cos\alpha), \tag{5.1}$$

where P_λ are the Legendre functions of order λ. Radial coefficients are calculated for

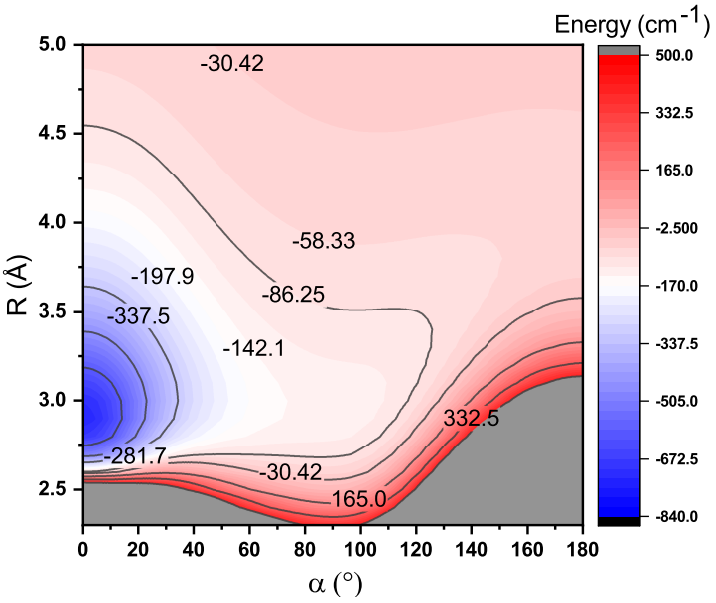

Figure 5.4: 2D Contour plot as a function of R and α for COH^+-He collision.

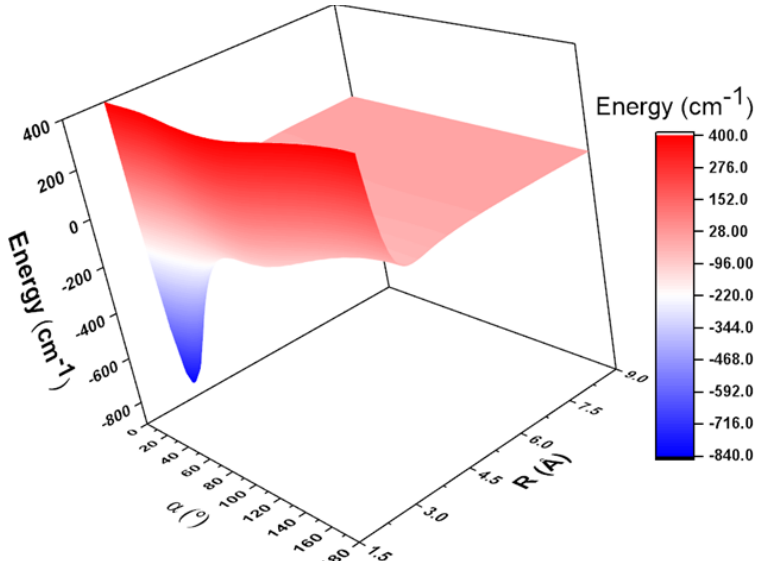

Figure 5.5: Potential energy surface as a function of R and α for COH^+-He collision.

$\lambda = 0-28$. The plot of λ corresponding to 0, 1, and 2 and V_λ varies as a function of R is shown in Figure 5.6. Due to the unsymmetric nature of COH^+, both odd and even λ's exist for this charged complex. $\lambda = 1$ and 3 strongly outweigh the $\lambda = 0$ and 2 and its potential well exists in the attractive region. The dominance of such a term may have a consequence on the behaviour of the dynamic results. The average difference between the analytical fit and *ab initio* calculations is less than 0.3% over the entire grid.

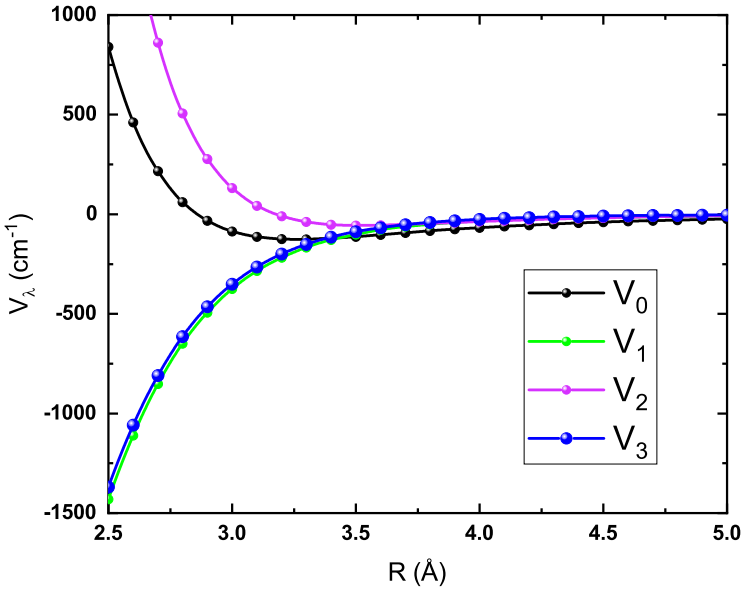

Figure 5.6: Radial coefficients as a function of R.

5.2 Bound-state Calculations and Pressure Broadening Cross-sections

Bound state calculations serve as a crucial accuracy assessment for potential energy surfaces. Bound-state spectroscopy is used to determine the PES-shape-related information. We have calculated the bound state energies despite this system's lack of experimental data, which will necessitate further experimental testing. Furthermore, the configuration of bound states significantly influences the emergence of scattering Feshbach resonances. We have used the BOUND[163,164] program to compute the bound state energies for this complex. The values of reduced mass (μ), rotational and distortion constants are given in Table 5.3. We have carried out the calculations

Table 5.3: MOLSCAT parameters for the scattering calculations

$B_e = 1.492$ cm^{-1}	$D_e = 3.8 \times 10^{-6}$ cm^{-1}
$j_{max} = 30, 35, 40, 45$	$\mu = 3.51719$ a.m.u.
$R_{min} = 1.5$ Å	$R_{max} = 50$ Å
OTOL $= 0.001$ Å^2	$DTOL = 0.01$ Å^2

for the first 30 rotational levels using a log-derivative propagator in the energy range from 0 to -840 cm^{-1}. Table 5.4 lists the difference in computed energies between the two states of COH$^+$−He and its isomeric pair HCO$^+$−He[100] that are radiatively

connected. This study calculates the rotational inelastic de-excitation cross-sections

Table 5.4: Computed rotational transitions ($j \rightarrow j'$) of COH^+-He complex. All quantities are given in MHz.

j	j'	COH^+-He	HCO^+-He[100]
0	1	24685.72	17381.45
1	2	49369.90	34755.08
2	3	74050.85	52104.04
3	4	98726.83	69454.38
4	5	123396.09	86754.36
5	6	148056.93	104023.15
6	7	172707.89	121235.50
7	8	197347.44	138402.60
8	9	221975.15	155532.41
9	10	246583.58	172563.47
10	11	271176.19	189540.72
11	12	295749.22	206444.76
12	13	320300.42	223231.25

as a function of total energy using the fitted COH^+-He PES. The time-independent equations of the CC method were introduced by Arthurs and his group[122] in the field of molecular collisions. In this CC approach, the rotational Hamiltonian is given as:

$$H_{rot} = B_e \boldsymbol{J}^2 - D_e \boldsymbol{J}^4. \tag{5.2}$$

The Alexander-Manolopoulos Airy (AIRY) propagator is adopted to solve the CC equations[135] and is implemented in the molecular scattering code MOLSCAT[134]. The important parameters required to perform the MOLSCAT calculations are given in Table 5.3. The limits of integration of MOLSCAT calculations are set to R_{min}= 1.5 Å and R_{max}= 50 Å. The total energy and the STEPS parameter are inversely proportional to the integration step. The STEPS parameter is therefore set to 20 for total energy lower than 110 cm^{-1} and 10 for higher than & equal to 110 cm^{-1}. The value of rotational (B_e) and distortion (D_e) constants used[98] are provided in Table 5.3. The non-reactive scattering computations between COH^+ and He are done for total energies ranging from 0.5 to 250 cm^{-1} considering the bending frequency (249 cm^{-1})[165] of COH^+ molecule. The energy grid between consecutive calculations is spanned as: 0.1 for 0.5−110 cm^{-1}, 1 cm^{-1} for 110−150 cm^{-1}, 5 cm^{-1} for 150−200

cm^{-1}, 10 cm^{-1} for 200−250 cm^{-1}. The rotational basis denoted by j_{max} is fixed to 30 for total energy (E_t) up to 100 cm^{-1} and successively increased to j_{max} = 45 up to 250 cm^{-1} energy. Rotational transitions from an initial state (j) to a final state (j') are characterized and cross-sections are computed using the equation 3.3. The centrifugal distortion (D_e) is included while computing the rotational levels of COH^+ under the rigid rotor assumption. The formula for rotational energy, E_j, is $E_j = B_e j(j+1) - D_e j^2(j+1)^2$. It is observed that the cross-section calculations indicate the existence of (shape and Feshbach) resonances due to the small energy step that is used here, and the complex comprises of both even and odd j rotational transitions. The perturber (helium) is stuck in the potential well, resulting in quasi-bound states of the COH^+−He system, which causes the Feshbach resonances and shape resonances to occur from tunneling resulting from the centrifugal energy barrier. The rotational cross-sections of COH^+-He collisions are shown in Figure 5.7 with their dependency on total energy (E_t) for the Δj=-1 and various $j \rightarrow 0$ transitions. Cross-sections for de-

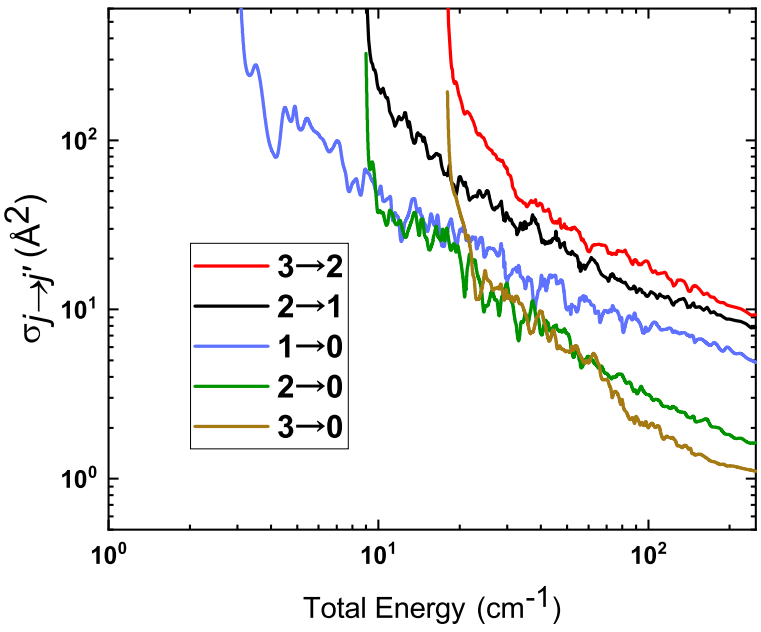

Figure 5.7: Dependence of cross-sections ($\sigma_{j \rightarrow j'}$) on the total energy ($E_t$) for $j \rightarrow j$' transitions for COH^+-He complex.

excitations often decrease as total energy rises.[166] Several resonances can be noticed for total energies less than 110 cm^{-1}. These resonances disappear at higher energies. Similar trend and behaviour of plots are also noticed in recent work and HCO^+-He system.[100] Additionally, Figure 5.7 illustrates how the cross-sections for Δj=-1 transitions increase as the value of j increases and as Δj rises, the cross-sections ($\sigma_{j \rightarrow j'}$) for

$j \rightarrow j'=0$ transitions become smaller. Cross-sections for $1 \rightarrow 0$ transitions predominate over $2 \rightarrow 0$ and $3 \rightarrow 0$. Compared to recent data of cross-sections of COH^+-He,[162] the results are approximately the same. The small differences observed may be because of differences in reported well-depth values or B_e value that they took into consideration.

Pressure-broadening calculations of the rotational spectra of molecular ions at low temperatures are of great interest due to their close relation with rotationally inelastic cross-sections. While state-to-state cross-sections are responsible for only inelastic collisions, pressure broadening depends on both elastic ($\Delta j=0$) and inelastic collisions ($\Delta j \neq 0$). Such a study was carried out for CO colliding with helium by Palma, *et al.* (1986)[167] Yang *et al.*[168] and by Ball & De Lucia (1998).[169] We have calculated the broadening cross-sections by obtaining the S-matrices from the scattering calculations.[100,134,170] The calculations of these cross-sections involve both upper and lower examined states having the same kinetic energy but different values of total energies. Pressure broadening cross-section calculations result in two parts: the real part describes the pressure broadening coefficient (γ), and the imaginary part describes the pressure shift coefficient (s) for a given transition. Figures 5.8(a) and (b) illustrate the trend of real and imaginary cross-sections, respectively, over the kinetic energy showing the resonances in the low energy range and that is more pronounced for the lowest rotational transition ($j=0 \rightarrow 1$).[161] These cross-sections must be thermally averaged in order to be compared to the experiment, where collisions usually take place at a variety of collision (kinetic) energy following the Maxwell-Boltzmann distribution, and that can be done using equation 5.3:[171]

$$\sigma(T) = (k_B T)^{-2} \int E_c \exp\left(\frac{-E_c}{k_B T}\right) \sigma(E_c) dE_c, \tag{5.3}$$

where T denotes the temperature in kelvin and is set to 88 K for the sake of comparison with its isomer HCO^+.[172] The values of integrated real and imaginary cross-sections at 88 K are presented in Table 5.5. We have calculated the broadening and state-to-state cross-sections and compared their peaks for $0 \rightarrow 1$ transition and found some extra peaks in pressure broadening cross-sections' curve corresponding to elastic collisions that are absent in case of inelastic collisions as shown in Figure 5.9.

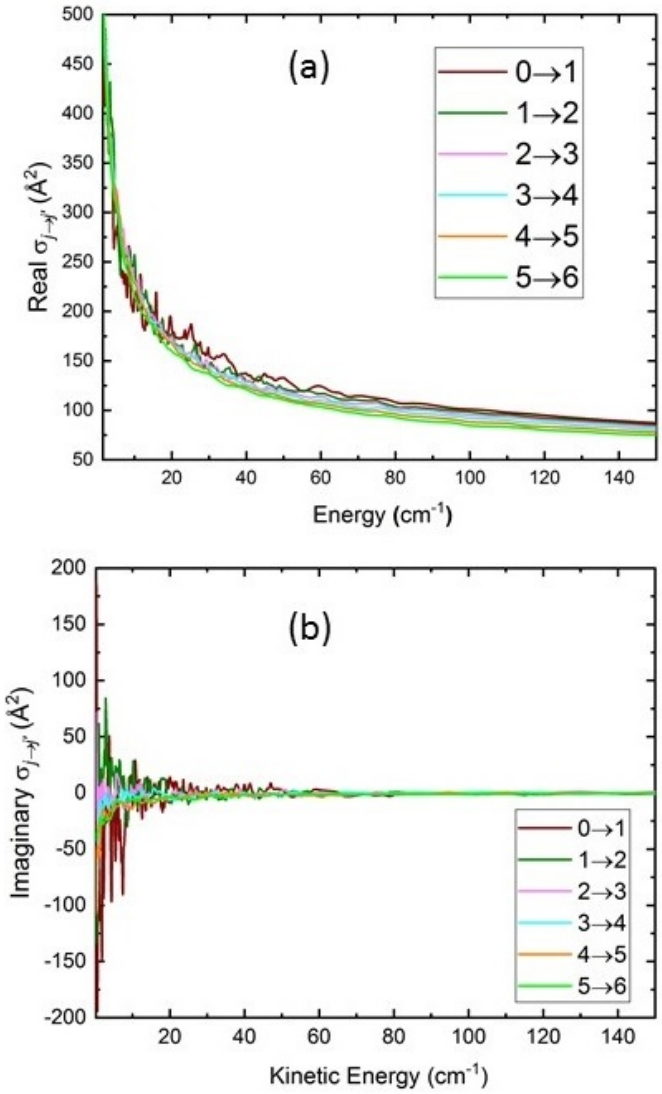

Figure 5.8: Variation of (a) real and (b) imaginary cross-sections ($\sigma_{j\to j'}$) with energy (E_t) for Δj=1 transitions for COH^+-He complex.

5.2.1 Pressure Broadening and Shift Coefficients

We have reported the results of pressure broadening (PB) coefficients of COH^+ in He gas at a temperature of 88 K in this paper. PB coefficients define the half-width-at-half-maximum (HWHM) of the spectroscopic line with a Lorentzian shape. Its expression is normalized per helium atmosphere as given in the equation: 5.4[173,174]

$$\gamma - is = nv\sigma(T) = \frac{56.6915}{\sqrt{\mu T}}\sigma(T), \tag{5.4}$$

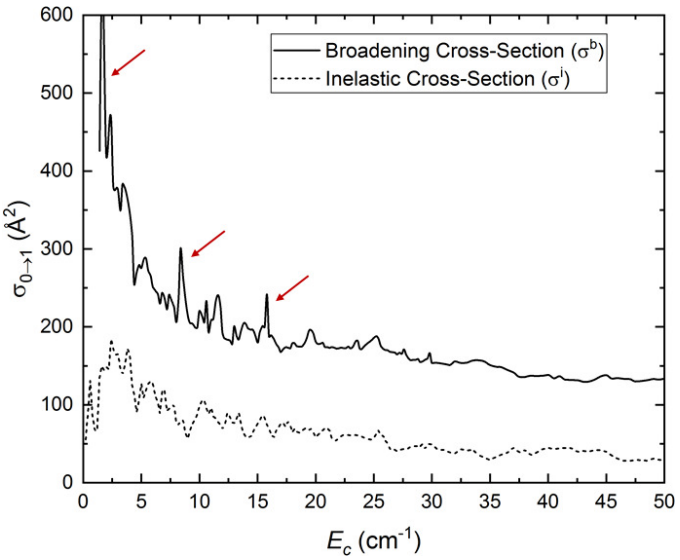

Figure 5.9: Comparison between pressure broadening cross-section (solid) and inelastic cross-section (dotted) for j=0→1 transition. Red arrows show the peaks for pressure broadening that are absent for inelastic collisions.

Table 5.5: Computed real and imaginary broadening cross-section for the COH^+−He at 88 K obtained by integration over the energy.

$j \rightarrow j'$	Real σ(Å^2)	Imaginary σ(Å^2)
0→1	112.099	0.602
1→2	109.348	0.197
2→3	108.341	1.093
3→4	106.135	1.268
4→5	104.223	2.474
5→6	101.040	2.761

where γ and s are given in cm^{-3} atm^{-1}, v=$(8k_BT/\pi\mu)^{1/2}$ is average velocity, $\sigma(T)$ is the thermally averaged broadening cross-section in Å^2, n denotes the number density of the perturbing gas, μ, reduced mass in a.m.u. and T is temperature at 88 K. The values of γ and s are calculated with the help of thermal averaged broadening cross-sections, i.e., $\sigma(T)$. The product of v and $\sigma(T)$, averaged over a Maxwell-Boltzmann distribution is known as the rate coefficient. Results of γ and s for this complex and HCO^+−He are given in Table 5.6. From these results, it is inferred that the results

Table 5.6: Computed values of pressure broadening (γ) and shift coefficients (s) for COH^+-He and comparison with the reported data of its stable isomer.

$j \rightarrow j'$	**This work**		**HCO^+–He**[100]	
	γ (MHz/Torr)	s (MHz/Torr)	γ (MHz/Torr)	s (MHz/Torr)
0→1	14.330	0.037	14.37	0.172
1→2	13.978	0.012	13.58	0.153
2→3	13.849	0.068	13.23	0.134
3→4	13.567	0.079	12.85	0.206
4→5	13.323	0.015	12.52	0.302
5→6	12.916	0.017	12.26	0.343

of COH^+-He are in the same order with the HCO^+-He[100] in magnitude. The minor differences are being observed due to the difference in value of the well-depth of the isomeric system (HCO^+-He=-279.7 cm^{-1} and COH^+-He=-836.5 cm^{-1}).

5.3 Rate Coefficients

By integrating the cross-sections, the collisional rate coefficients (equation 3.4) from the state-to-state cross-sections at temperature T. Figure 5.10 shows the plots of rotational rate coefficients over a range of 5−60 K temperatures.

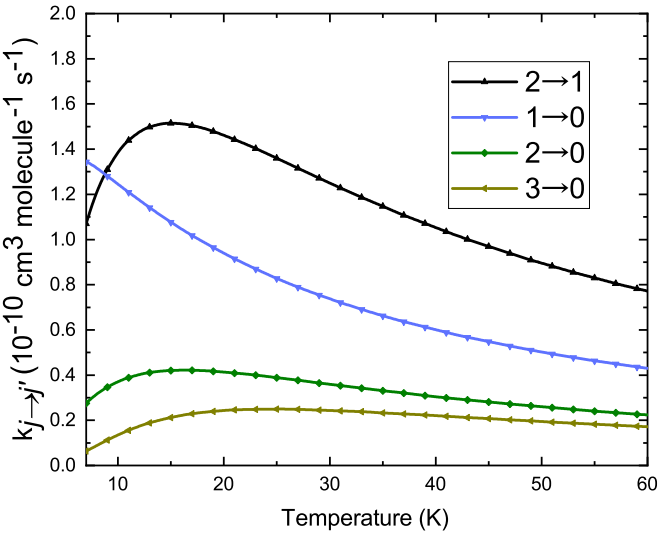

Figure 5.10: Rates with respect to change in temperature for $j \rightarrow j$' transitions for COH^+-He complex.

Looking at the propensity, we observe that Δj=-1 are favoured over other Δj

(Δj=-2 and -3) transitions. For Δj=-1, 2→1 transition has maximum rate as shown in Figure 5.10 and it decreases with decreasing rotational level j. The Langevin theory's prediction for ion-neutral interactions is reflected at higher temperatures, where all rate coefficients become almost temperature-independent. The comparison of present results with that of HCO^+-He[95,100] shows that both isomers have comparable rate ($\sim 10^{-10}$ cm^3 molecule^{-1} s^{-1}) and similar behaviour. We have also compared our rate coefficients data with Santander *et al.*[162] in the Table 5.7 (right panel), and our data is found to be in the same order with very negligible differences. The small differences

Table 5.7: Comparison of rate coefficients (in 10^{-10} cm^3 molecule^{-1} s^{-1}) data with the reported work of Santander *et al.*

Temperature (K)	**This work**		**Reported Data**[162]	
	2→1	1→0	2→1	1→0
10	1.32	1.28	1.60	0.95
20	1.47	0.93	1.42	0.84
30	1.28	0.73	1.32	0.80

are suspected to be due to different well-depth values and different procedures of analytical fitting.

5.4 Summary

1. PES of protonated carbon monoxide molecule with He is computed at CCSD(T)/aug-cc-pVQZ. We have reported the well-depth of the surface as -836.55 cm^{-1} at α=0° and R = 2.9 Å. In contrast, Santander *et al.* presented a PES with a well-depth of -853.49 cm^{-1} at the same R value. This disparity in the well-depth values can be attributed to the variations in the bond lengths of COH^+ and the use of different [CCSD(T)-F12b/aug-cc-pVQZ] calculation methods. Further, the expanded potential energy surface is used to perform quantum dynamical studies.

2. The rotational frequencies of the bound states with j in the range 0-19 have been computed for this system. CC calculations are performed for calculating the broadening cross-sections for kinetic energies up to 150 cm^{-1}. In addition, the comparison between the broadening and the inelastic cross-sections predicts that some extra peaks are available in the former that are absent in the case of inelastic cross-sections. The complex comprises of both even and odd j rotational transitions.

3. The state-to-state rate coefficients have been calculated for the COH^+-He complex and the data has been compared with the reported COH^+-He work at three different temperatures. The obtained rate coefficients are generally consistent with the previously reported data for COH^+-He, with minor variations primarily attributed to differences in the potential energy surface well-depths for both systems. We expect that this work will encourage more experiments on COH^+ collision with He and the data presented here will be very beneficial for astrophysical observations in ISM as well as for experiments.

Chapter 6

Rotational Quenching of C_2 with ^{3}He and ^{4}He Collisions at Ultracold Temperatures

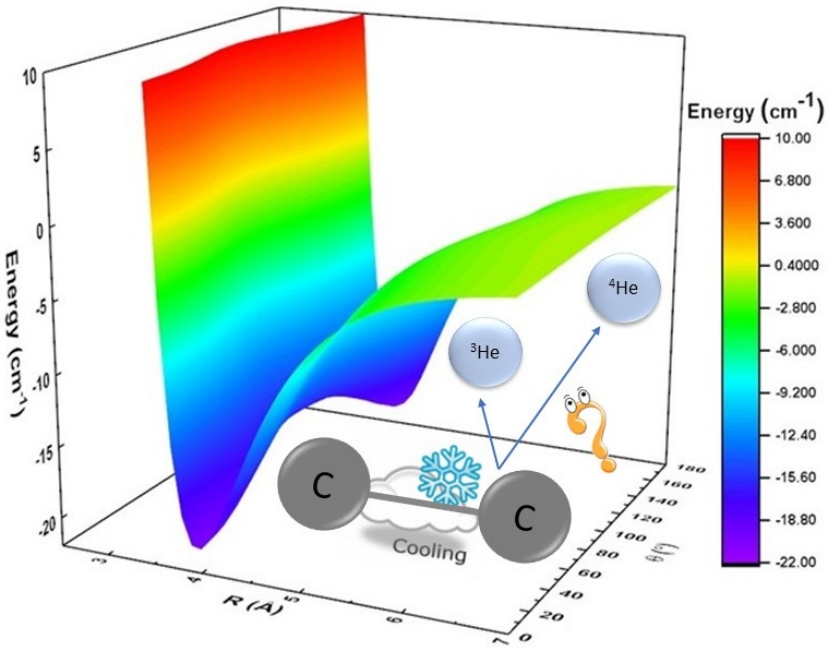

Rotational quenching of C_2 with ^{3}He and ^{4}He

6.1 Introduction to Ultracold Molecules and Ultracold Chemistry

Over the last few years, preparing the reactants and controlling products with quantum state precision has become the ultimate goal. This promise is fulfilled by ultracold chemistry, a novel and rapidly expanding area in which reactants are created in a single quantum state.[175–180] The term ultracold in atomic and molecular physics refers to collisions that take place below 1 mK temperature. Applications for ultracold atoms and molecules include quantum simulation of spin-lattice models, testing fundamental symmetries of nature, molecular spectroscopy, and chemically controlled reactions.[7,175]

Experiments for cooling and trapping molecules have significantly progressed over the last decade. A wide variety of direct and indirect methods came into consideration to generate ultracold molecules.[181–183] Helium buffer gas cooling,[184–186] sympathetic cooling[187] and Stark Deceleration[188,189] techniques which are the direct methods involve removing kinetic energy from pre-existing molecules and indirect methods, which include photoassociation[190,191] and magnetoassociation[192–194] rely on fusing ultracold atoms that have been previously cooled. Buffer gas cooling is a relatively effective and good approach for trapping and cooling molecules and here, excess energy is transferred to the helium gas. Meijer and co-workers demonstrated the approach of Stark Deceleration by cooling ammonia molecules to about 350 mK[195] and metastable CO molecules to 4 mK temperature.[196]

The performance of buffer gas and sympathetic cooling is mainly determined by the values of the scattering cross-section. Internal energy transfer in cold diatomic molecules colliding with cold ^{3}He and ^{4}He buffer gases are of significant interest. Several investigations have already been done on ro-vibrational energy transfer collisions.[125,129,197–199] To our knowledge, diatomic molecules such as Nitrogen (N_2),[200–202] oxygen (O_2),[203] carbon monosulphide (CS)[198] and carbon monoxide (CO)[204–206] have been studied having collision with ^{3,4}He and their collisions are also pretty crucial with ^{4}He in astrophysics. Also, the ultracold collisional study of O_2 and N_2 considering the isotopic effect of He was subjected to numerous experimental and theoretical research. The cross-sections of these systems follow the Wigner threshold law below a

threshold kinetic energy. The controlling molecular interactions in the same manner as atomic interactions are of great importance.[207]

In this work, we concentrate on the rotational quenching of C_2 with ^{3}He and ^{4}He. This system was chosen because of the recent chemical synthesis of diatomic C_2.[208] Also, a theoretical study of C_2 has indicated that C_2 has a quadruple bond with a singlet biradical character in the ground state.[209] Since C_2 has no permanent dipole moment, this molecule cannot be cooled with the technique of Stark Deceleration,[188,189] instead, we will need to use helium buffer gas cooling.[210]

6.2 Potential Energy Surface of C_2 with He

6.2.1 PES and Analytical fit

The accurate description of the van der Waals interaction between the C_2 molecule and He gas needs the use of a higher-order electron correlation method and basis set. The geometry optimization of C_2 molecule is performed in the MOLPRO package using the CCSD(T)/aug-cc-pVQZ level of theory and further, we have performed explicitly coupled CCSD(T)-F12 computations to investigate its accuracy. Among the different approximations of CCSD(T)-F12 correlation energies, the CCSD(T)-F12b[117,118] approximation with scaled triples has been shown to correspond well with CCSD(T) having a large-basis. The *ab initio* PES computed for this work describes the interactions between a linear entity C_2 and an atomic helium keeping the C_2 fixed at equilibrium distance, r=1.246 Å. We have computed a two-dimensional PES for C_2-

Figure 6.1: Optimized C_2 Molecule

He using the CCSD(T)-F12b method associating with aug-cc-pVQZ. We find a weak van der Waals complex that is most conveniently described using the three Jacobi coordinates r, R and θ as defined in Figure 6.2. Here R presents the internuclear separation between helium and the C_2 molecule's center of mass. θ is the angle between R and molecule bond vector, r. Najar et al. reported the ground and the first excited state PES for C_2-He using MRCI+Q and concluded that there exists no conical

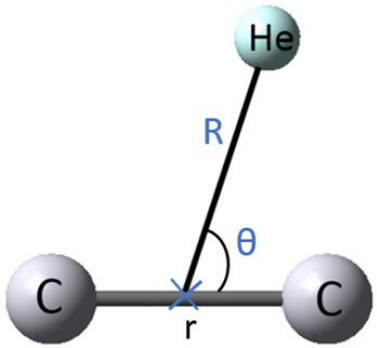

Figure 6.2: Jacobi coordinates of C_2-He system

intersection between the two electronic states.[138] To ensure the size consistency, basis set superposition errors are computed using the method of counterpoise:[121]

$$V(R,\theta) = E_{C_2-He}(R,\theta) - E_{C_2}(r,\infty) - E_{He}(\infty). \tag{6.1}$$

Separation between the C_2 and He is varied from 2.5 to 25 Å with the step size of 0.1 Å and θ is varied from 0° to 180° degrees. The potential energy curves for this van der Waals complex are shown in Figure 6.3. This weak van der Waals He-C_2 system's

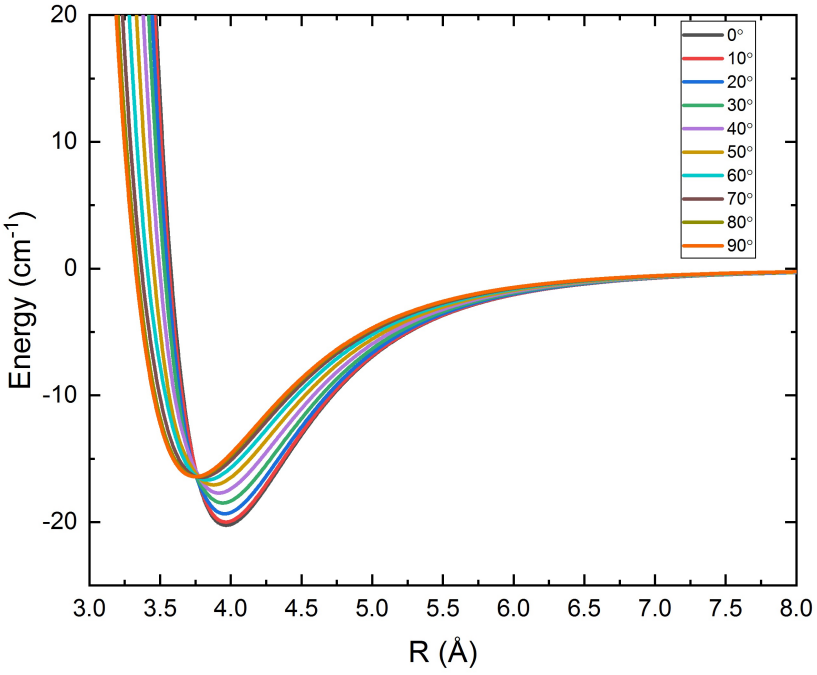

Figure 6.3: Potential energy curves for C_2-He.

well-depth at its global minimum is -20.3 cm^{-1} at R=4.0 Å and θ=0° and r=1.246 Å as shown in Figures 6.4 and 6.5. These values are in good accordance with those of Najar et al. that is 19.6 cm^{-1} at R= 3.95 and θ=0°.[138]

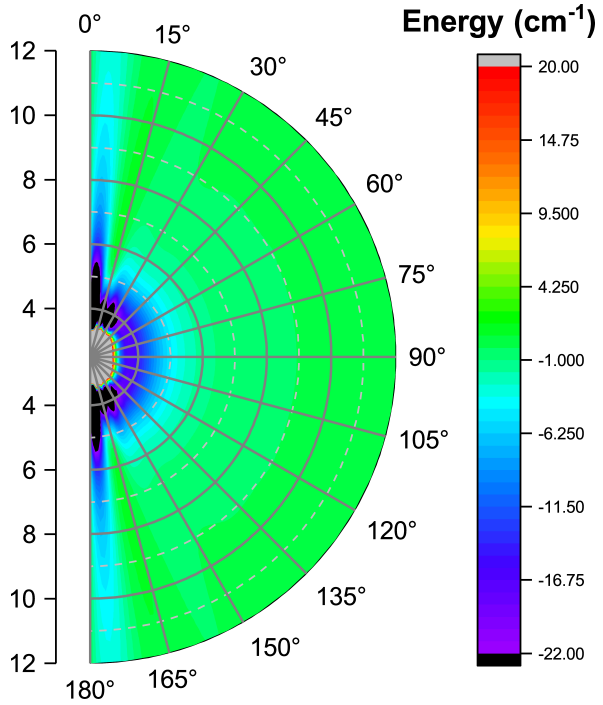

Figure 6.4: Polar contour plot of $C_2(X^1\Sigma_g^+)$-He(^{1}S) system at r=1.246 Å.

The PES is interpolated analytically in terms of multipolar coefficients for carrying out the dynamical calculations according to

$$V(R,\theta) = \sum_{\lambda} V_\lambda(R) P_\lambda(cos\theta), \tag{6.2}$$

where P_λ(x) is the Legendre polynomial of order λ and V_λ(R) are radial strengths. We have included the λ's up to λ_{max}=18. Due to the symmetric nature of C_2, only even terms contribute. The radial coefficients V_λ for λ=0, 2 and 4 are plotted in Figure 6.6. The λ=0 strength has a minimum energy at around -19 cm^{-1}.

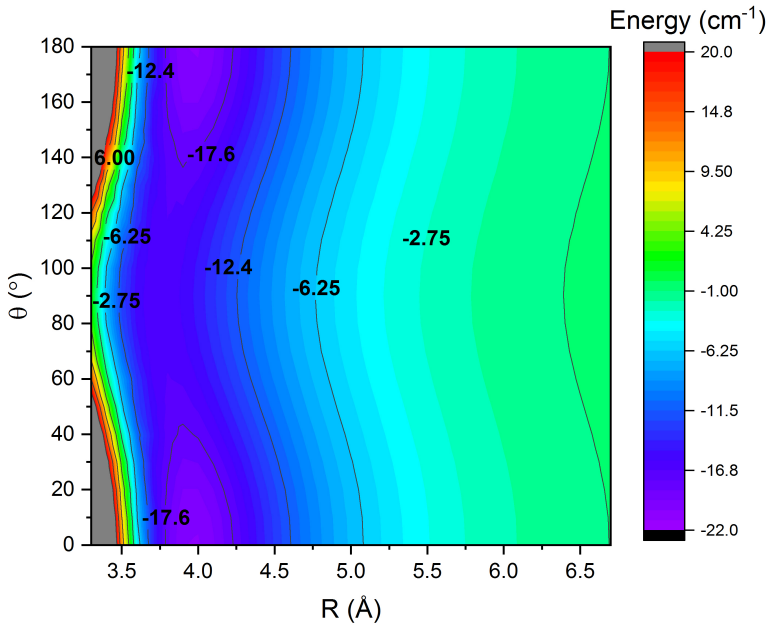

Figure 6.5: 2D contour plot of C_2-He.

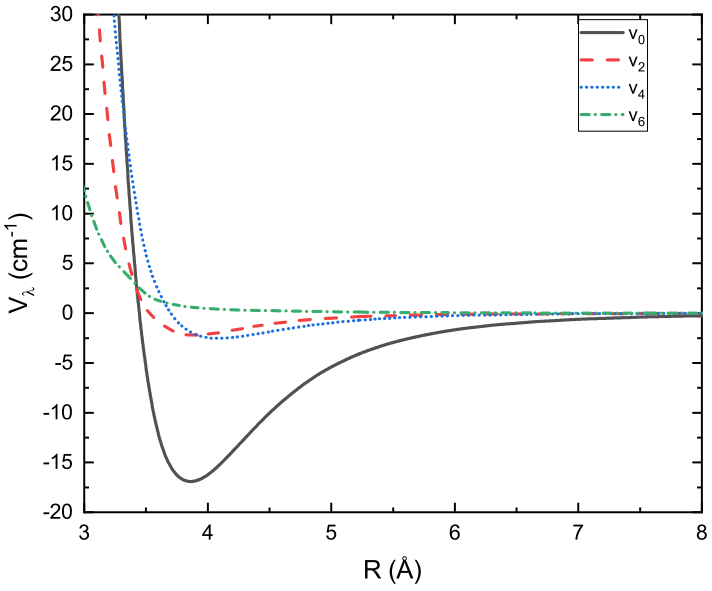

Figure 6.6: Computed radial coefficients (λ=0-6) with respect to R associated with C_2 ($X^1\Sigma_g^+$)+ He (^{1}S) 2D-PES.

6.3 Rotational Quenching of C_2 with ^{3}He-C_2 and ^{4}He-C_2

6.3.1 Computational Details

The MOLSCAT[134] code is used to calculate the cross-sections using the CC method. We have used CC wave function expansion in terms of products of the diatoms rotational eigenfunctions and spherical harmonics for the rotation of He around the center of mass of C_2.[122] We have labeled the diatomic states by angular momentum j and the C_2-He rotational states by orbital angular momentum or partial wave l. Here, we have used the AIRY propagator[135] for integrating coupled-channels equations. State-to-state cross-sections are computed with the help of scattering matrix $S^J_{jj'll'}$ and

$$\sigma_{j\to j'}(E_k) = \frac{\pi}{k_j^2(2j+1)} \sum_{J=0} \sum_{l=|J-j|}^{J+j} \sum_{l'=|J-j'|}^{J+j'} \times |\delta_{jj'}\delta_{ll'} - S^J_{jj'll'}(E_k)|^2 \times (2J+1). \quad (6.3)$$

J is the conserved total angular momentum. The prime quantities j' and l' describe the final states after the quenching. $k_j{=}\sqrt{2\mu E_k}/\hbar$ represents the wave vector for C_2 rotational channel j with kinetic energy E_k and reduced mass μ. The total de-excitation (quenching) cross-section from a initial j state is:

$$\sigma_j^{tot} = \sum_{j'} \sigma_{j\to j'}. \quad (6.4)$$

The scattering cross-section may represent the scattering length in the limit of zero kinetic (collision) energy. When scattering occurs in a single channel, the scattering length is real, but when two or more channels remain open in the case of inelastic scattering, the scattering length becomes imaginary. Complex scattering length, a can be denoted as (α -iβ), where β and α represent the imaginary and real parts of scattering length, a. In the limit of zero energy, the elastic cross-section is

$\sigma_{j\to j}(E_k{\to}\ 0){=}\ 4\pi(\alpha_j^2{+}\beta_j^2)$, where imaginary part is:

$$\beta_j = \lim_{k_j\to 0} \frac{k_j\sigma_j^{tot}(E)}{4\pi}. \quad (6.5)$$

The quenching rate coefficient comes finite and is given by $r_j(T\to 0) = 4\pi\beta_j\hbar/\mu$.[211] The quenching rate coefficient, $r_{j\to j'}(T)$ at temperature T from j to j' is:

$$r_{j\to j'}(T) \quad = \quad \sqrt{\frac{8k_BT}{\pi\mu}}\,(k_BT)^{-2}\int_0^\infty \sigma_{j\to j'}(E_k) \quad \times \quad E_k \exp\left(\frac{-E_k}{k_BT}\right) dE_k. \quad (6.6)$$

Finally, we compute the predissociation lifetime from the imaginary part β_j using the expression:[211]

$$\tau_j = \frac{\mu|a|^4}{2\hbar\alpha_j\beta_j}. \quad (6.7)$$

6.3.2 Close Coupling Calculations at Low and Ultralow Energies

Cross-section calculations are performed in the energy domain of 10^{-6} cm^{-1}-1000 cm^{-1} for both isotopes of helium (^{4}He and ^{3}He). The input parameters used in the MOLSCAT calculations are rotational constant, B_e= 1.8201 cm^{-1} and reduced mass, μ=2.6795 a.m.u. (^{3}He-C_2) and μ=3.4309 a.m.u. (^{4}He-C_2). The step size in energy is 0.1 cm^{-1} for energy less than 20 cm^{-1}, 0.5 cm^{-1} from 20-50 cm^{-1}, 1 cm^{-1} from 50-100 cm^{-1}, 10 cm^{-1} from 100-200 cm^{-1} and 100 cm^{-1} from 200-1000 cm^{-1}. We obtain state-to-state cross-sections for j=8 to j'=0, 2, 4 and 6 as shown in Figure 6.7.

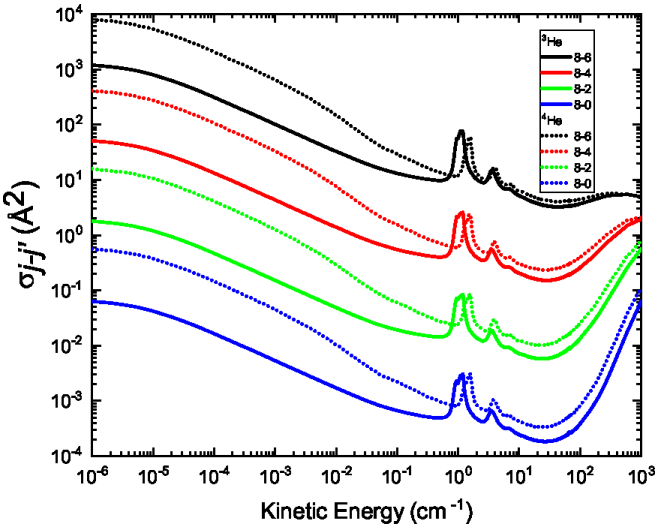

Figure 6.7: Integral rotational cross-sections as functions of kinetic energy for C_2 colliding with ^{3}He (solid curves) and ^{4}He (dotted curves) from j=8 to j'=6,4,2 and 0.

Only even rotational transitions are present due to the symmetric nature of C_2 and nuclear spin statistics. The C_2 + ^{4}He collision leads to approximately one order of magnitude larger cross-sections than the lighter ^{3}He case. This similar behaviour of difference in the values of the cross-section between ^{3}He and ^{4}He is shown by some diatomic (N_2-He,[212] MgH-He,[213] CS-He[198]) and symmetric (NCCN-He[129]) systems. Among all the results shown in Figure 6.7, the transition from j=8 to j'=6 has the largest cross-sections and transition Δ=-2 dominates. Two isotopes of helium quenched from j=2 to j'=0 vary a little after 10^{-1} cm^{-1} and ^{4}He has more value of cross-sections initially, as presented in Figure 6.8. Figure 6.8 follows the same trend

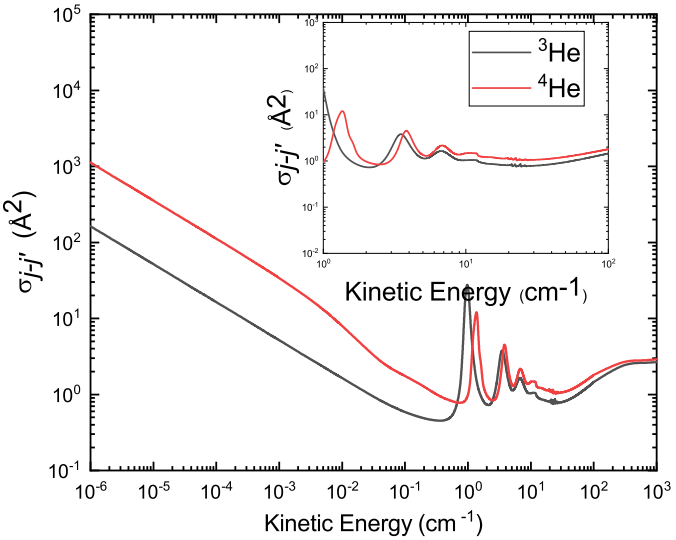

Figure 6.8: Integral rotational cross-sections as functions of kinetic energy for C_2 colliding with ^{3}He (black curve) and ^{4}He (red curve) from j=2 to j'=0.

for cross-sections in case of ^{4}He as that of Najar et al.[138] for Δj=$\pm$2. Both the plots show resonances below 100 cm^{-1} and above 100 cm^{-1}, the value of cross-sections keeps on increasing. In Figure 6.8, it is inferred that the value of cross-sections decreases with the increase in kinetic energy below 10^{-1} cm^{-1} following the Wigner's threshold law at ultralow kinetic energies. The cross-section increases with kinetic energies above 100 cm^{-1}. The cross-sections for two isotopic forms of He lie close to each other and the resonances in the plots are caused by the formation of van der Waals complex in the energy scale of 1 cm^{-1} to 40 cm^{-1} for the transition occurring from j=2 to j'=0.

Further, we have studied the scattering length of both the isotopes of He colliding with C_2. The values of β_j for ^{3}He and ^{4}He are 0.0069 Å and 0.637 Å, respectively. The total cross-sections for rotational transitions of C_2 with ^{3}He and ^{4}He as a function of kinetic energy for j=8 are shown in Figure 6.9.

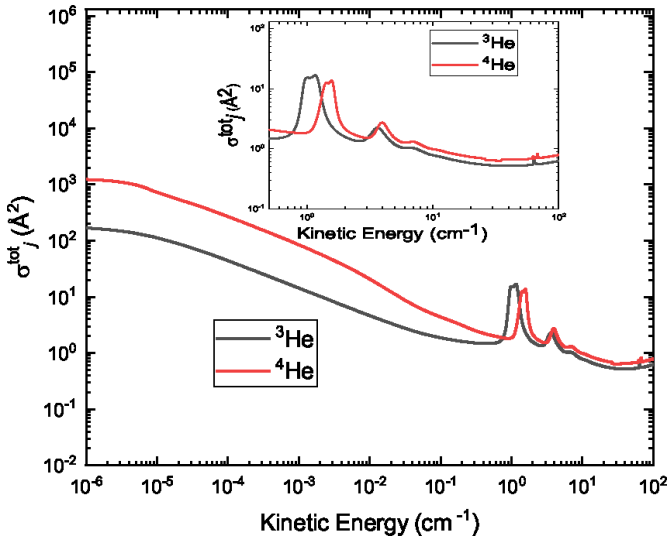

Figure 6.9: Total cross-sections for rotational transitions of C_2 collisions with ^{3}He (black curve) and ^{4}He (red curve) as function of kinetic energy for j=8.

6.3.3 Collisional Quenching Rate Coefficients

Using the equation 6.6, we have computed the rate coefficients of quenching as a function of temperature by averaging the cross-sections for the initial rotational level (j) to all final possible energy levels (j'). We have computed the rate coefficients in the temperature domain of 10^{-8} K to 100 K. Rate coefficients from j=2 to j'=0 for ^{3}He and ^{4}He are shown in Figure 6.10 and for initial level j=8 to final level j'=6,4,2 and 0 are plotted in Figure 6.11. We observe only even Δj transitions for our system and among them, j=8 to j'=6 have maximum value of quenching rate coefficients in the sub-Kelvin regime. The value of cross-sections (Figure 6.12) and rate coefficient increase with the increase in j value. Total rate coefficients are calculated by summing over all final states j' from a particular j^{th} level. The total rate coefficient for initial quantum number j=8 is plotted in Figure 6.13. Above 10^{-1} K, the rate value for heavier isotope matches the lighter one, but in the ultracold regime, the value of ^{4}He dominates the ^{3}He. This trend matches the case of N_2 colliding with ^{3}He and ^{4}He.[212] Zero temperature quenching rate coefficients are estimated to be 2.059×10^{-12}

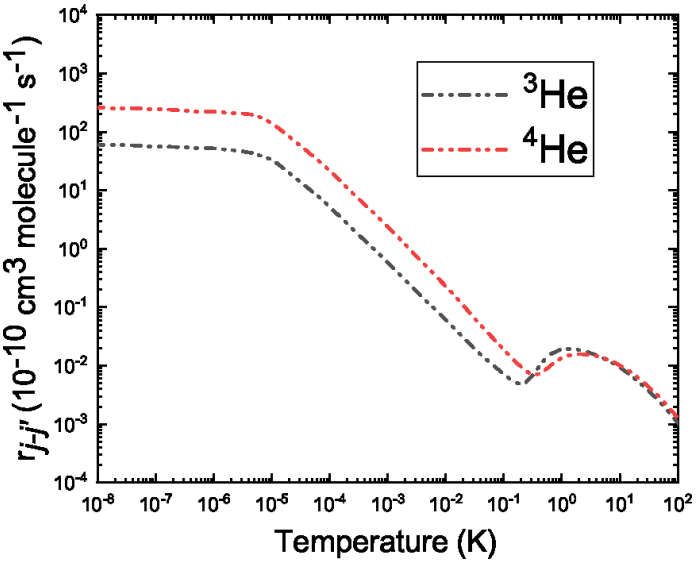

Figure 6.10: Rotational quenching rate coefficients of C_2 collisions with from j=2 to j'=0 with ^{3}He and ^{4}He.

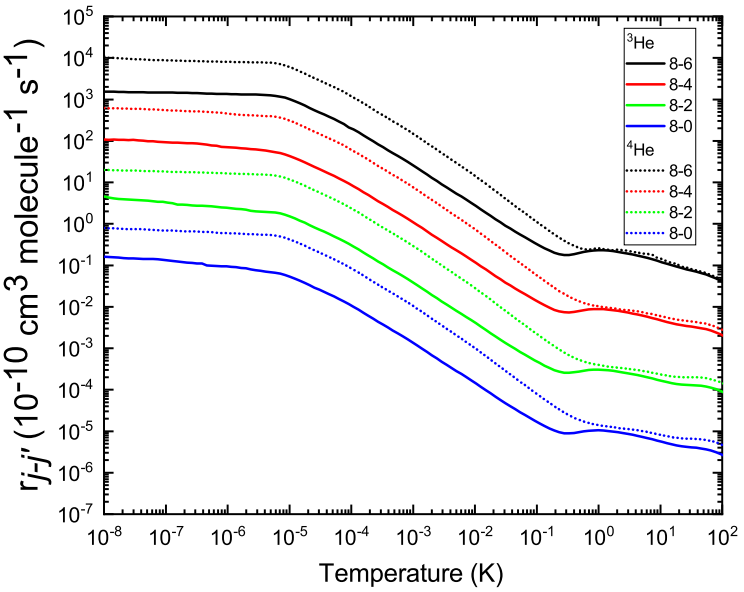

Figure 6.11: Rotational quenching rate coefficients of C_2 collisions with from j=8 to j'=6,4,2 and 0 with ^{3}He and ^{4}He.

cm^{-3}s^{-1} and 1.482×10^{-11} cm^{-3}s^{-1} computed using the equation 6.7 for ^{3}He and ^{4}He, respectively, and the lifetime of quasi bound state is calculated using equation 6.7 for ^{3}He-C_2 (2.75 ns) and is found to be larger than ^{4}He-C_2 (0.04 ns).

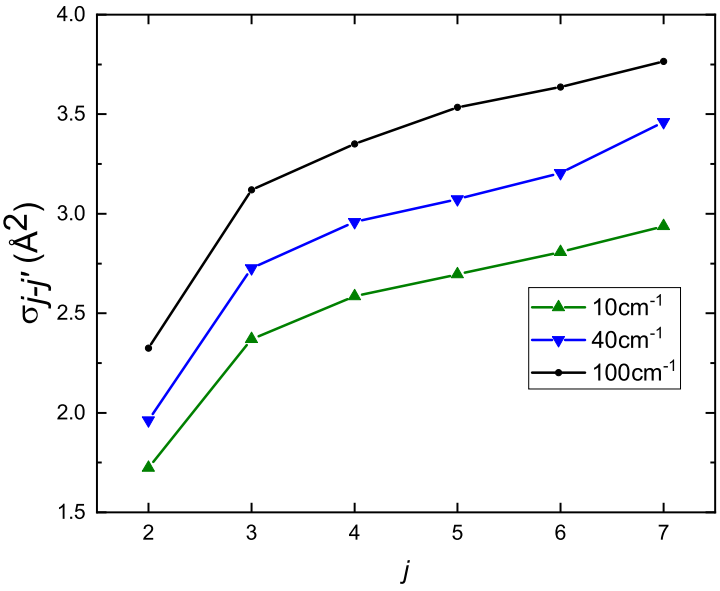

Figure 6.12: Plot of C_2 cross-sections with initial j and Δj=-2 for E_k=10, 40 and 100 cm^{-1} for ^{3}He.

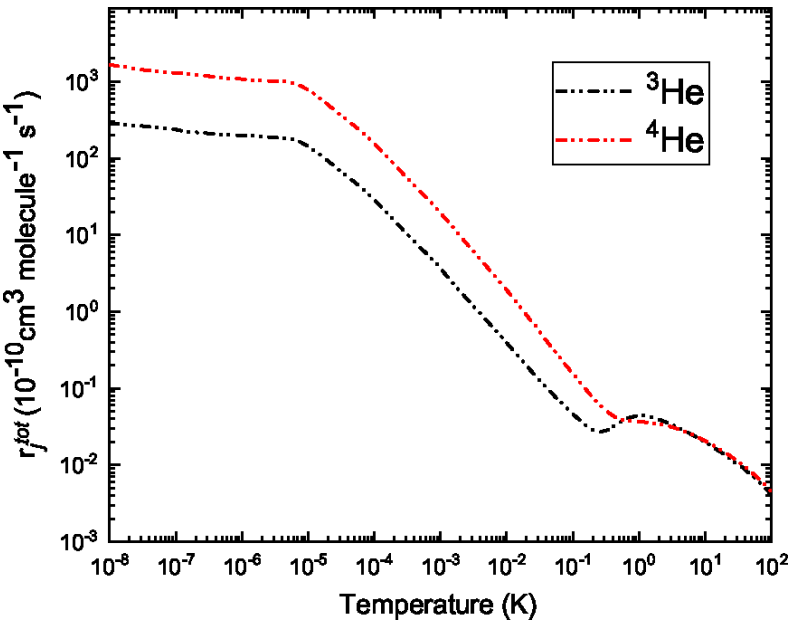

Figure 6.13: Total rotational rate coefficient for quenching of C_2 molecule with ^{3}He and ^{4}He for j=8.

6.4 Summary

1. In this chapter *ab initio* potential energy surface is computed for C_2 in collision with He using rigid rotor approximation. The calculations are carried out using the computed 2D-PES at CCSD(T)-F12b/aug-cc-pVQZ level of theory, keeping the C_2 fixed at r=1.246 Å. The PES has a well-depth of -20.30 cm^{-1} at R=4.0 Å and θ=0°.

2. Inelastic integral and total cross-sections and corresponding rotational rate coefficients are computed for C_2 quenching with ^{3}He and ^{4}He at ultracold (10^{-8} K) up to intermediate (100 K) temperatures. CC approach is used to determine the collisional state-to-state cross-sections.

3. Inelastic cross-sections show a decreasing trend with the increase in kinetic energy in the ultralow energy regime, validating Wigner's threshold law. Concerning the propensity trend, only even Δj transitions are favoured over odd ones. The cross-sections and quenching rate coefficients for heavier isotope ^{4}He-C_2 are larger than that for the lighter isotope ^{3}He-C_2 and thus ^{4}He-C_2 is a better rotational cooler for the C_2 molecule.

Chapter 7

Conclusions and Future Directions

7.1 Conclusions

The summary and conclusions of the thesis, along with future research prospects are outlined in this chapter. Our work has commenced with the computation of global potential energy surfaces, a crucial step for investigating quantum dynamics and spectroscopy. The first two chapters are introductory chapters. In the third chapter, potential energy surface is computed for CNNC-He and CNNC-H_2 using the CCSD(T)-F12a/aug-cc-pVTZ level of theory. The averaged CNNC-H_2 PES has a well-depth of -143.38 cm^{-1}, which is almost two times the minimum energy of -69.46 cm^{-1} for the CNNC-He collision. Both surfaces are T-shaped. Both systems show similar trends and shapes upon multipolar expansion. CNNC-H_2 collision has a larger isotropic term v_0 by $\sim$ 20 cm^{-1}in comparison to CNNC-He. Additionally, state-to-state cross-sections are calculated using close coupling method and the range of resonances in the CNNC-*para*-H_2 collision is broader, extending up to approximately 150 cm^{-1}, whereas the CNNC-He collision only covers a range up to 40 cm^{-1}. Only even Δj transitions are allowed due to the symmetric nature of CNNC. CNNC-*para*-H_2 rate coefficients are found to be 0.90-2.95 times those of CNNC-He rate coefficients.

The 4th chapter, PESs are computed for NCCP-He and NCCP-H_2 using the CCSD(T)-F12a/aug-cc-pVTZ level of theory. For averaged NCCP-H_2 PES, a global energy minimum of -125.40 cm^{-1} is observed which is approximately 2.5 times of NCCP-He (-46.40 cm^{-1}) collision. Upon expansion of PES, both systems demonstrate analogous trends and shapes. The isotropic term v_0 increases by about $\sim$ 20 cm^{-1} due to the lower minimum energy of the NCCP-H_2 collision. Furthermore, the range of resonances in the NCCP-*para*-H_2 collision observes up to 200 cm^{-1}, while it persists

up to 50 cm^{-1} in the case of NCCP-He. The molecular asymmetry of NCCP results in transitions that produce both even and odd Δj values. The rate coefficients for NCCP-*para*-H_2 are found to be 1.5 to 4.5 times greater than those for NCCP-He collision. Modeling the NCCP abundance in the ISM will be simpler owing to new insights into collision rates and other dynamic properties between H_2/He and NCCP.

5th chapter discusses the interaction of the ionic molecule COH^+ in collision with He starting with PES at CCSD(T)/aug-cc-pVQZ level of theory. COH^+-He has a global minimum of -853.49 cm^{-1} at α=0° and R = 2.9 Å. The inelastic cross-sections as a function of energy are calculated in the energy range of 0.5-250 cm^{-1} using the CC method. Both even and odd Δj transitions are allowed due to the asymmetric nature of COH^+. Δj=-1 transitions are favoured over other Δj transitions. The rotational frequencies of the bound states with j in the range 0-19 have been computed for this system. CC calculations are further performed for calculating the broadening cross-sections for kinetic energies up to 150 cm^{-1}. The comparison between the broadening and the inelastic cross-sections predicts that some extra peaks are available in the former that are absent in the case of inelastic cross-sections. The state-to-state rate coefficients have been calculated for the COH^+−He complex and the results are consistent with the previously reported data for COH^+-He, with minor variations primarily attributed to differences in the potential energy surface well depths for both systems.

In the last chapter, the interaction of C_2 with ^{3}He and ^{4}He is studied at ultracold temperatures. *ab initio* PES has a well-depth of -20.30 cm^{-1} at R=4.0 Å and θ=0°. Inelastic integral and total cross-sections are calculated in the energy domain of 10^{-6} cm^{-1}-1000 cm^{-1} for both ^{3}He-C_2 and ^{4}He-C_2. and corresponding rotational rate coefficients are computed for C_2 quenching with ^{3}He and ^{4}He at ultracold (10^{-8} K) up to intermediate (100 K) temperatures. CC approach is used to determine the collisional state-to-state cross-sections. We obtain state-to-state cross-sections for j=8 to j'=0, 2, 4 and 6 and j=2 to j'=0. The value of cross-sections decreases with the increase in kinetic energy below 10^{-1} cm^{-1} following Wigner's threshold law at ultralow kinetic energies. Quenching rate coefficients are calculated in the temperature domain of 10^{-8} K to 100 K. Above 10^{-1} K, the rate value for heavier isotope matches with the lighter one, but in the ultracold regime, the value of ^{4}He dominates the ^{3}He. Zero temperature quenching rate coefficients are estimated to be 2.059×10^{-12} $cm^{-3}s^{-1}$ and 1.482×10^{-11} $cm^{-3}s^{-1}$ computed for ^{3}He and ^{4}He, respectively, and the lifetime of quasi bound state is calculated for ^{3}He-C_2 (2.75 ns). It is found to be larger than

^{4}He-C_2 (0.04 ns). Further, the value of scattering length (SL) is calculated for both the isotopes of He colliding with C_2. The values of SL for ^{3}He and ^{4}He are 4.48 Å and 4.67 Å, respectively. ^{4}He-C_2 is a better rotational cooler for the C_2 molecule.

7.2 Future Directions

1. The interaction of COH^+ has been studied solely with He using time-independent quantum dynamics by our group and Santander et al. In cold ISM, H_2, H^+ and He are the most abundant colliders. The collisional dynamical study may be incorporated with *ortho*-H_2 and *para*-H_2 using a similar methodology.

2. Our study considers the few orientations of angular motion of H_2 molecule for quantum dynamics in studying the collision of CNNC and NCCP with *para*-H_2. All possible orientations can be considered in order to study and compare the effect of *ortho*-H_2 on CNNC and NCCP collision with *para*-H_2.

3. We have studied the rotational energy transfer in C_2 dimer undergoing collision with He using rigid rotor approximation. One can perform vibrational studies for this complex and calculate vibrational inelastic cross-sections with the relaxation of C-C intermolecular bond.

Appendix A

Fortran Code for Finding Pressure Broadening Cross-sections as a Function of Temperature for COH^+ System

```
IMPLICIT REAL*8(A-H, O-Z)
PARAMETER(N=218, M=1)
DIMENSION SIGMA(N), e(N), SUM(M), LOGSUM(M)
OPEN(UNIT=1, FILE='01.dat')
OPEN(UNIT=40, FILE='k01.dat')
BOLTZ=1.380658D-23
DO I=1,N
READ(1,*) E(I), SIGMA(I)
ENDDO
DO I=1,N
E(I)=E(I)*1.9865D-23
ENDDO
TP=88.D0
DO J=1,M
CONST=(1/BOLTZ/TP)**2
PRINT*,'TP, CONST'
PRINT*, TP, CONST
SM=0.D0
DO I=1,N
```

```
EXPONT=DEXP(-E(I)/BOLTZ/TP)
SM=SM+(SIGMA(I)*E(I)*EXPONT)
CONTINUE
SUM(J)=CONST*SM
SUM(J)=SUM(J)/6.023D23
WRITE(40,*)TP, SUM(J)
TP=TP+2.D0
CONTINUE
PRINT*,CONST
STOP
END
```

Appendix B

Fortran Code for Finding Pressure Broadening Coefficient for COH^+ System

```
IMPLICIT REAL*8(A-H, O-Z)
PARAMETER(N=218,M=1)
DIMENSION SIGMA(N), e(N), SUM(M), LOGSUM(M)
OPEN(UNIT=1, FILE='01.dat')
OPEN(UNIT=40, FILE='k01.dat')
AKBOLTZ=1.380658D-23
PI=DACOS(-1.D0)
xH=1.00797D0
xC=12.0107D0
xO=15.9999D0
xHe=4.002602D0
REDM=((xC+xO+xH)*xHe)/(xH+xC+xO+xHe)
PRINT*,REDM
AMU=REDM*1.6605402D-27
DO I=1,N
READ(1,*) E(I), SIGMA(I)
ENDDO
DO I=1,N
SIGMA(I)=SIGMA(I)*1.D-20
DO I=1,N
E(I)=E(I)*1.9865D-23
```

```
ENDDO
TP=88.D0
DO J=1,M
RELVEL=DSQRT(8.D0*AKBOLTZ*TP/PI/AMU)
CONST1=RELVEL*(1/AKBOLTZ/TP)**2
CONST2=(1/(2*PI*AKBOLTZ*TP))
CONST3=133.322*1.D-6
PRINT*,‘RELVEL, AKBOLTZ, TP, CONST1’
PRINT*,RELVEL, AKBOLTZ, TP, CONST1
SM=0.D0
DO I=1,N
EXPONT=DEXP(-E(I)/AKBOLTZ/TP)
SM=SM+(SIGMA(I)*E(I)*EXPONT)
CONTINUE
SUM(J)=CONST1*CONST2*CONST3*SM*1.D1
SUM(J)=SUM(J)/6.023D23
WRITE(40,*)TP, SUM(J)
TP=TP+2.d0
CONTINUE
PRINT*,CONST1, CONST2, EXPONT, AMU, AKBOLTZ
STOP
END
```

References

[1] G. Winnewisser, J. T. Armstrong, The Physics and Chemistry of Interstellar Molecular Clouds mm and Sub-mm Observations in Astrophysics, volume 331, 1989.

[2] G. Winnewisser, K. M. T. Yamada, Interstellar Molecules: Their Laboratory and Interstellar Habitat, Springer, Berlin, Germany, 2011.

[3] Cdms classic documentation, 2024. URL: https://cdms.astro.uni-koeln.de/classic/molecules.

[4] S. Weinreb, A. H. Barrett, M. L. Meeks, J. C. Henry, Radio Observations of OH in the Interstellar Medium, Nature 200 (1963) 829–831.

[5] G. R. Carruthers, Rocket Observation of Interstellar Molecular Hydrogen, Astrophys. J. 161 (1970) L81.

[6] E. E. Etim, E. Arunan, Accurate Enthalpies of Formation of Astromolecules: Energy, Stability and Abundance, (2016). arXiv:1609.09589.

[7] E. Roueff, F. Lique, Molecular Excitation in the Interstellar Medium: Recent Advances in Collisional, Radiative, and Chemical Processes, Chem. Rev. 113 (2013) 8906–8938.

[8] B. A. McGuire, 2018 Census of Interstellar, Circumstellar, Extragalactic, Protoplanetary Disk, and Exoplanetary Molecules, Astrophys. J. Suppl. Ser. 239 (2018) 17.

[9] S. A. Sandford, M. Nuevo, P. P. Bera, T. J. Lee, Prebiotic Astrochemistry and the Formation of Molecules of Astrobiological Interest in Interstellar Clouds and Protostellar Disks, Chem. Rev. 120 (2020) 4616–4659.

[10] D. Rehder, Chemistry in Space: From Interstellar Matter to the Origin of Life, Wiley-VCH, Weinheim, 2010.

[11] C. Puzzarini, V. Barone, A Never-Ending Story in the Sky: The Secrets of Chemical Evolution, Phys. Life Rev. 32 (2020) 59–94.

[12] P. Ehrenfreund, J. Cami, Cosmic Carbon Chemistry: From the Interstellar Medium to the Early Earth, volume 2, Cold Spring Harbor Laboratory Press, Cold Spring Harbor, NY, USA, 2010.

[13] R. C. Fortenberry, A Vision for the Future of Astrochemistry in the Interstellar Medium by 2050, ACS Phys. Chem. Au. 4 (2024) 31.

[14] R. C. Fortenberry, Quantum Astrochemical Spectroscopy, Int. J. Quantum Chem. 117 (2017) 81–91.

[15] V. Barone, M. Biczysko, C. Puzzarini, Quantum Chemistry Meets Spectroscopy for Astrochemistry: Increasing Complexity Toward Prebiotic Molecules, Acc. Chem. Res. 48 (2015) 1413–1422.

[16] L. Mckemmish, Accurate Molecular Spectroscopy Data for Astrochemistry: Strengths and Limitations., 43rd COSPAR Scientific Assembly 43 (2021) 1919.

[17] C. Puzzarini, V. Barone, The Challenging Playground of Astrochemistry: An Integral Strategy, Phys. Chem. Chem. Phys. 22 (2020) 6507–6523.

[18] C. Puzzarini, Astrophysics and Astrochemistry: The Role of Rotational Spectroscopy, IAU General Assembly 29 (2015) 2255621.

[19] R. B. Bernstein, Atom-Molecule Collision Theory: A Guide for the Experimentalist, Springer US, 2013.

[20] I. W. Smith, Laboratory Astrochemistry: Gas-phase Processes, Annual Review A&A 49 (2011) 29–66.

[21] M. Born, R. Oppenheimer, Zur Quantentheorie Der Molekeln, Ann. Phys. 389 (1927) 457–484.

[22] L. M. Ziurys, The Chemistry in Circumstellar Envelopes of Evolved Stars: Following the Origin of the Elements to the Origin of Life, Proc. Natl. Acad. Sci. U.S.A. 103 (2006) 12274–12279.

[23] A. Fuente, S. García-Burillo, M. Gerin, D. Teyssier, A. Usero, J. R. Rizzo, P. de Vicente, Photon-dominated Chemistry in the Nucleus of M82: Widespread HOC^+ Emission in the Inner 650 Parsec Disk, Astrophys. J. 619 (2005) L155–L158.

[24] M. Guelin, J. Cernicharo, G. Paubert, B. E. Turner, Free CP in IRC+10216, Astron. Astrophys. 230 (1990) L9–L11.

[25] C. Xue, E. R. Willis, R. A. Loomis, K. L. K. Lee, A. M. Burkhardt, C. N. Shingledecker, S. B. Charnley, M. A. Cordiner, S. Kalenskii, M. C. McCarthy, E. Herbst, A. J. Remijan, B. A. McGuire, Detection of Interstellar HC_4NC and an Investigation of Isocyanopolyyne Chemistry under TMC-1 Conditions, Astrophys. J. 900 (2020) L9.

[26] C. Cabezas, J. Cernicharo, J. L. Alonso, M. Agndez, S. Mata, M. Gulin, I. Pea, Laboratory and Astronomical Discovery of Hydromagnesium Isocyanide, Astrophys. J. 775 (2013) 133.

[27] B. E. Turner, B. Zuckerman, Observations of Strongly Deuterated Molecules: Implications for Interstellar Chemistry., Astrophys. J. 225 (1978) L75–L79.

[28] K. Kawaguchi, M. Ohishi, S.-I. Ishikawa, N. Kaifu, Detection of Isocyanoacetylene HCCNC in TMC-1, Astrophys. J. 386 (1992) L51.

[29] Cernicharo, J., Velilla-Prieto, L., Agúndez, M., Pardo, J. R., Fonfría, J. P., Quintana-Lacaci, G., Cabezas, C., Bermúdez, C., Guélin, M., Discovery of the First Ca-Bearing Molecule in Space: CaNC, Astron. Astrophys. 627 (2019) L4.

[30] A. J. Remijan, J. M. Hollis, F. J. Lovas, D. F. Plusquellic, P. R. Jewell, Interstellar Isomers: The Importance of Bonding Energy Differences, Astrophys. J. 632 (2005) 333–339.

[31] P. Schilke, C. Comito, S. Thorwirth, First Detection of Vibrationally Excited HNC in Space, Astrophys. J. 582 (2003) L101–L104.

[32] M. Guélin, S. Muller, J. Cernicharo, M. McCarthy, P. Thaddeus, Detection of the SiNC radical in IRC+10216, Astron. Astrophys. 426 (2004) L49–L52.

[33] R. Kołos, Z. R. Grabowski, The Chemistry and Prospects for Interstellar Detection of Some Dicyanoacetylenes and Other Cyanoacetylene-related Species, Astrophys. Space Sci. 271 (2000) 65–72.

[34] C. E. Dateo, M. Dupuis, W. A. Lester, Ab Initio Study of Cyanogen: The $X^1\Sigma_g^+$, $a^3\Sigma_u^+$, $B^1\Delta_u$, and $C^1\Pi_u$ States, J. Chem. Phys. 83 (1985) 265–272.

[35] R. E. Connors, J. L. Roebber, K. Weiss, Vacuum Ultraviolet Spectroscopy of Cyanogen and Cyanoacetylenes, J. Chem. Phys. 60 (1974) 5011–5024.

[36] S. Bell, Electronic Structure and Spectrum of Cyanogen, Chem. Phys. Lett. 67 (1979) 498–502.

[37] E. A. J. Wannenmacher, H. Lin, W. M. Jackson, Photodissociation Dynamics of Cyanogen (C_2N_2) in the Threshold Region for Dissociation, J. Phys. Chem. 94 (1990) 6608–6615.

[38] S. A. Barts, J. B. Halpern, The Emission Spectrum of C_2N_2, Chem. Phys. Lett. 161 (1989) 207–211.

[39] A. G. Maki, High-Resolution Infrared Spectra of Cyanogen and Cyanogen-$^{15}N_2$, J. Chem. Phys. 43 (1965) 3193–3199.

[40] L. H. Jones, Raman and Far Infrared Spectrum of C_2N_2, J. Mol. Spectrosc. 45 (1973) 55–64.

[41] M. Sana, G. Leroy, Etude Theorique Des Proprietes Thermodynamiques Du Radical CN Et De Ses Dimeres, J. Mol. Struct.: THEOCHEM 76 (1981) 259–276.

[42] R. K. Chaudhuri, S. Krishnamachari, K. F. Freed, Ab Initio Description of the Ground and Excited States of Cyanogen Isomers, J. Mol. Struct.: THEOCHEM 768 (2006) 119–126.

[43] Y. H. Ding, X. R. Huang, Z. S. Li, C. C. Sun, Theoretical Study on Potential Energy Surface of C_2N_2, J. Chem. Phys. 108 (1998) 2024–2027.

[44] P. Botschwina, P. Sebald, Calculated Spectroscopic Properties for NCCN, CNCN, CNNC and HNCCN, Chem. Phys. 141 (1990) 311–323.

[45] M. T. Nguyen, Isocyanogen (NCNC) and Diisocyanogen (CNNC): Structures and Some Spectroscopic Properties, Chem. Phys. Lett. 157 (1989) 430–435.

[46] S. Petrie, Proton Affinities of Dicyanogen Isomers: Is There a Preferred Site of Protonation for CNCN?, J. Phys. Chem. A 102 (1998) 7835–7840.

[47] K. Sunil, J. Yates, K. Jordan, Theoretical Study of the Isomerization of Cyanogen, Chem. Phys. Lett. 171 (1990) 185–190.

[48] T. van der Does, F. Bickelhaupt, Diisocyanogen, Angew. Chem. Int. Ed. 27 (1988) 936–938.

[49] G. Maier, H. P. Reisenauer, J. Eckwert, C. Sierakowski, T. Stumpf, Matrix Isolation of Diisocyanogen CNNC, Angew. Chem. Int. Ed. 31 (1992) 1218–1220.

[50] O. Grabandt, C. De Lange, R. Mooyman, T. van der Does, F. Bickelhaupt, He(I) Photoelectron Spectroscopy of Diisocyanogen (CNNC), Chem. Phys. Lett. 155 (1989) 221–226.

[51] M. B. Bell, P. A. Feldman, M. J. Travers, M. C. McCarthy, C. A. Gottlieb, P. Thaddeus, Detection of $HC_{11}N$ in the Cold Dust Cloud TMC-1, Astrophys. J. 483 (1997) L61–L64.

[52] M. Krüger, H. Dreizler, D. Preugschat, D. Lentz, Synthesis and Structure of Ethynyl Isocyanide, Angew. Chem. Int. Ed. 30 (1991) 1644–1646.

[53] S. Petrie, T. J. Millar, A. J. Markwick, NCCN in TMC-1 and IRC+10216, Mon. Not. R. Astron. Soc. 341 (2003) 609–616.

[54] M. Agúndez, N. Marcelino, J. Cernicharo, Discovery of Interstellar Isocyanogen (CNCN): Further Evidence that Dicyanopolyynes Are Abundant in Space, Astrophys. J. 861 (2018) L22.

[55] S. Petrie, Y. Osamura, NCCN and NCCCCN Formation in Titan's Atmosphere:HNC as a Viable Precursor, J. Phys. Chem. A 108 (2004) 3623–3631.

[56] Y. Osamura, S. Petrie, NCCN and NCCCCN Formation in Titan's Atmosphere: 1. Competing Reactions of Precursor HCCN(^{3}A") with H(^{2}S) and CH_3(^{2}A′), J. Phys. Chem. A 108 (2004) 3615–3622.

[57] M. Agúndez, J. Cernicharo, P. de Vicente, N. Marcelino, E. Roueff, A. Fuente, M. Gerin, M. Guélin, C. Albo, A. Barcia, L. Barbas, R. Bolaño, F. Colomer, M. C. Diez, J. D. Gallego, J. Gómez-González, I. López-Fernández, J. A. López-Fernández, J. A. López-Pérez, I. Malo, J. M. Serna, F. Tercero, Probing Non-polar Interstellar Molecules Through their Protonated Form: Detection of Protonated Cyanogen ($NCCNH^+$), Astron. Astrophys. 579 (2015) L10.

[58] J. Cernicharo, M. Guélin, Discovery of the C_8H Radical, Astron. Astrophys. 309 (1996) L27–L30.

[59] M. Guelin, N. Neininger, J. Cernicharo, Astronomical Detection of the Cyanobutadiynyl Radical C_5N, 335 (1998) L1–L4.

[60] J. Cernicharo, M. Guélin, H. Hein, C. Kahane, Sulfur in IRC+10216, Astron. Astrophys. 181 (1987) L9–L12.

[61] M. Ohishi, N. Kaifu, K. Kawaguchi, A. Murakami, S. Saito, S. Yamamoto, S.-I. Ishikawa, Y. Fujita, Y. Shiratori, W. M. Irvine, Detection of a New Circumstellar Carbon Chain Molecule C_4Si, Astrophys. J. Lett. 345 (1989) L83.

[62] M. Bell, L. Avery, P. Feldman, C_3S and C_5S in IRC+10216, Astrophys. J. 417 (1993) L37.

[63] D. Halfen, D. Clouthier, L. M. Ziurys, Detection of the CCP Radical ($X^2\Pi$) in IRC+10216: A New Interstellar Phosphorus-containing Species, Astrophys. J. 677 (2008) L101.

[64] G. Wallerstein, I. Iben, P. Parker, A. M. Boesgaard, G. M. Hale, A. E. Champagne, C. A. Barnes, F. Käppeler, V. V. Smith, R. D. Hoffman, et al., Synthesis of the Elements in Stars: Forty Years of Progress, Rev. Mod. Phys. 69 (1997) 995.

[65] E. M. Burbidge, Phosphorus Over-abundance in Quasars Re-Examined, Astrophys. Space Sci. 265 (1999) 99–101.

[66] P. Dufton, F. Keenan, A. Hibbert, The Abundance of Phosphorus in the Interstellar Medium, Astron. Astrophys. 164 (1986) 179–183.

[67] B. Turner, J. Bally, Detection of Interstellar PN: The First Identified Phosphorus Compound in the Interstellar Medium, Astrophys. J. 321 (1987) L75–L79.

[68] L. M. Ziurys, Detection of interstellar PN: The First Phosphorus-bearing Species Observed in Molecular Clouds, Astrophys. J. 321 (1987) L81–L85.

[69] T. Tsuji, Molecular Abundances in Stellar Atmospheres II., Astron. Astrophys. 23 (1973) 411–431.

[70] B. E. Turner, T. Tsuji, J. Bally, M. Guelin, J. Cernicharo, Phosphorus in the Dense Interstellar Medium, Astrophys. J. 365 (1990) 569.

[71] O. Kwon, M. L. McKee, Theoretical Calculations on the NCCP Potential Energy Surface, J. Phys. Chem. A 105 (2001) 478–483.

[72] N.-N. Pham-Tran, B. Hajgató, T. Veszprémi, M. T. Nguyen, Theoretical Study of Cyanophosphapropyne (NCCP), Isocyanophosphapropyne (CNCP) and their

Isomers: Stability and Properties, Phys. Chem. Chem. Phys. 3 (2001) 1588–1597.

[73] T. A. Cooper, H. W. Kroto, J. F. Nixon, O. Ohashi, Detection of C-cyanophosphaethyne, NCCP by Microwave Spectroscopy, J. Chem. Soc., Chem. Commun. (1980) 333–334.

[74] L. Bizzocchi, S. Thorwirth, H. S. Müller, F. Lewen, G. Winnewisser, Submillimeter-Wave Spectroscopy of Phosphaalkynes: HCCCP, NCCP, HCP, and DCP, J. Mol. Spectrosc. 205 (2001) 110–116.

[75] Agúndez, Marcelino, Cernicharo, José, Guélin, Michel, New Molecules in IRC+10216: Confirmation of C_5S and Tentative Identification of MgCCH, NCCP, and SiH_3CN, Astron. Astrophys. 570 (2014) A45.

[76] M. Agúndez, J. Cernicharo, M. Guélin, Discovery of Phosphaethyne (HCP) in Space: Phosphorus Chemistry in Circumstellar Envelopes, Astrophys. J. 662 (2007) L91–L94.

[77] S. Milam, D. Halfen, E. Tenenbaum, A. Apponi, N. Woolf, L. Ziurys, Constraining Phosphorus Chemistry in Carbon-and Oxygen-rich Circumstellar Envelopes: Observations of PN, HCP, and CP, Astrophys. J. 684 (2008) 618.

[78] T. Yamaguchi, S. Takano, N. Sakai, T. Sakai, S.-Y. Liu, Y.-N. Su, N. Hirano, S. Takakuwa, Y. Aikawa, H. Nomura, S. Yamamoto, Detection of Phosphorus Nitride in the Lynds 1157 B1 Shocked Region, Publ. Astron. Soc. Jpn 63 (2011) L37–L41.

[79] D. Haasler, V. M. Rivilla, S. Martí n, J. Holdship, S. Viti, N. Harada, J. Mangum, K. Sakamoto, S. Muller, K. Tanaka, Y. Yoshimura, K. Nakanishi, L. Colzi, L. Hunt, K. L. Emig, R. Aladro, P. Humire, C. Henkel, P. van der Werf, First Extragalactic Detection of a Phosphorus-bearing Molecule: Phosphorus Nitride (PN), Astron. Astrophys. 659 (2022) A158.

[80] Tobola, R., Klos, J., Lique, F., Chalasinski, G., Alexander, M. H., Rotational Excitation and De-excitation of PN Molecules by He Atoms, Astron. Astrophys. 468 (2007) 1123–1127.

[81] C. T. Bop, N. A. Boye Faye, K. Hammami, N. Jaidane, Rotational Excitation of the CP($X^2\Sigma^+$) Open Shell Molecule due to Collision with He(^1S), J. Phys. Chem. A 121 (2017) 7854–7860.

[82] A. Badri, F. Najar, C. T. Bop, N.-E. Jaidane, M. Hochlaf, State-to-state Inelastic Rate Coefficients of Phosphine in Collision with He at Low to Moderate Temperature, Mon. Not. R. Astron. Soc. 499 (2020) 1578–1586.

[83] F. Najar, M. Naouai, H. E. Hanini, N. Jaidane, Rotationally Inelastic Scattering of PN by Para-H_2(j=0) at Low/Moderate Temperature, Mon. Not. R. Astron. Soc. 472 (2017) 2919–2925.

[84] E. Herbst, Molecular Ions in Interstellar Reaction Networks, J. Phys.: Conf. Ser. 4 (2005) 17.

[85] M. Guélin, J. Cernicharo, Organic Molecules in Interstellar Space: Latest Advances, Front. Astron. Space Sci. 9 (2022) 787567.

[86] R. Spezia, Y. Jeanvoine, D. Scuderi, Ion-Molecule Reactions as a Possible Synthetic Route for the Formation of Prebiotic Molecules in Space, Springer (2018) 277–292.

[87] D. K. Bohme, Charge State Chemistry: What a Difference a Charge Makes in Gas-phase Chemistry, Int. J. Mass Spectrom. 472 (2022) 116674.

[88] S. Petrie, D. K. Bohme, Ions in space, Mass Spectrom. Rev. 26 (2007) 258–280.

[89] F. Walter, F. Bertoldi, C. Carilli, P. Cox, K. Y. Lo, R. Neri, X. Fan, A. Omont, M. A. Strauss, K. M. Menten, Molecular Gas in the Host Galaxy of a Quasar at Redshift Z=6.42, Nature 424 (2003) 406–408.

[90] D. Buhl, L. E. Snyder, Unidentified Interstellar Microwave Line, Nature 228 (1970) 267–269.

[91] W. Kraemer, G. Diercksen, Identification of Interstellar X-ogen as HCO^+, Astrophys. J. 205 (1976) L97–L100.

[92] P. J. Bruna, S. D. Peyerimhoff, R. J. Buenker, Ab Initio Investigation of the HCO^+ and COH^+ Molecule-ions: Structure and Potential Surfaces for Dissociation in Ground and Excited States, Chem. Phys. 10 (1975) 323–334.

[93] T. Monteiro, Rotational Excitation of Molecular Ions in Interstellar Clouds: HCO^+ and HCS^+, Mon. Not. R. Astron. Soc. 210 (1984) 1–11.

[94] T. S. Monteiro, Rotational Excitation of HCO^+ by Collisions with H_2, Mon. Not. R. Astron. Soc. 214 (1985) 419–427.

[95] B. Giovanni, D. Luca, M. Markus, State-to-state Rotational Transition Rates of the HCO^+ Ion by Collisions with Helium, Mon. Not. R. Astron. Soc. 397 (2009) 1909–1914.

[96] T. J. Dhilip Kumar, S. Kumar, Low-energy Rotational Inelastic Collisions of H^+ + CO System, J. Chem. Phys. 136 (2012) 044317.

[97] H. Masso, L. Wiesenfeld, The HCO^+-H_2 van der Waals Interaction: Potential Energy and Scattering, J. Chem. Phys. 141 (2014) 184301.

[98] M. Mladenovic, Theoretical Spectroscopic Parameters for Isotopic Variants of HCO^+ and HOC^+, J. Chem. Phys. 147 (2017) 114111.

[99] O. Denis-Alpizar, T. Stoecklin, A. Dutrey, S. Guilloteau, Rotational Relaxation of HCO^+ and DCO^+ by Collision with H_2, Mon. Not. R. Astron. Soc. 497 (2020) 4276–4281.

[100] F. Tonolo, L. Bizzocchi, M. Melosso, F. Lique, L. Dore, V. Barone, C. Puzzarini, An Improved Study of HCO^+ and He System: Interaction Potential, Collisional Relaxation, and Pressure Broadening, J. Chem. Phys. 155 (2021) 234306.

[101] R. Woods, C. Gudeman, R. Dickman, P. Goldsmith, G. Huguenin, W. Irvine, A. Hjalmarson, L.-A. Nyman, H. Olofsson, The HCO^+/HOC^+ Abundance Ratio in Molecular Clouds, Astrophys. J. 270 (1983) 583–588.

[102] M. F. Jarrold, M. T. Bowers, D. J. Defrees, A. D. McLean, E. Herbst, A Reanalysis of the HCO^+/HOC^+ Abundance Ratio in Dense Interstellar Clouds, Astrophys. J. 303 1 (1986) 392–400.

[103] D. J. Defrees, A. D. McLean, E. Herbst, Calculations Concerning the HCO^+/HOC^+ Abundance Ratio in Dense Interstellar Clouds, Astrophys. J. 279 (1984) 322–334.

[104] N. L. Ma, B. J. Smith, L. Radom, Refined Calculations of the Structures and Stabilities of the Formyl (HCO^+) and Isoformyl (COH^+) Cations, Chem. Phys. Lett. 197 (1992) 573–580.

[105] S. Raugei, M. L. Klein, Ab Initio Molecular Dynamics Investigation of the Formyl Cation in the Superacid SbF_5/HF, J. Phys. Chem. B 105 (2001) 8212–8219.

[106] W. Wagner-Redeker, P. R. Kemper, M. F. Jarrold, M. T. Bowers, The Formation and Reactivity of HOC^+: Interstellar Implications, J. Chem. Phys. 83 (1985) 1121–1131.

[107] M. Smith, S. v. Schlemmer, J. von Richthofen, D. Gerlich, $HOC^+ + H_2$ Isomerization Rate at 25 K: Implications for the Observed $[HCO^+]/[HOC^+]$ Ratios in the Interstellar Medium, Astrophys. J. 578 (2002) L87.

[108] L. M. Ziurys, A. J. Apponi, Confirmation of Interstellar HOC^+: Reevaluating the $[HCO^+]/[COH^+]$ Abundance Ratio, Astrophys. J. Lett. 455 (1995) L73.

[109] H. Liszt, R. Lucas, J. H. Black, The Abundance of HOC^+ in Diffuse Clouds, Astron. Astrophys. 428 (2004) 117–120.

[110] A. J. Apponi, T. C. Pesch, L. M. Ziurys, Detection of HOC^+ toward the Orion Bar and M17-SW: Enhanced Abundances in Photon-dominated Regions?, Astrophys. J. 519 (1999) L89–L92.

[111] M. Gerin, H. Liszt, D. Neufeld, B. Godard, P. Sonnentrucker, J. Pety, E. Roueff, Molecular Ion Abundances in the Diffuse ISM: CF^+, HCO^+, HOC^+, and C_3H^+, Astron. Astrophys. 622 (2019) A26.

[112] D. Flower, Molecular Collisions in the Interstellar Medium, Cambridge University Press, Cambridge, England, UK, 2007.

[113] G. Quéméner, CHAPTER 12: Ultracold Collisions of Molecules, 2018.

[114] H.-J. Werner, P. J. Knowles, F. R. Knizia, F. R. Manby, M. Schutz, . et al., See http://www.molpro.net (MOLPRO, a package of *ab initio* programs, Version 2015).

[115] M. J. Frisch, G. W. Trucks, H. B. Schlegel, G. E. Scuseria, M. A. Robb, J. R. Cheeseman, G. Scalmani, V. Barone, G. A. Petersson, H. Nakatsuji, X. Li, M. Caricato, A. V. Marenich, J. Bloino, B. G. Janesko, R. Gomperts, B. Mennucci, H. P. Hratchian, J. V. Ortiz, A. F. Izmaylov, J. L. Sonnenberg, D. Williams-Young, F. Ding, F. Lipparini, F. Egidi, J. Goings, B. Peng, A. Petrone, T. Henderson, D. Ranasinghe, V. G. Zakrzewski, J. Gao, N. Rega, G. Zheng, W. Liang, M. Hada, M. Ehara, K. Toyota, R. Fukuda, J. Hasegawa, M. Ishida, T. Nakajima, Y. Honda, O. Kitao, H. Nakai, T. Vreven, K. Throssell, J. A. Montgomery, Jr., J. E. Peralta, F. Ogliaro, M. J. Bearpark, J. J. Heyd, E. N. Brothers, K. N. Kudin, V. N. Staroverov, T. A. Keith, R. Kobayashi,

J. Normand, K. Raghavachari, A. P. Rendell, J. C. Burant, S. S. Iyengar, J. Tomasi, M. Cossi, J. M. Millam, M. Klene, C. Adamo, R. Cammi, J. W. Ochterski, R. L. Martin, K. Morokuma, O. Farkas, J. B. Foresman, D. J. Fox, Gaussian16 Revision B.01, 2016. Gaussian Inc. Wallingford CT.

[116] K. Raghavachari, G. W. Trucks, J. A. Pople, M. Head-Gordon, A Fifth-order Perturbation Comparison of Electron Correlation Theories, Chem. Phys. Lett. 157 (1989) 479–483.

[117] T. B. Adler, G. Knizia, H.-J. Werner, A Simple and Efficient CCSD(T)-F12 Approximation, J. Chem. Phys. 127 (2007) 221106.

[118] G. Knizia, T. B. Adler, H.-J. Werner, Simplified CCSD(T)-F12 Methods: Theory and Benchmarks, J. Chem. Phys. 130 (2009) 054104.

[119] R. A. Kendall, T. H. Dunning, R. J. Harrison, Electron Affinities of the First-row Atoms Revisited. Systematic Basis Sets and Wave Functions, J. Chem. Phys. 96 (1992) 6796–6806.

[120] T. H. Dunning, Gaussian Basis Sets for Use in Correlated Molecular Calculations. I. The Atoms Boron through Neon and Hydrogen, J. Chem. Phys. 90 (1989) 1007–1023.

[121] S. F. Boys, F. Bernardi, The Calculation of Small Molecular Interactions by the Differences of Separate Total Energies. Some Procedures with Reduced Errors, Mol. Phys. 19 (1970) 553–566.

[122] A. M. Arthurs, A. Dalgarno, D. R. Bates, The Theory of Scattering by a Rigid Rotator, Proc. R. Soc. A. 256 (1960) 540–551.

[123] C. F. Curtiss, F. Adler, The scattering of Atoms From Fiatomic Molecules, J. Chem. Phys. 20 (1952) 249–256.

[124] P. Botschwina, J. Flügge, Ab Initio Vibration-Rotation Coupling Constants and the Equilibrium Geometries of NCCN and CNCN, Chem. Phys. Lett. 180 (1991) 589–593.

[125] Ritika, S. Kumar, T. J. Dhilip Kumar, Electronic Structure Calculations and Quantum Dynamics of Rotational De-excitation of CNNC by He, Phys. Chem. Chem. Phys. 24 (2022) 2785–2793.

[126] S. Kumar, A. Kushwaha, T. J. Dhilip Kumar, Quantum Dynamics Study of Rotational Transitions of NCCN Induced by He Collision, J. Chem. Phys. 149 (2018) 174312.

[127] D. Ben Abdallah, M. M. Al Mogren, S. Dhaif Allah Al Harbi, M. Hochlaf, Rotational (De-)excitation of Isocyanogen by Collision with Helium at Low Energies, J. Chem. Phys. 149 (2018) 064305.

[128] A. Chefai, F. Khadri, K. Hammami, F. Lique, Collisional Excitation of Interstellar CCN($X^2\Pi$) Induced by He, J. Chem. Phys. 149 (2018) 014305.

[129] S. Kumar, A. Kushwaha, R. Kaur, T. J. Dhilip Kumar, Ultracold Rotational Quenching of NCCN Scattering with ^{3}He and ^{4}He, Chem. Phys. Lett. 738 (2020) 136819.

[130] D. B. Abdallah, K. Hammami, F. Najar, N. Jaidane, Z. B. Lakhdar, M. L. Senent, G. Chambaud, M. Hochlaf, Low-Temperature Rate Constants for Rotational Excitation and De-excitation of C_3 ($X^1\Sigma_g^+$) by Collisions with He (^{1}S), Astrophys. J. 686 (2008) 379–383.

[131] S. Kumar, T. J. Dhilip Kumar, Quantum Scattering Calculations for Rotational Excitations of C_3 by Hydrogen Atom: Potential Energy Surfaces and Rate Coefficients, J. Phys. Chem. A 123 (2019) 7296–7302.

[132] S. Kumar, T. J. Dhilip Kumar, Ab Initio Potential Energy Surfaces of C_3 Collision with Proton and Quantum Dynamics of Rotational Transition, J. Phys. Chem. A 122 (2018) 5437–5444.

[133] G. A. Parker, R. L. Snow, R. T. Pack, Intermolecular Potential Surfaces from Electron Gas Methods. I. Angle and Distance Dependence of the He-CO_2 and Ar-CO_2 Interactions, J. Chem. Phys. 64 (1976) 1668–1678.

[134] J. Hutson, S. Green, Molscat computer code, version 14, MOLSCAT Computer Code, Version 14, Collaborative Computational Project No. 6 of the Science and Engineering Research Council, UK (1994).

[135] M. H. Alexander, D. E. Manolopoulos, A Stable Linear Reference Potential Algorithm for Solution of the Quantum Close-coupled Equations in Molecular Scattering Theory, J. Chem. Phys. 86 (1987) 2044–2050.

[136] K. M. Christoffel, J. M. Bowman, Complex Coordinate Calculations of Feshbach Resonance Energies and Widths for a Collinear Triatomic System, J. Chem. Phys. 78 (1983) 3952–3958.

[137] L. N. Smith, D. J. Malik, D. Secrest, Rotational Compound State Resonances for an Argon and Methane Scattering System, J. Chem. Phys. 71 (1979) 4502–4514.

[138] F. Najar, D. Ben Abdallah, N. Jaidane, Z. Ben Lakhdar, Potential energy surface for the $C_2(X^1\Sigma_g^+)$+He(^{1}S) System: Application to the Rotationally Inelastic Scattering of C_2 in Collisions with He, Chem. Phys. Lett. 460 (2008) 31–36.

[139] A. Faure, P. Jankowski, T. Stoecklin, K. Szalewicz, On the Importance of Full-Dimensionality in Low-Energy Molecular Scattering Calculations, Sci. Rep. 6 (2016) 1–10.

[140] Ritika, T. J. Dhilip Kumar, New Potential Energy Surface and Rotational De-excitation Cross-sections of CNNC by para-H_2 (j_p=0), Phys. Chem. Chem. Phys. 25 (2023) 24904–24911.

[141] Ritika, S. Kumar, T. J. Dhilip Kumar, Electronic Structure Calculations and Quantum Dynamics of Rotational De-excitation of CNNC by He, Phys. Chem. Chem. Phys. 24 (2022) 2785–2793.

[142] A. Kushwaha, Ritika, P. Chahal, T. J. Dhilip Kumar, Rotational Excitation of NCCN by p-H_2(j_c = 0) at Low Temperatures, ACS Earth Space Chem. 7 (2023) 515–522.

[143] F. Najar, D. Ben Abdallah, N. Jaidane, Z. Ben Lakhdar, G. Chambaud, M. Hochlaf, Rotational Excitation and De-excitation of $C_2(X^1\Sigma_g^+)$ by Para-H_2(j=0), J. Chem. Phys. 130 (2009) 204305.

[144] J. M. Robbe, H. Lavendy, D. Lemoine, B. Pouilly, Theoretical Study of the Deexcitation of C_2 in Collisions with Helium, Astron. Astrophys. 256 (1992) 679–682.

[145] Ritika, T. J. Dhilip Kumar, New Ab Initio Calculations and Collisional Properties of Closed-shell NCCP ($^1\Sigma^+$) by Collisions with He (^{1}S), Mon. Not. R. Astron. Soc. 515 (2022) 5145–5150.

[146] H. El Hanini, M. Naouai, A. Jrad, F. Najar, N.-E. Jaidane, Rotational (De-)excitation of Oxophosphine (HPO) by Collision with Helium (He), Comput. Theor. Chem. 1203 (2021) 113355.

[147] C. Nkem, K. Hammami, Y. Halawlaw, O. O. Calvin, N.-E. Jaidane, Rotational Excitation of Protonated Hydrogen Cyanide ($HCNH^+$) by He Atom at Low Temperature, Astrophys. Space Sci. 349 (2013) 171–179.

[148] D. P. Tew, W. Klopper, A Comparison of Linear and Nonlinear Correlation Factors for Basis Set Limit Moller-Plesset Second Order Binding Energies and Structures of He_2, Be_2, and Ne_2, J. Chem. Phys. 125 (2006) 094302.

[149] J.-M. Launay, Molecular Collision Processes. I. Body-Fixed Theory of Collisions Between Two Systems with Arbitrary Angular Momenta, J. Phys. B: Atom. Mol. Phys. 10 (1977) 3665.

[150] D. Flower, J.-M. Launay, E. Kochanski, J. Prissette, An Ab Initio Potential Energy Surface for the Study of CO-H_2 Collision at Thermal Energies, Chem. Phys. 37 (1979) 355–362.

[151] Ritika, T. J. Dhilip Kumar, NCCP Collisions with Para-H_2: Accurate Potential Energy Surface and Quantum Dynamics at Interstellar Temperatures, Mon. Not. R. Astron. Soc. 527 (2024) 9826–9832.

[152] F. Lique, M.-L. Senent, A. Spielfiedel, N. Feautrier, Rotationally Inelastic Collisions of $SO(X^3\Sigma^-)$ with H_2: Potential Energy Surface and Rate Coefficients for Excitation by Para-H_2 at Low Temperature, J. Chem. Phys. 126 (2007) 164312.

[153] P. Halvick, T. Stoecklin, F. Lique, M. Hochlaf, Explicitly Correlated Treatment of the Ar-NO^+ Cation, J. Chem. Phys. 135 (2011) 044312.

[154] O. Denis-Alpizar, T. Stoecklin, P. Halvick, Rovibrational Energy Transfer in the He-C_3 Collision: Potential Energy Surface and Bound States, J. Chem. Phys. 140 (2014) 084316.

[155] D. Papp, J. Sarka, T. Szidarovszky, A. G. Csaszar, E. M*á*tyus, M. Hochlaf, T. Stoecklin, Complex Rovibrational Dynamics of the Ar-NO^+ Complex, Phys. Chem. Chem. Phys. 19 (2017) 8152–8160.

[156] M. M. Al Mogren, O. Denis-Alpizar, D. B. Abdallah, T. Stoecklin, P. Halvick, M.-L. Senent, M. Hochlaf, On the Use of Explicitly Correlated Treatment

Methods for the Generation of Accurate Polyatomic-He/H_2 Interaction Potential Energy Surfaces: The Case of C_3-He Complex and Generalization, J. Chem. Phys. 141 (2014) 044308.

[157] R. D. Johnson, Computational Chemistry Comparison and Benchmark Database, NIST Standard Reference Database 101, 2002.

[158] Y. Zhu, L. Tian, H. Song, M. Yang, Kinetic and Dynamic Studies of the H_3^+ + CO $\rightarrow H_2$ + HCO^+/HOC^+ Reaction on a High-level Ab Initio Potential Energy Surface, J. Chem. Phys. 151 (2019) 054311.

[159] M. Mladenovic, M. Lewerenz, Comparison of Spectroscopic Strategies to Determine Molecular Geometries and the Impact of Nuclear Versus Atomic Masses: The Example of HCO^+ and HOC^+, Mol. Phys. 116 (2018) 3607–3620.

[160] G. D. Purvis, R. J. Bartlett, A Full Coupled-cluster Singles and Doubles Model: The Inclusion of Disconnected Triples, J. Chem. Phys. 76 (1982) 1910–1918.

[161] Ritika, T. J. Dhilip Kumar, Rotational Transitions of COH^+ and He: New Interaction Potential, Bound States, Scattering and Pressure Broadening Cross-sections, ChemPhysChem 25 (2024) e202300607.

[162] C. L. Santander, R. Urzúa-Leiva, T. Stoecklin, O. Denis-Alpizar, Rotational Transitions of HOC^+ Induced by Collision with He at Low Temperature, J. Phys. Chem. A 123 (2019) 10990.

[163] J. M. Hutson, C. R. L. Sueur, Bound and Field: Programs for Calculating Bound States of Interacting Pairs of Atoms and Molecules, Comp. Phys. Commun. 241 (2019) 1–8.

[164] J. M. Hutson, C. R. L. Sueur, User Manual for MOLSCAT, BOUND and FIELD, Version 2022: Programs for Quantum Scattering Properties and Bound States of Interacting Pairs of Atoms and Molecules, 2019. URL: https://arxiv.org/abs/1903.06755.

[165] J. Koput, *Ab Initio* Structure and Vibration-Rotation Dynamics of the Formyl and Isoformyl Cations, HCO^+/HOC^+, J. Chem. Phys. 150 (2019) 154307.

[166] Ritika, T. J. Dhilip Kumar, Rotational Quenching of C_2 with ^{3}He and ^{4}He Collisions at Ultracold Temperatures, Chem. Phys. Lett. 798 (2022) 139623.

[167] A. Palma, S. Green, Effect of the Potential Well on Low Temperature Pressure Broadening in CO–He, J. Chem. Phys. 85 (1986) 1333–1335.

[168] B. Yang, H. Perera, N. Balakrishnan, R. C. Forrey, P. C. Stancil, Quenching of Rotationally Excited CO in Cold and Ultracold Collisions with H, He and H_2, J. Phys. B: At. Mol. Opt. Phys. 39 (2006) S1229.

[169] C. D. Ball, F. C. De Lucia, Direct Measurement of Rotationally Inelastic Cross Sections at Astrophysical and Quantum Collisional Temperatures, Phys. Rev. Lett. 81 (1998) 305–308.

[170] Q. Liao, E. Herbst, Calculations of the low temperature pressure broadening of HCO^+ rotational spectral lines by H_2, J. Chem. Phys. 104 (1996) 3956–3961.

[171] C. D. Ball, M. Mengel, F. C. De Lucia, D. E. Woon, Quantum Scattering Calculations for H_2S-He between 1-600 K in Comparison with Pressure Broadening, Shift, and Time Resolved Double Resonance Experiments, J. Chem. Phys. 111 (1999) 8893–8903.

[172] B. Giovanni, D. Luca, T. Francesca, M. Markus, Experimental and Theoretical Study of Helium Broadening and Shift of HCO^+ Rotational Lines, Chem. Phys. Chem. 9 (2008) 2237–2244.

[173] Q. Liao, E. Herbst, Calculations of the Low Temperature Pressure Broadening of HCO^+ Rotational Spectral Lines by H_2, J. Chem. Phys. 104 (1996) 3956–3961.

[174] A. Godard Palluet, F. Thibault, F. Lique, Rotational Excitation of CO_2 Induced by He: New Potential Energy Surface and Scattering Calculations, J. Chem. Phys. 156 (2022) 104303.

[175] M. T. Bell, T. P. Softley, Ultracold Molecules and Ultracold Chemistry, Mol. Phys. 107 (2009) 99–132.

[176] J. M. Hutson, Ultracold Chemistry, Sci. 327 (2010) 788–789.

[177] L. D. Carr, D. DeMille, R. V. Krems, J. Ye, Cold and Ultracold Molecules: Science, Technology and Applications, New J. Phys. 11 (2009) 055049.

[178] R. V. Krems, Cold Controlled Chemistry, Phys. Chem. Chem. Phys. 10 (2008) 4079–4092.

[179] H. L. Bethlem, G. Meijer, Production and Application of Translationally Cold Molecules, Int. Rev. Phys. Chem. 22 (2003) 73–128.

[180] N. Balakrishnan, Perspective: Ultracold Molecules and the Dawn of Cold Controlled Chemistry, J. Chem. Phys. 145 (2016) 150901.

[181] R. V. Krems, Molecules Near Absolute Zero and External Field Control of Atomic and Molecular Dynamics, Int. Rev. Phys. Chem. 24 (2005) 99–118.

[182] N. Nemitz, F. Baumer, F. Münchow, S. Tassy, A. Görlitz, Production of Heteronuclear Molecules in an Electronically Excited State by Photoassociation in a Mixture of Ultracold Yb and Rb, Phys. Rev. A 79 (2009) 061403.

[183] S. Y. Van De Meerakker, N. Vanhaecke, G. Meijer, Stark Deceleration and Trapping of OH Radicals, Annu. Rev. Phys. Chem. 57 (2006) 159–190.

[184] J. M. Doyle, B. Friedrich, J. Kim, D. Patterson, Buffer-gas Loading of Atoms and Molecules into a Magnetic Trap, Phys. Rev. A 52 (1995) R2515–R2518.

[185] N. Tariq, N. A. Taisan, V. Singh, J. D. Weinstein, Spectroscopic Detection of the LiHe Molecule, Phys. Rev. Lett. 110 (2013) 153201.

[186] N. R. Hutzler, H.-I. Lu, J. M. Doyle, The Buffer Gas Beam: An Intense, Cold, and Slow Source for Atoms and Molecules, Chem. Rev. 112 (2012) 4803–4827.

[187] P. Barletta, J. Tennyson, P. Barker, Creating Ultracold Molecules by Collisions with Ultracold Rare-gas Atoms in an Optical Trap, Phys. Rev. A 78 (2008) 052707.

[188] M. Schnell, G. Meijer, Cold Molecules: Preparation, Applications, and Challenges, Angew. Chem. Int. Ed. 48 (2009) 6010–6031.

[189] S. Y. T. Van De Meerakker, H. L. Bethlem, N. Vanhaecke, G. Meijer, Manipulation and Control of Molecular Beams, Chem. Rev. 112 (2012) 4828–4878.

[190] J. Bahns, P. Gould, W. Stwalley, Formation of Cold (T$\leq$1K) Molecules, volume 42 of *Advances in Atomic, Molecular, and Optical Physics*, Academic Press, (2000), pp. 171–224.

[191] K. M. Jones, E. Tiesinga, P. D. Lett, P. S. Julienne, Ultracold Photoassociation Spectroscopy: Long-range Molecules and Atomic Scattering, Rev. Mod. Phys. 78 (2006) 483–535.

[192] E. A. Donley, N. R. Claussen, S. T. Thompson, C. E. Wieman, Atom-Molecule Coherence in a Bose-Einstein Condensate, Nature 417 (2002) 529533.

[193] T. Köhler, K. Góral, P. S. Julienne, Production of Cold Molecules Via Magnetically Tunable Feshbach Resonances, Rev. Mod. Phys. 78 (2006) 1311–1361.

[194] C. Chin, R. Grimm, P. Julienne, E. Tiesinga, Feshbach Resonances in Ultracold Gases, Rev. Mod. Phys. 82 (2010) 1225–1286.

[195] H. Bethlem, G. Berden, F. Crompvoets, R. Jongma, A. van Roij, G. Meijer, Electrostatic Trapping of Ammonia Molecules, Nature 406 (2000) 491–494.

[196] H. L. Bethlem, G. Berden, A. J. A. Van Roij, F. M. H. Crompvoets, G. Meijer, Trapping Neutral Molecules in a Traveling Potential Well, Phys. Rev. Lett. 84 (2000) 5744–5747.

[197] M. Pawlak, P. Zuchowski, P. Jankowski, Kinetic Isotope Effect in Low-Energy Collisions between Hydrogen Isotopologues and Metastable Helium Atoms: Theoretical Calculations including the Vibrational Excitation of the Molecule, J. Chem. Theory Comput. 17 (2021) 1008–1016.

[198] R. Kaur, T. J. Dhilip Kumar, Rotational Quenching of CS in Ultracold ^{3}He Collisions, Chem. Phys. Lett. 659 (2016) 304–309.

[199] A. Bergeat, S. Chefdeville, M. Costes, S. B. Morales, C. Naulin, U. Even, J. Klos, F. Lique, Understanding the Quantum Nature of Low-energy C(^{3}P$_j$) + He Inelastic Collisions, Nat. Chem. 10 (2018) 519522.

[200] A. Banks, D. Clary, H.-J. Werner, Vibrational Relaxation of N_2 by Collision with He Atoms, J. Chem. Phys. 84 (1986) 3788–3797.

[201] T. Stoecklin, A. Voronin, J. Rayez, Vibrational Quenching of N_2 (ν=1, j_{rot}=j) by ^{3}He: Surface and Close-coupling Calculations at Very Low Energy, Phys. Rev. A 66 (2002) 042703.

[202] E. Dimova, G. Petrov, K. Blagoev, Quenching of ^{4}He and ^{3}He Excited States by Collisions with N_2, Vacuum 76 (2004) 405–408.

[203] N. Balakrishnan, A. Dalgarno, On the Quenching of Rovibrationally Excited Molecular Oxygen at Ultracold Temperatures, J. Phys. Chem. A 105 (2001) 2348–2351.

[204] F. Paesani, F. Gianturco, Vibrational Effects in a Weakly-Interacting Quantum Solvent: The CO Molecule in ^{4}He Gas and in ^{4}He Droplets, J. Chem. Phys. 116 (2002) 10170–10182.

[205] E. Bodo, F. Gianturco, A. Dalgarno, Quenching of Vibrationally Excited CO (ν=2) Molecules by Ultracold Collisions with ^{4}He Atoms, Chem. Phys. Lett. 353 (2002) 127–130.

[206] P. Florian, M. Hoster, R. Forrey, Rotational Relaxation in Ultracold CO+He Collisions, Phys. Rev. A 70 (2004) 032709.

[207] R. V. Krems, Molecules Near Absolute Zero and External Field Control of Atomic and Molecular Dynamics, Int. Rev. Phys. Chem. 24 (2005) 99–118.

[208] K. Miyamoto, S. Narita, Y. Masumoto, T. Hashishin, T. Osawa, M. Kimura, M. Ochiai, M. Uchiyama, Room-Temperature Chemical Synthesis of C_2, Nat. Commun. 11 (2020) 1–7.

[209] H. S. Rzepa, A Thermodynamic Assessment of the Reported Room-Temperature Chemical Synthesis of C_2, Nat. Commun. 12 (2021) 1–3.

[210] R. Decarvalho, J. M. Doyle, B. Friedrich, T. Guillet, J. Kim, D. Patterson, J. D. Weinstein, Buffer-gas Loaded Magnetic Traps for Atoms and Molecules: A Primer, Eur. Phys. J. At. Mol. Opt. Plasma Phys. 7 (1999) 289–309.

[211] N. Balakrishnan, R. Forrey, A. Dalgarno, Threshold Phenomena in Ultracold Atommolecule Collisions, Chem. Phys. Lett. 280 (1997) 1–4.

[212] T. Stoecklin, A. Voronin, Strong Isotope Effect in Ultracold Collision of N_2^+ ($\nu = 1$, $j = 0$) with He: A Case Study of Virtual-State Scattering, Phys. Rev. A 72 (2005) 042714.

[213] Xu, X.T., Shao, X., Yu, C.H., Sun, C.Y., Huang, W., Feng, E., Cold and Ultracold Collisions of MgH with Helium, Eur. Phys. J. D 65 (2011) 383–390.

Publications

1. **Ritika**, S. Kumar and T. J. Dhilip Kumar, "Electronic Structure Calculations and Quantum Dynamics of Rotational De-excitation of CNNC by He", *Phys. Chem. Chem. Phys.*, **2022**, 24, 2785-2793. https://doi.org/10.1039/D1CP04273D

2. **Ritika** and T. J. Dhilip Kumar, "Rotational Quenching C_2 with ^{3}He and ^{4}He Collisions at Ultracold Temperatures" *Chem. Phys. Lett.*, **2022**, 798, 174312. https://doi.org/10.1016/j.cplett.2022.139623

3. **Ritika** and T. J. Dhilip Kumar, "New *Ab Initio* Calculations and Collisional Properties of Closed-Shell NCCP ($^1\Sigma^+$) by Collision with He (^{1}S)", *Mon. Not. R. Astron. Soc.*, **2022**, 515, 51455150. https://doi.org/10.1093/mnras/stac2063

4. A. Kushwaha, **Ritika**, P. Chahal and T. J. Dhilip Kumar, "Rotational Excitation of NCCN by *p*-H_2 (j_c=0) at Low Temperatures", *ACS Earth Space Chem.*, **2023**, 7, 515522. https://doi.org/10.1021/acsearthspacechem.2c00355

5. **Ritika**, and T. J. Dhilip Kumar, "New Potential Energy Surface and Rotational De-excitation Cross-sections of CNNC by Collisions with *Para*-H_2 (j_p=0)", *Phys. Chem. Chem. Phys.*, **2023**, 25, 24904-24911. https://doi.org/10.1039/d3cp03354f

6. **Ritika**, and T. J. Dhilip Kumar, "Rotational transitions of COH^+ with He: New Interaction Potential, Bound States, Scattering and Pressure Broadening Cross-sections", *ChemPhysChem*, **2024**, e202300607. https://doi.org/10.1002/cphc.202300607

7. **Ritika** and T. J. Dhilip Kumar, "NCCP Collisions with *Para*-H_2: Accurate Potential Energy Surface and Quantum Dynamics at Interstellar Temperatures", *Mon. Not. R. Astron. Soc.*, **2024**, 527, 9826-9832. https://doi.org/10.1093/mnras/stad3840

8. **Ritika**, and T. J. Dhilip Kumar, "Improved Potential Energy Surface and Quantum Dynamics of Phosphorus Mononitride (NP) by Helium" (*Manuscript in Preparation*).

9. **Ritika**, and T. J. Dhilip Kumar, "Nonadiabatic Couplings in H^+ + NP Collision using Time-Dependent Quantum Dynamics" (*Manuscript in Preparation*).

10. Gurjaspreet Singh, Pooja Malik, Yamini Thakur, Sumesh Khurana, **Ritika**, Priyanka and T. J. Dhilip Kumar, K.N. Singh "Development of a Triazole-Linked Bis-Organosilane Compound as a Dual-Function Agent: Sensing of Al^{3+} Ions in Aqueous Environments and Inhibition of HIV-1 Protease" (*Under Review*).

Conferences & Workshops

1. Attended a GIAN course: **Ultracold Molecules and Controlled Chemistry** held at Indian Institute of Technology Ropar, Rupnagar, India. (December 16−20, 2019)

2. Attended a workshop on **Practical Aspects of Quantum Chemical Calculations** conducted by the Department of Chemistry, Kurukshetra University. (December 25, 2019-January 10, 2020)

3. Attended a national computing course on HPC Shiksha: **Basics of High-Performance Computing** organized by IITs Goa, Kharagpur, Madras, and Palakkad. (November 2020- February 2021)

4. Delivered an oral presentation "Electronic structure calculations and quantum dynamical study of neutral molecule-atom collisions" in **Virtual Winter School of Computational Chemistry**. (February 21−25, 2022)

5. Presented a poster on "New *ab initio* calculations and collisional properties of closed-shell NCCP ($^1\Sigma^+$) by collision with He (^{1}S)" in **DAE BRNS Symposium on Current Trends in Theoretical Chemistry (CTTC-2022)** at BARC, Mumbai, India. (September 22−24, 2022)

6. Presented a poster "Electronic structure calculations and quantum dynamical study of neutral molecule- atom collisions" in **Theoretical Chemistry and Biology (TCB) Symposium**, NIPER Mohali, India. (October 15, 2022)

7. Presented a poster "New *ab initio* calculations and collisional properties of closed-shell NCCP ($^1\Sigma^+$) by collision with He (^{1}S)" in **PMRF Annual Symposium 2022**, IIT Madras, India. (February 17−18, 2022)

8. Delivered an oral presentation "Electronic structure calculations and quantum dynamical study of neutral molecule-atom collisions" at **Chem Fest-2023**, IIT Ropar, India. (March 9, 2023)

9. Presented a poster "Rotational quenching C_2 with ^{3}He and ^{4}He collisions at ultracold temperatures" at **Workshop on Ultracold Molecules (UW-2023)** at University of Warsaw, Warsaw, Poland. (September 05−08, 2023)

10. Presented a poster "Rotational de-excitation rates of CNNC ($^1\Sigma^+$) by collisions with *para*-H_2 (j_p=0) in new 4D surface" at **International Conference on**

Molecular Energy Transfer in Complex Systems (iCOMET) in Shiv Vilas Resort, Jaipur, India. (November 12−17, 2023)

11. Presented a poster "NCCP collisions with *para*-H_2: Accurate potential energy surface and quantum dynamics at interstellar temperatures" at **Conference: The Path of Quantum Chemistry into the 21st Century (PQCC-2023)** at ETH Zurich, Switzerland. (January 16−18, 2024)

12. Delivered an oral presentation "From lab to space: Unravelling interstellar chemistry through collisional de-excitation at cold temperatures" at IIT Ropar on **National Science Day**.(February 28, 2024)

BIODATA

PERSONAL INFORMATION

Name : Ritika
Date of Birth : 2nd November, 1996
Nationality : Indian
Contact No. : 7988589118, 7834936286
Email Address : Ritikaarora1266@gmail.com
Ritika.19cyz0007@iitrpr.ac.in

ACADEMIC DETAILS

1. **Matriculation** (2011-2012): CBSE Board, SDMPS, Hansi with CGPA 8.60.
2. **Higher Secondary** (2013-2014): CBSE Board, SKDVM, Hansi with 87.8%
3. **B.Sc. Hons. Chemistry** (2014-2017): Department of Chemistry, Dyal Singh College, Delhi University, Delhi with 75.6%
4. **M.Sc Chemistry** (2017-2019): Department of Chemistry, Kurukshetra University, Kurukshetra with CGPA 8.88.
5. **Ph.D.** (2019-2024): Department of Chemistry, Indian Institute of Technology, Ropar with CGPA 8.8.

SKILLS AND PROFICIENCIES

1. **Software's Known**: Microsoft Office, Chem-Draw, Gaussian, Gauss View, MOLPRO, Origin Pro.
2. **Language Known**: Fortran
3. **Instrument's Operated**: Polarimeter, FT-IR Spectrometer, UV-Spectrophotometer, pH meter, Conductometer.

ACADEMIC ACHIEVEMENTS

1. Graduate Aptitude in Engineering (**GATE**) conducted by Indian Institute of Technology, Madras, 2019.
2. Junior Research Fellowship (**CSIR-JRF)** in Chemical Sciences with 88th rank.
3. Prestigious Prime Minister Research Fellowship (**PMRF),** July 2020-July 2024.

EXTRACURRICULAR ACTIVITIES

1. Member of the **Chemical Society** (Kurukshetra University).

LIST OF PUBLICATIONS

1. **Ritika;** Kumar, S.; Dhilip Kumar, T. J., Electronic structure calculations and quantum dynamics of rotational de-excitation of CNNC by He, *Phys. Chem. Chem. Phys.*, **2022**, 24 (5), 2785–2793. **(PCCP HOT ARTICLE)**
2. **Ritika** and Dhilip Kumar, T. J. Rotational quenching of C_2 with ^{3}He and ^{4}He collisions at ultracold temperatures, *Chem. Phys. Lett.*, **2022**, 798, 139623.
3. **Ritika** and Dhilip Kumar, T. J., New *ab initio* calculations and collisional properties of closed shell NCCP ($^1\Sigma^+$) by collisions with He (^{1}S), *Mon. Not. R. Astron. Soc.*, **2022**, 515, 5145-5150.
4. Kushwaha, A.; **Ritika;** Chahal, P.; Dhilip Kumar, T. J., Rotational excitation of NCCN by p-H_2 ($j_c = 0$) at low temperatures, *ACS Earth Space Chem.*, **2023**, 7, 515-522.
5. **Ritika** and Dhilip Kumar, T. J., New potential energy surface and rotational de-excitation cross-sections of CNNC by collisions with *para*-H_2 (j_p=0), *Phys. Chem. Chem. Phys.*, **2023**, 25, 24904-24911.
6. **Ritika**, and Dhilip Kumar, T. J., Rotational transitions of COH^+ with He: New interaction potential, bound states, scattering and pressure broadening cross-sections, *Chem. Phys. Chem.*, **2024**, 25, e202300607.
7. **Ritika** and Dhilip Kumar, T. J., NCCP collisions with *para*-H_2: Accurate potential energy surface and quantum dynamics at interstellar temperatures, *Mon. Not. R. Astron. Soc.*, **2024**, 527, 9826-9832